Alma Mater Studiorum · Università di Bologna

Scuola di Scienze
Dipartimento di Fisica e Astronomia
Corso di Laurea Magistrale in Fisica

Production and characterization of tin oxide thin films deposited via solution combustion synthesis

Relatore:
Prof. Beatrice Fraboni

Correlatore:
Dott. Rita Branquinho

Presentata da:
Matteo Giangolini

Abstract

The main goal of this thesis work is the production and characterization of Tin oxide thin film deposited via Solution Combustion Synthesis (SCS). Different precursors are used in order to study the effect of the chemical nature of the reagent on the structural, morphological and electrical properties of the thin films.

Tin oxide was chosen because is one of the most promising candidates for p-type oxide. In fact, the semiconductor oxides reported in the literature are mostly limited to n-type and there is a need for solution processed p-type oxide semiconductors to achieve Complementary Metal Oxide Semiconductors (CMOS) using all oxide materials. Anyway, the production window of solution processed for p-type SnO is narrow and Silver doping will be used to enhance the probability to get it. If production of p-type Tin oxide will not be achieved, the work will be focused on n-type SnO_2 and on the optimisation of devices made with this material, either Thin Film Transistors (TFTs) or Transparent Conductive Oxides (TCOs).

Samples made in this work show good optical properties, like transmittance over 80% and energy gap values around 3.79 eV, but none of them turned out to be a p-type oxide or a good TFT. Samples annealed at higher temperatures have good electrical conductivity properties, which could lead to a future study in order to optimise these materials for TCO purposes.

Contents

1 High mobility oxides: deposition methods and applications 19
1.1 Transparent Conductive Oxide 20
1.2 Thin Film Transistor 25
1.3 Solution combustion synthesis 32

2 Tin oxide 37
2.1 SnO 39
2.2 SnO_2 43

3 Materials and method 47
3.1 Precursors solution 47
3.2 Film deposition and characterization 49
3.3 Device fabrication and characterization 53

4 Experimental results 57
4.1 Solutions characterization 57
4.2 Thin film characterization 59
4.2.1 Samples with stoichiometric precursors 59
4.2.2 Different number of layers 72
4.2.3 Using Silver as dopant 77

5 Conclusions 105
5.1 Annealing at 150 $°C$ under DUV 105
5.2 Annealing at 180 $°C$ 107
5.3 Annealing at 250 $°C$ 107
5.4 Annealing at 300 $°C$ 108
5.5 Future prospective 108

Bibliography **111**

List of Figures

1.1 X-ray diffractograms calculated on the basis of a reference pattern for $Sn_6O : 4(OH)_4$ (ICDD-PDF: $01 - 084 - 2157$), SnO (01-072-1012), SnO_2 ($00 - 041 - 1445$), and Sn ($00 - 004 - 0673$), respectively, with $Cu - K_{\alpha 1}$ and $Cu - K_{\alpha 2}$ diffractions superimposed. In the figure below x-ray diffractograms of thin films annealed at different temperatures. The plot of a bare glass substrate is also given at the bottom as a reference[10]. 21

1.2 Dependence of (a) the electrical resistivity (ρ), (b) the mobility (μ), and (c) the carrier concentration (n) of the Aluminum Tin-Oxide (ATO) films (with thickness of $53\ nm$) on the annealing temperature and time[11]. 22

1.3 Structure of a TFT in a configuration staggered bottom-gate with the region of the channel depicted. 26

1.4 Comparison between TFT structures. 27

1.5 Typical a) output and b) transfer characteristics of a n-type oxide TFT[23]. 30

1.6 Comparison of the energy required for a conventional reaction relatively to a combustion one. 34

2.1 $Sn - O$ phase diagram[34]. 38

2.2 Comparison of the structure of the (a) SnO (001) and (b) SnO_2 (101) surfaces. 39

2.3 Ball-and-stick model of the litharge structure of SnO. 40

2.4 Comparison between the band structure of a) SnO_2 and b) SnO[23]. 41

2.5 Ball-and-stick models of SnO_2, low index surfaces. The bulk rutile-unit cell is shown in (a). (b), (c), and (d) show bulk termination of the (110), (100), and (101) surfaces respectively. On the left-hand side stoichiometric bulk terminations are represented. On the right-hand side surfaces with reduced oxygen concentration are indicated. 44

2.6 Decrease of the resistivity for TCO materials from 1970 to 2000[54]. 46

3.1 Samples deposited on glass, $p-Si$ and $p-Si/SiO_2$ respectively. In the first row there are the samples with NH_4NO_3 while in the second row there are the samples with $AgNO_3$. 50

3.2 Scheme of spin coating deposition. An excess amount of a liquid precursor is dropped. The substrate is held by vacuum and an high speed rotation spread the liquid over the entire substrate. A final anneal remove the solvents that are left in the film. 51

3.3 Image of the ellipsometer used for thickness evaluation. 52

3.4 Sample after source and drain electrodes deposition and after a post-annealing at 160 $°C$ for 1 h. 53

3.5 Van der Pauw pattern and contact positions used in this work. . . 54

4.1 DSC-TG analysis for the solution with $SnCl_2$, $AgNO_3$, $Urea$ and $2-ME$ as solvent. 58

4.2 The graphs show the FTIR spectra of the samples (a) with $AgNO_3$, (b) with NH_4NO_3 and (c) with no combustion process at 350 $°C$. There are no peaks over 1500 cm^{-1} for the samples annealed that prove that there are no organic bounds. In the fingerprint region the peaks are located at the same wavenumbers for samples with the same precursors. 60

4.3 The graph shows the FTIR spectra of the samples annealed at 150 $°C$ and the deep UV radiation. There are no peaks over 1500 cm^{-1} that prove that there are no organic bounds. In the fingerprint region the peaks are located at the same wavenumbers in both of the samples. Data are presented only until 2000 cm^{-1} because there are no peaks between 2000 cm^{-1} and 5000 cm^{-1}. 61

4.4 The graphs show the transmittance of the samples (a) annealed at $150\ ^{\circ}C$ under DUV, (b) with $AgNO_3$, (c) with NH_4NO_3 and (d) with no combustion process at $350\ ^{\circ}C$. Is visible that all the samples have a transmittance of at least over 80% in the visible range, except for the sample annealed at $150\ ^{\circ}C$ under DUV with no combustion and the sample with NH_4NO_3 annealed at $250\ ^{\circ}C$. 62

4.5 Thickness of the films depending on the annealing temperature. Thickness values are referred to samples deposited on $p-Si$ substrate. 64

4.6 XRD diffractograms of samples annealed at (a) $150\ ^{\circ}C$ under DUV, (b) $180\ ^{\circ}C$, (c) $250\ ^{\circ}C$, (d) $300\ ^{\circ}C$ and (e) $350\ ^{\circ}C$ with no combustion process. Is visible how the structure of the thin films changes due to the annealing temperature. At $150\ ^{\circ}C$, $180\ ^{\circ}C$ and $250\ ^{\circ}C$ there is no crystalline structure while at $300\ ^{\circ}C$ and $350\ ^{\circ}C$ the samples have the characteristic peaks of the SnO_2. . 65

4.7 Topographic height map of sample with $AgNO_3$ annealed at $150\ ^{\circ}C$ under DUV acquired by AFM in alternate mode. 66

4.8 Topographic maps of sample with $AgNO_3$ annealed at $180\ ^{\circ}C$ acquired by AFM in alternate mode. 66

4.9 (a)(b) 5x5 μm and (c)(d) 2x2 μm topographic maps of sample with $AgNO_3$ annealed at $300\ ^{\circ}C$ acquired by AFM in alternate mode. 67

4.10 SEM surface of the sample with $AgNO_3$ at two different magnification, (a) 20k and (b) 50k. Some agglomerations and the crystalline structure are visible. 68

4.11 Surface map of sample with $AgNO_3$ annealed at $300\ ^{\circ}C$ acquired by EDS. Here are reported the (a) electron map and the presence of (b) Tin, (c) Silver and (d) Oxygen. Is clearly visible that the agglomerations are mainly composed by Silver. 69

4.12 Transfer characteristic curves for the samples annealed at (a) $150\ °C$ under DUV, (b) $180\ °C$, (c) $250\ °C$, (d) $300\ °C$, (e) $350\ °C$. In the left y-axis the drain current (I_D) values are reported while in the right y-axis the gate leakage current (I_G) values are reported with dashed lines. All the measures were made with $V_D = 8\ V$ and V_{GS} that sweep from $-8\ V$ to $+8\ V$. The width/length ratio (W/L) is 14 for all the devices. 71

4.13 XRD diffractograms of the samples with (a) $AgNO_3$, (b) NH_4NO_3 with different number of layers. Is visible how the structure of the thin films changes due to the number of layers. In both of the cases only the films with 3 and 4 layers show a crystal structure. . 73

4.14 Thickness of the films depending on the number of layers. There is a linear-like relation between the number of layers of a film and its thickness. 75

4.15 Transfer characteristic curves for samples with different number of layers with (a) $AgNO_3$ and (b) NH_4NO_3 as precursor. In the left y-axis the drain current (I_D) values are reported while in the right y-axis the gate leakage current (I_G) values are reported with dashed lines. All the measures were made with $V_D = 8\ V$ and V_G that sweep from $-8\ V$ to $+8\ V$. The width/length ratio (W/L) is 14 for all the devices. 76

4.16 The graphs show the FTIR spectra of the samples annealed at (a) $150\ °C$ under DUV, (b) $180\ °C$ and (c) $300\ °C$. There are no peaks over $1500\ cm^{-1}$ for the samples that prove that there are no organic bounds. In the fingerprint region the peaks are not located at the same wavenumbers. 78

4.17 The graph shows the transmittance of samples doped with Ag, annealed at different temperatures. Most of the samples have a drop of transmittance around $2.5\ eV$, which makes them not fully transparent in the visible range. 79

4.18 Cross section of films annealed at $300\ °C$. The images report the thickness of the contacts deposited, of the film and of the $p - SiO_2$ substrate. 80

4.19 XRD diffractograms of samples deposited with stoichiometric reactions and doped with Ag annealed at (a) $150\ °C$ under DUV, (b) at $180\ °C$ and (c) at $300\ °C$. Is visible how the structure of the thin films changes due to the annealing temperature. At $150\ °C$ and $180\ °C$ there is no crystalline structure except for a peak due to Ag in samples heavily doped while at $300\ °C$ the samples have the characteristic peaks of Ag and $AgCl$. 82

4.20 Height (a, c, d) and amplitude (b) map of samples doped with Ag annealed at $180\ °C$ acquired by AFM in alternate mode. . . . 83

4.21 Height (a, c, e, f) and amplitude (b, d) map of samples doped with Ag annealed at $300\ °C$ acquired by AFM in alternate mode. 84

4.22 SEM surface of the sample doped with $0.1\ mmol$ of Ag annealed at $150\ °C$ under DUV at two different magnifications, (a) 20k and (b) 50k. Agglomerations are visible. 85

4.23 SEM surface of the sample doped with $0.2\ mmol$ of Ag annealed at $150\ °C$ under DUV at two different magnifications, (a) 20k and (b) 50k. Agglomerations are visible. 86

4.24 SEM surface of the sample doped with $0.4\ mmol$ of Ag annealed at $150\ °C$ under DUV at two different magnifications, (a) 20k and (b) 50k. Agglomerations are visible. 87

4.25 SEM surface of the sample doped with $0.1\ mmol$ of Ag annealed at $180\ °C$ at two different magnifications, (a) 20k and (b) 50k. Agglomerations are visible. 88

4.26 SEM surface of the samples doped with (a) 0.2 and (b) $0.4\ mmol$ of Ag annealed at $180\ °C$ at 20k of magnification. The surfaces are smooth. 89

4.27 SEM surface of the sample doped with $0.1\ mmol$ of Ag annealed at $300\ °C$ at two different magnifications, (a) 20k and (b) 50k. Some big clusters are visible. 90

4.28 SEM surface of the sample doped with $0.2\ mmol$ of Ag annealed at $300\ °C$ at two different magnifications, (a) 20k and (b) 50k. Some big clusters and agglomerations are visible. 91

4.29 SEM surface of the sample doped with $0.4\ mmol$ of Ag annealed at $300\ °C$ at two different magnifications, (a) 20k and (b) 50k. Several agglomerations are visible. 92

4.30 Surface map acquired by EDS of sample doped with $0.1\ mmol$ of Ag and annealed at $150\ °C$ under DUV. Here are reported the (a) electron map and the presence of (b) Tin, (c) Silver and (d) Chlorine. Table (e) shows weight and percentage of atoms in the sample's surface. 94
4.31 Surface map acquired by EDS of sample doped with $0.2\ mmol$ of Ag and annealed at $150\ °C$ under DUV. Here are reported the (a) electron map and the presence of (b) Tin, (c) Silver and (d) Chlorine. Table (e) shows weight and percentage of atoms in the sample's surface. 95
4.32 Surface map acquired by EDS of sample doped with $0.4\ mmol$ of Ag and annealed at $150\ °C$ under DUV. Here are reported the (a) electron map and the presence of (b) Tin, (c) Silver and (d) Chlorine. Table (e) shows weight and percentage of atoms in the sample's surface. 96
4.33 Surface map acquired by EDS of sample doped with $0.1\ mmol$ of Ag and annealed at $180\ °C$. Here are reported the (a) electron map and the presence of (b) Tin, (c) Silver and (d) Chlorine. Table (e) shows weight and percentage of atoms in the sample's surface. 97
4.34 Surface map acquired by EDS of sample doped with $0.2\ mmol$ of Ag and annealed at $180\ °C$. Here are reported the (a) electron map and the presence of (b) Tin, (c) Silver and (d) Chlorine. Table (e) shows weight and percentage of atoms in the sample's surface. 98
4.35 Surface map acquired by EDS of sample doped with $0.4\ mmol$ of Ag and annealed at $180\ °C$. Here are reported the (a) electron map and the presence of (b) Tin, (c) Silver and (d) Chlorine. Table (e) shows weight and percentage of atoms in the sample's surface. 99
4.36 Surface map acquired by EDS of sample doped with $0.1\ mmol$ of Ag and annealed at $300\ °C$. Here are reported the (a) electron map and the presence of (b) Tin, (c) Silver and (d) Chlorine. Table (e) shows weight and percentage of atoms in the sample's surface. 100

4.37 Surface map acquired by EDS of sample doped with $0.2\ mmol$ of Ag and annealed at $300\ °C$. Here are reported the (a) electron map and the presence of (b) Tin, (c) Silver and (d) Chlorine. Table (e) shows weight and percentage of atoms in the sample's surface. 101

4.38 Surface map acquired by EDS of sample doped with $0.4\ mmol$ of Ag and annealed at $300\ °C$. Here are reported the (a) electron map and the presence of (b) Tin, (c) Silver and (d) Chlorine. Table (e) shows weight and percentage of atoms in the sample's surface. 102

4.39 Transfer characteristic curves for the doped samples annealed at (a) $150\ °C$ under DUV, (b) $180\ °C$, and (c) $300\ °C$. In the left y-axis the drain current (I_D) values are reported while in the right y-axis the gate leakage current (I_G) values are reported with dashed lines. All the measures were made with $V_D = 8\ V$ and V_{GS} that sweep from $-8\ V$ to $+8\ V$. The width/length ratio (W/L) is 14 for all the devices. 104

5.1 Energy gap values and error for all the samples analysed in this work which had a reliable value of thickness. 106

List of Tables

2.1 Summary of main physical properties of SnO_2[52]. 45

3.1 Oxidizing and reducing valences of reagents. 48

4.1 pH of solution with $AgNO_3$ by varying the reagents order. 59
4.2 Thickness and energy gap of the samples. χ^2 is referred to the correlation between samples and the models used. 63
4.3 Electrical properties measured using Hall measurement system for sample with $AgNO_3$ annealed at $300\ °C$. 70
4.4 Thickness and energy gap of the samples with different number of layers. Thickness values are referred to samples deposited on $p-Si$ substrate. 74
4.5 Thickness and energy gap of the samples doped with Ag. Thickness values are referred to samples deposited on $p-Si$ substrate. 81
4.6 Root mean square roughness of samples analysed with AFM. . . . 93
4.7 Electrical properties measured using Hall measurement system for the sample doped with $0.1\ mmol$ of Ag annealed at $300\ °C$. . . 103

Introduction

The evolution from rigid silicon-based electronics to low-cost flexible electronics requires the use of solution based production methods. Recently, there has been remarkable development in solution processed inorganic metal oxide semiconductor materials for high-performance Thin Film Transistors (TFTs) and such devices have demonstrated impressive results. The semiconductor oxides reported in the literature are mostly limited to n-type, however, there is still a need for solution processed p-type oxide semiconductors to achieve Complementary Metal Oxide Semiconductors (CMOS) using all oxide materials. One of the most promising candidates for p-type oxide TFTs is Tin oxide: SnO. The production window of solution processed of these materials is narrow so it is important to understand which precursor reagents favor the formation of SnO.

In this work I developed solution processed Tin oxide thin films using solution combustion synthesis and using different Tin ion precursors in order to study the effect of the chemical nature of the reagents on the structural, morphological and electrical properties of the thin films. The process of Solution Combustion Synthesis (SCS) allows to reach the energy-efficient synthesis of bulk materials such as carbides, $III-V$ semiconductors, metal oxides, refractory nitrides and intermetallic compounds by using self-energy generating combustion chemistry. The influence of annealing process and synthesis temperature will also be studied in order to determine the best reaction conditions to obtain high quality materials. The optimized Tin oxide thin films will be integrated in TFTs. Main characterization techniques include XRD, UV-Vis-NIR spectroscopy, Hall effect and electrical characterization of TFTs.

Since obtaining p-type oxide is highly difficult, if this goal is not achieved

the study will be focused on n-type SnO_2 and on the optimisation of devices made with this material, either TFTs or Transparent Conductive Oxides (TCOs).

In the first chapter applications of this devices are presented, such as TFTs and TCOs. Moreover, the solution combustion synthesis technique is explained.

In the second chapter all the physical and electrical properties of Tin, Tin oxide and Tin dioxide are showed and discussed, explaining why this material is so interesting in research.

In the third one, materials and intstruments used are showed and explained, like precursor reagents, deposition features and investigation tools.

In the fourth chapter, finally, all the results obtained from measures and analysis for all the samples made in this work are reported and discussed.

Chapter 1

High mobility oxides: deposition methods and applications

Nowadays the transparent electronic, an emerging field of technology, is replacing classical silicon-based devices. Like conventional electronic, this field requires both n-type and p-type transistor. The development of p-type transparent Thin-Film Transistors (TFTs) and p-type Transparent Conductive Oxides (TCOs) is more difficult than the n-type ones[1]. Developing p-type TFTs would enable the fabrication of complementary metal oxide semiconductor (CMOS), bringing great improvements to optoelectronic devices, such as flat-panel displays, OLEDs and all related applications. The state of the art shows a large success of n-type oxides, that allows the application of transparent conducting oxides and Transparent Semiconductive Oxides (TSO) as active channel layers of Thin-Film Transistors[2][3]. Moreover, p-type oxides are relevant both for TCO and TSO (for fully transparent p-n junctions or p-type TFTs) applications. Until now there were few reports on p-type TCO and no reports at all about p-type oxide TFTs with performance similar to n-type ones. For what concerns TSOs, they are facing exactly the same problems faced by organic TFTs but now in an opposite way, since most of organic TFTs with good electrical performance are p-type[4]. As of today, almost all reported oxide TCOs and TSOs for TFTs are based

on n-type oxides [5]. P-type oxides have very low carrier mobility compared to their n-type counterparts, which is the main obstacle in obtaining high performance TCOs and p-channel oxide TFTs. Recently, much attention has been given to Cu and Sn based semiconductors[1].

In particular, solution-processed amorphous metal oxides, which will be treated in this work, demonstrated exceptional large area uniformity, high dielectric constants and no need for vacuum processing conditions. Their solution processability leads to new possibilities for low cost printable and transparent devices using flexible substrates. The main options to solution process oxide semiconductors are typically spin coating, inkjet-printing, dip-coating and spray-coating[6][7].

In the last years, amorphous metal oxides produced by solution can be compared with oxide semiconductor films developed by physical vapor deposition (PVD), but usually an extra annealing process at high temperatures is necessary to induce a condensed and uniform film, which is not compatible with flexible low cost substrates[8]. Figure 1.1 and Figure 1.2 show a comparison between some properties for materials annealed at different temperatures. In order to solve this problem, researchers tried a new strategy to reduce the temperature needed for the production of solution-processed metal oxide TFTs by using self-energy generating combustion chemistry. The process of solution combustion synthesis (SCS) allows to reach the energy-efficient synthesis of bulk materials such as carbides, $III-V$ semiconductors, metal oxides, refractory nitrides and intermetallic compounds[9].

1.1 Transparent Conductive Oxide

Materials exhibiting both high optical transparency in the visible range of the electromagnetic spectrum and high electrical conductivity (σ) are not common when considering conventional material categories, such as metals, polymers and ceramics. For instance, metals are generally characterized by high electrical conductivity but they are opaque, while ceramics are electrical insulating materials that can be optically transparent, thanks to their typically large bandgap (E_G). Despite that, certain ceramic materials can simultaneously fulfill the requirements of high σ and optical transparency.

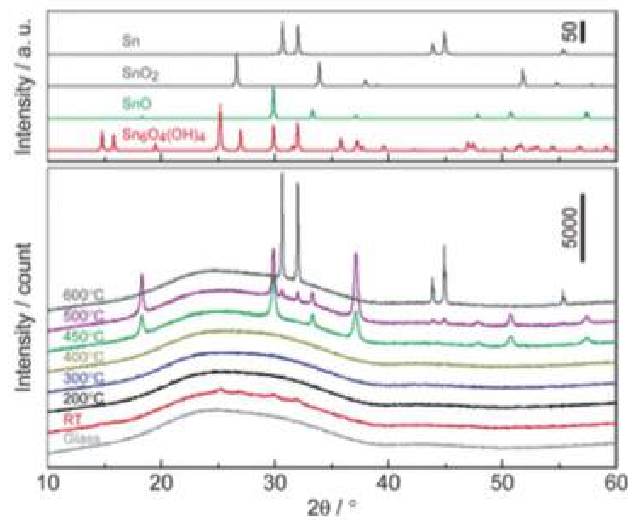

Figure 1.1: X-ray diffractograms calculated on the basis of a reference pattern for $Sn_6O:4(OH)_4$ (ICDD-PDF: $01-084-2157$), SnO (01-072-1012), SnO_2 ($00-041-1445$), and Sn ($00-004-0673$), respectively, with $Cu-K_{\alpha 1}$ and $Cu-K_{\alpha 2}$ diffractions superimposed. In the figure below x-ray diffractograms of thin films annealed at different temperatures. The plot of a bare glass substrate is also given at the bottom as a reference[10].

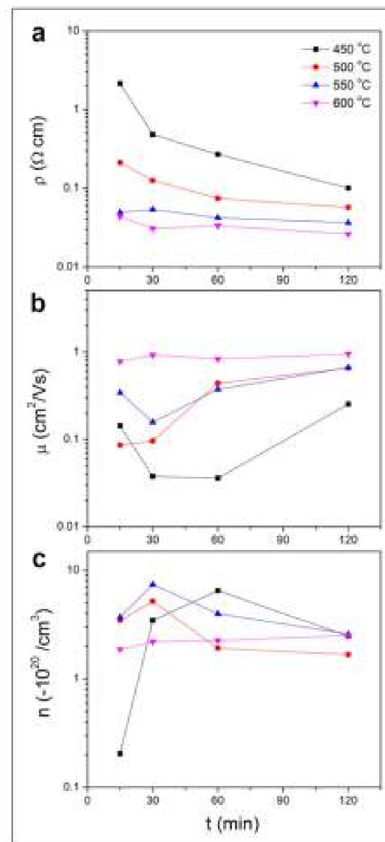

Figure 1.2: Dependence of (a) the electrical resistivity (ρ), (b) the mobility (μ), and (c) the carrier concentration (n) of the Aluminum Tin-Oxide (ATO) films (with thickness of $53\ nm$) on the annealing temperature and time[11].

Transparent Conductive Oxides (TCO) are doped metal oxides used in optoelectronic devices such as flat panel displays and photovoltaics (including inorganic devices, organic devices, and dye-sensitized solar cell). Most of these films are fabricated with polycrystalline or amorphous microstructures.

These materials are called transparent because the transmittance of incident light is more than 80% and their electrical conductivity σ is higher than 10^3 S/cm for efficient carrier transport. For photovoltaic applications the TCOs must have a bandgap E_G greater than 3.2 eV (to avoid light absorption) and a minimum carrier concentration on the order of 10^{20} cm^{-3} for low resistivity [12].

Current transparent conducting oxides used in industry are primarily n-type conductors, meaning their primary conduction is as donors of electrons. This is because electron mobility is typically higher than hole mobility, and because of the difficulty of finding shallow acceptors in wide band gap oxides to create a large hole population. Suitable p-type transparent conducting oxides are still being researched, though the best of them are still orders of magnitude behind n-type TCOs. The lower concentration of carriers of TCOs with respect to metals shift their plasma resonance in the NIR and SWIR range[13].

As said, TCOs are wide band gap semiconducting oxides with high conductivity, which is due to doping either by oxygen vacancies or by extrinsic dopants. The electrical conductivity of n-type TCO thin films depends on the electron density in the conduction band and on their mobility:

$$\sigma = \mu n e \tag{1.1}$$

where μ is the electron mobility, n is its density, and e is the electron charge. The mobility is given by:

$$\mu = \frac{e\tau}{m^*} \tag{1.2}$$

where τ is the mean time between collisions and m^* is the effective electron mass. Due to the large energy gap separating the valence band from the conducting band, the conduction band cannot be thermally populated at room temperature, hence, stoichiometric crystalline TCOs are good insulators[14]. To explain the TCO characteristics, various population mechanisms and several models describing the electron mobility were proposed. Some charac-

teristics of the mobility and the processes by which the conduction band is populated with electrons were shown to be interconnected by electronic structure studies[15], e.g., that the mobility is proportional to the magnitude of the band gap. For intrinsic materials the density of conducting electrons has been attributed to the presence of donor centers, usually metallic interstitials or oxygen vacancies, that produce shallow donor or impurity states located close to the conduction band. Extrinsic dopants have an important role in populating the conduction band, and some of them have been unintentionally introduced. It's the case of SnO_2, where the important role of interstitial Sn in populating the conducting band, in addition to that of oxygen vacancies, was supported by first-principle calculations of Kiliç and Zunger[16]. They showed that Sn interstitials and O vacancies, which dominate the defect structure of SnO_2 due to the multivalence of Sn, explained the natural non-stoichiometry of this material and produced shallow donor levels, turning the material into an intrinsic n-type semiconductor[17]. The electrons released by these defects were not compensated because acceptor-like intrinsic defects consisting of Sn voids and O interstitials did not form spontaneously. Furthermore, due to the large gap between the Fermi level and the energy level of the first unoccupied states, the released electrons did not make direct optical transitions in the visible range. Thus, SnO_2 could have a carrier density with minor effects on its transparency[17].

It is important to know that there is an intrinsic limit of conductivity, due to two main reasons. One is that n and μ cannot be independently increased in TCOs with high carrier concentrations, as they are in competition. At high conducting electron density, carrier transport is limited primarily by ionized impurity scattering i.e., the Coulomb interactions between electrons and the dopants. Higher doping concentration reduces carrier mobility to a degree that the conductivity is not increased, and it decreases the optical transmission at the near-infrared edge[18]. With increasing dopant concentration, the resistivity reaches a lower limit, and does not decrease beyond it, whereas the optical window becomes narrower. The second is that high dopant concentration could lead to clustering of the dopant ions, which increases the scattering rate and could produce non-parabolicity of the conduction band[19].

As said at the beginning of the previous paragraph, TCOs should have low absorption coefficient in the near UV-VIS-NIR region. In the near UV

region the transmission is limited by the energy gap E_G as photons with energy higher than E_G are absorbed. There is a second transmission edge in the NIR region, due to the reflection at the plasma frequency. The optical properties of TCOs transmission T, reflection R and absorption A, are determined by its refraction index n, extinction coefficient k, band gap E_G, and geometry. Geometry includes film thickness, thickness uniformity, and film surface roughness. T, R and A are intrinsic, depending on the chemical composition and solid structure of the material, while the geometry is extrinsic. Moreover, there is a negative correlation between the carrier density and the position of the IR absorption edge, but positive correlation between the carrier density and the UV absorption edge, as E_G increases at larger carrier density (Moss-Burstein effect). As a result, the TCO transmission boundaries and conductivity are interconnected. The state of the art for the industry standard in TCOs is Tin-doped Indium Oxide (ITO). This material shows resistivity of the order $\sim 10^{-4}\ \Omega \cdot cm$ and very high transmittance (greater than 80%)[20]. The drawback for this material is its cost, due to the price of Indium. Other materials, like doped binary compounds such as Aluminum-doped Zinc-Oxide (AZO), Indium-doped Cadmium-Oxide and Tin Oxide have been proposed as alternative materials. This is because AZO is composed of Aluminum and Zinc, two common and inexpensive materials, such as Tin, while Indium-doped Cadmium oxide only uses Indium in low concentrations. Other novel transparent conducting oxides include Barium stannate and the correlated metal oxides Strontium Vanadate and Calcium Vanadate.

Currently, researchers are trying to optimize the electrical and optical characteristics of TCOs by changing the deposition method and parameters, like temperature or pressure.

1.2 Thin Film Transistor

A Thin Film Transistor (TFT) is a special kind of field-effect transistor made by depositing thin films of an active semiconductor layer, a dielectric layer and metallic contacts over a non-conducting supporting substrate. It has a gate electrode which works like a switch to open or close two other electrodes, the source and the drain, where a vertical electrical field is applied

forming a conducting channel, as shown in Figure 1.3[21].

Unlike classical Metal-Oxide-Semiconductor Field-Effect Transistor (MOSFET), where the substrate is an active part of the device (usually monocrystalline silicon), TFTs allow separating elements in an integrated circuit and the substrate can be of any form, such as a flexible substrate. Even though this is an advantage, the fabrication process of TFTs is now limited in temperature: since the substrate is usually made of glass or a polymeric material, the maximum processing temperature is around 650 $°C$, while the monocrystalline silicon allows higher process temperature[22].

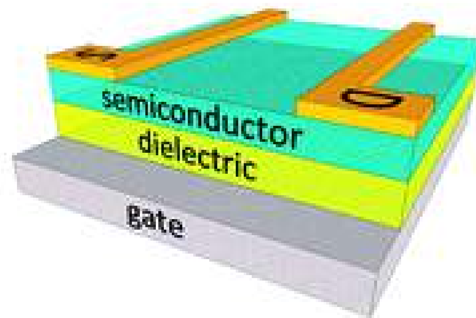

Figure 1.3: Structure of a TFT in a configuration staggered bottom-gate with the region of the channel depicted.

There are four possible TFT structures as shown in Figure 1.4. They can be either staggered or coplanar. In a coplanar configuration the source, the drain and the insulator contacts are on the same side of the semiconductor and the source-drain contacts are in direct contact with the induced channel. In a staggered configuration, the source and the drain contacts are on the opposite side of the semiconductor from the insulator and there is no direct connection to the induced channel. Each one of these structures could be classified as bottom-gate (inverted) or top-gate (normal) device. A bottom-gate TFT has the gate insulator and gate electrode located beneath the semiconductor. A top-gate TFT has the gate and the insulator located on top of the semiconductor. In a top-gate device, the semiconductor is covered by a gate insulator, so the top surface is inherently passivated. In the experiments that lead to this thesis, oxide semiconductors were produced and applied as active layer in staggered bottom-gate Thin Film Transistors.

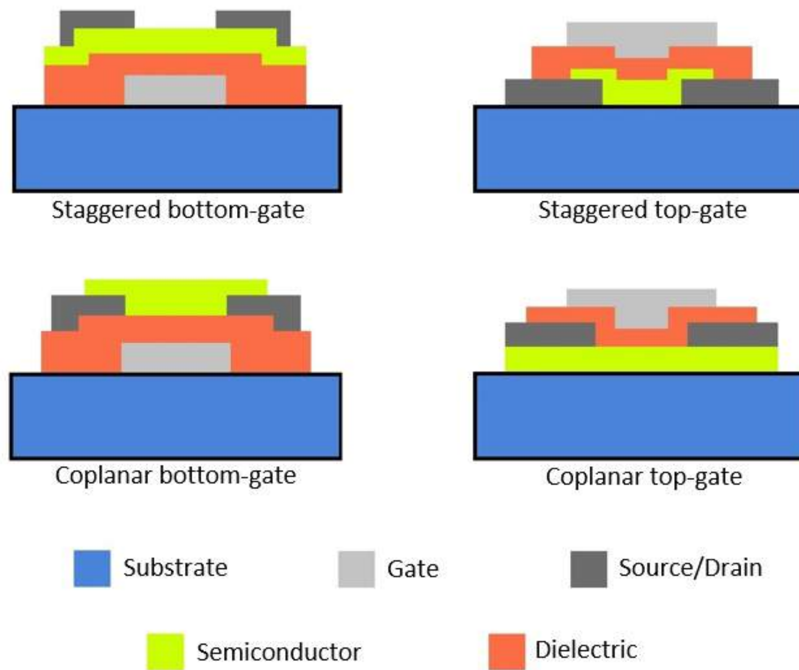

Figure 1.4: Comparison between TFT structures.

The following explanations about how TFT works will be done considering p-type TFT. The behavior of n-type TFTs is similar, but the sign of the polarizations is the opposite and the majority carriers are electrons instead of holes.

The initial condition is with no voltage applied to gate electrode (V_{GS}): the free carriers are homogeneously distributed in the semiconductor layer. If the semiconductor examined has low density of charge carriers, the conductivity in the active layer will be very low as well as the current between the source and drain electrodes resulting from the applications of an electric field between them. This state is called Off State and the resulting current is called Off Current (I_{DSoff})[24].

When a negative voltage is applied to the gate electrode, there will be an excess of majority carriers that will be attracted to the surface of the p-type semiconductor, near to the interface with the dielectric. The charge density of this thin layer increases, creating a conductive channel between the source and the drain. The application of an electric field between the source and drain electrodes (V_{DS}) will result in a current flow between them.

This current is called On Current (I_{DSon}) because the device is at On state [25].

Applying different voltages in the gate electrode it is possible to describe the operation of a TFT analysing the energy band diagram of the capacitor comprised by the gate electrode, the dielectric and the semiconductor. When the capacitor is biased with positive or negative voltages, three cases may exist. When a negative voltage is applied to the gate electrode, the valence band edge, E_V, bends upward near to the surface and it is closer to Fermi level and the semiconductor/insulator interface has an accumulation of holes (a channel has formed), since the carrier density depends exponentially on the energy difference ($E_F - E_V$). This is called the accumulation case. When a positive voltage is applied, the band bends downward and the majority carriers are depleted (depletion case); when a larger positive voltage is applied, the band bends even more downward so that the intrinsic level E_i at the surface crosses over the Fermi level E_F (inversion state) and the number of electrons at the surface is larger than the number of holes.

P-type TFTs can operate in enhancement or depletion modes, depending if the threshold voltage (V_T) is negative or positive. For TFTs that operate in enrichment mode, the conductivity of the channel for a zero bias gate voltage is zero (off-state) and a negative gate voltage is required to put the device at on-state. For a device that operates in depletion mode, the device is already on even without a gate voltage being applied and is necessary to apply a V_{GS} to achieve the off-state. Depletion mode devices are less desirable because they require more energy to keep the device off.

As said before, applying a negative voltage V_{GS}, higher than V_T in module, let the TFT to operate in accumulation mode and, if the active layer is a p-type, accumulated charges are holes. Depending on the value of V_{DS}, different operation regimes can be observed during the on-state: the linear regime and the saturation regime[26].

In linear regime, I_{DS} is described by:

$$I_{DS} = \frac{W}{L} C_i \cdot \mu_{FE} \cdot [(V_{GS} - V_T)V_{DS} - \frac{1}{2}V_{DS}^2] \qquad when \ \ V_{DS} < V_{GS} - V_T \quad (1.3)$$

where W is the channel width, L is the channel length, C_i is the gate capacity per unit area and μ_{FE} is the field-effect mobility. For very low

V_{DS}, the quadratic term can be neglected, yielding a linear relation between I_{DS} and V_{DS}. In this case, the accumulated charges are considered to be uniformly distributed throughout the channel[27].

In the saturation regime, I_{DS} is described by:

$$I_{DS} = \frac{W}{2L} C_i \cdot \mu_{sat} \cdot (V_{GS} - V_T)^2 \qquad when \;\; V_{DS} > V_{GS} - V_T \tag{1.4}$$

where μ_{sat} is the saturation mobility. In this regime, the semiconductor close to the drain region becomes depleted, a phenomenon designated by pinch-off that leads to the saturation of I_{DS}.

In Figure 1.5 the static characteristics of TFTs are visible: the output and transfer characteristics.

In the output characteristics, V_{DS} is swept for different V_{GS} values, allowing one to observe clearly the linear and saturation regimes described above. The transfer characteristic, where V_{GS} is swept for a constant V_{DS}, allows to extract a large number of quantitative electrical parameters, like On/Off ratio, threshold voltage (V_T), turn-on voltage (V_{on}), mobility (μ) and subthreshold slope (S) that will be described below[22].

Threshold voltage V_T corresponds to the V_{GS} for which an accumulation layer or conductive channel is formed close to the dielectric/semiconductor interface. V_T can be calculated at low V_{DS} (linear regime) doing a linear extrapolation of the $I_{DS} - V_{GS}$ plot or at high V_{DS} (saturation regime) doing an extrapolation from $\sqrt{I_{DS}} - V_G$ plot.

Mobility of a TFT can be extracted using different methods, which are described below:

- Effective mobility (μ_{eff}). It can be estimated at low V_{DS} by the conductance of the device (g_d), given by[28]:

$$g_d = \left(\frac{\partial I_D}{\partial V_{DS}} \right) = \mu_{eff} C_i \frac{W}{L} (V_{GS} - V_T) \tag{1.5}$$

  obtaining:

$$\mu_{eff} = \frac{g_d}{C_i \frac{W}{L} (V_{GS} - V_T)} \tag{1.6}$$

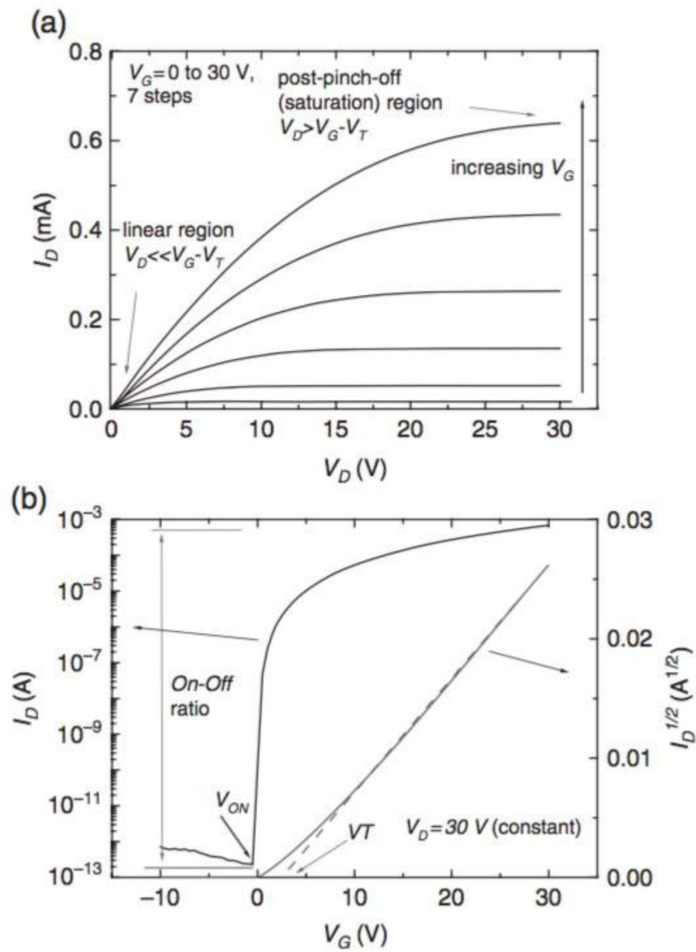

Figure 1.5: Typical a) output and b) transfer characteristics of a n-type oxide TFT[23].

- Field effect mobility (μ_{FE}). It can be estimated at linear regime from the transconductance (g_m), which is defined as:

$$g_m = \left(\frac{\partial I_D}{\partial V_{GS}} \right) \Bigg|_{V_{DS}} \tag{1.7}$$

and μ_{FE} is given by:

$$\mu_{FE} = \frac{g_m}{C_i \frac{W}{L} V_{DS}} \tag{1.8}$$

- Saturation mobility (μ_{sat}). It can be estimated by differentiating $\sqrt{I_{DS}}$ as a function of V_{GS}:

$$g_m = \left(\frac{\partial \sqrt{I_D}}{\partial V_{GS}} \right) \Bigg|_{V_{DS}} = \sqrt{\frac{W}{2L} \mu_{sat} C_i} \tag{1.9}$$

where μ_{sat} is given by:

$$\mu_{sat} = \frac{\left(\frac{\partial \sqrt{I_D sat}}{\partial V_{GS}} \right)^2}{\frac{W}{2L} C_i} \tag{1.10}$$

The field effect mobility is usually lower than the effective mobility, because the dependence of mobility on electric fields is neglected through g_m. Major differences can be often observed between the mobilities calculated from linear and saturation regions. μ_{FE} can be affected by problems from source and drain contacts and in such cases there are deviations regarding the linearity of $I_{DS} - V_{DS}$ curve, underestimating the value of μ_{FE}. For saturation regime, when the channel width has the same dimension of dielectric thickness, $I_{DS} - V_{DS}$ curve does not show saturation and exhibits high values, leading to incorrectly high values of μ_{sat}.

The subthreshold slope (S) is defined as the V_{GS} needed to increase I_{DS} by one decade and is given by the inverse of the maximum slope of the transfer characteristic:

$$S = \left(\left| \frac{\partial \log(I_D)}{\partial V_{GS}} \right| \right)^{-1} \tag{1.11}$$

High μ_{FE} leads to high saturation current and fast switching speed between on/off states, low subthreshold slope and high on/off ratio values indicate efficient and effective modulation of I_{DS} with V_G; V_T close to zero ensure low power consumption.

1.3 Solution combustion synthesis

As said at the beginning of this chapter, the development of large-area, low-cost electronics for flat-panel displays and flexible circuitry depends heavily on high-throughput fabrication processes and a choice of materials with appropriate performance characteristics. For different applications, high charge carrier mobility, high electrical conductivity, large dielectric constants, mechanical flexibility or optical transparency may be required. Although thin films of metal oxides could potentially meet all of these needs, as of today they are deposited using slow, labour-intensive and expensive techniques such as sputtering[29].

In the last years, amorphous metal oxides produced by solution can be compared with oxide semiconductor films developed by Physical Vapor Deposition (PVD), but usually an extra high-temperature annealing process is necessary to induce a condensed and uniform film, which is not compatible with flexible low cost substrates[30].

For low-temperature solution-based oxide film fabrication, a promising approach would be via a localized heating mechanism analogous to low-temperature $poly - Si$ laser crystallization. However, for the present wide bandgap oxides, this would require expensive ultraviolet lasers and would risk damaging other materials in the device.

For this reason, recently, researchers found a new technique to solve the problem of high temperature for the production of solution-processed metal oxide TFTs: using self-energy generating combustion chemistry, the Solution Combustion Synthesis (SCS).

The SCS technique is based on the use of saturated aqueous solution of a metal nitrate as oxidizing agent and a suitable organic fuel employed as reducing agent. This redox mixture ignites upon heating at a determined temperature, usually below 300°C, to initiate a self-propagating exothermic reaction that sustains high temperatures for a sufficient period of time to

decompose all the organic material and metal salts. The final product is usually a crystallized material with nanometric size clusters.

It is important to notice that the type of organic fuel needs to be specific for the metal employed for the SCS and the type of mixed metal oxide formed. Moreover, the structure and/or surface properties of the final product obtained using SCS method are influenced not only by the nature or type of fuel but also by the fuel-to-oxidizer ratio. Furthermore, an additional thermal treatment could be applied in order to burn residual carbonaceous material.

Solution Combustion Synthesis offers many reasons to be attractive for film solution processing. First, the generation of high local temperatures without a furnace, that enables low-cost large-scale bulk syntheses, and the high self-generated energies that can convert precursors into the corresponding oxides at low process temperatures. Second, oxide formation via conventional precursors based on metal hydroxide and/or alkoxide conversion is endothermic, requiring significant external energy input to form metal-O-metal lattices, whereas combustion synthesis is exothermic, not requiring external energy input once ignited. Furthermore, conventional processes and precursors typically require high temperatures for oxidizing organic impurities to achieve phase-pure products, whereas in combustion reactions with balanced redox chemistry, the atomically local oxidizer supply can efficiently remove organic impurities without coke formation.

The heat required for the material synthesis is supplied by the resulting redox after ignition. The self-generated heat of synthesis provides a localized energy supply, eliminating the need for a high, externally applied processing temperature and results in the final solid phase formation, as shown in Figure 1.6.

In order to calculate the oxidizing/reducing valencies of a redox mixture we will use the method introduced by Jain[31].

The fuel "richness" or "leanness" of a combustible mixture is usually determined by the equivalence ratio ϕ, which is defined as

$$\phi = \frac{\phi_s}{\phi_m} \tag{1.12}$$

where ϕ_m is the mixture ratio (fuel/oxidizer) and ϕ_s is the stoichiometric ratio[32].

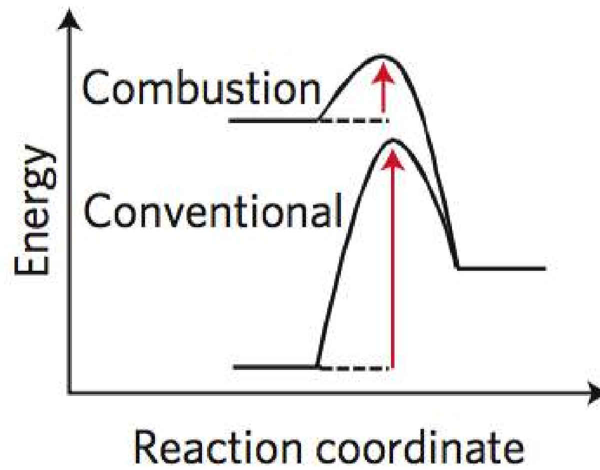

Figure 1.6: Comparison of the energy required for a conventional reaction relatively to a combustion one.

The optimal stoichiometric composition of the redox mixture is achieved when no molecular oxygen is required (i.e., $\phi = 1$). When ϕ is below unit ($\phi < 1$) the redox mixture is under fuel-lean regime and molecular oxygen is produced. On the other hand, when $\phi > 1$ the redox mixture is under fuel-rich condition, requiring molecular oxygen to fully convert the fuel. At optimal stoichiometric composition ($\phi = 1$) and fuel-rich condition the reaction releases the maximum energy.

Another parameter called "elemental stoichiometric coefficient" (ϕ_e) was suggested by Bakhman[33] which reflects the relationship between the intramolecular "fuel" and "oxidizer." Whereas $\phi_e = \phi = 1$ for stoichiometrically balanced compositions, they may differ substantially at other compositions. The deviations become more apparent when the fuel contains the "oxidizer" and the oxidizer contains "fuel" elements.

All the oxidizing and reducing elements are treated in a similar manner irrespective of whether they are present in the oxidizer or the fuel components. ϕ_e is defined as:

$$\phi_e = \frac{Total\ composition\ of\ oxidizing\ elements}{Total\ composition\ of\ reducing\ elements} = \tag{1.13}$$

$$= \frac{\sum Coefficient\ of\ oxidizing\ elements}{(-1)\sum Coefficient\ of\ reducing\ elements} = \tag{1.14}$$

$$= \frac{p}{r} \tag{1.15}$$

where p and r are integers representing the total composition of the oxidizing and the reducing elements respectively in the mixture.

In this method, metals, carbon and hydrogen are considered as reducing elements with the corresponding metal valence, $+4$ for carbon and $+1$ for hydrogen. On the other hand, oxygen is seen as an oxidizer with valence -2 and nitrogen is considered with valence 0. Hydration water does not affect the overall compound valence. The full calculation for the samples used in this work will be shown later.

It is important to note that these calculations are based on a theoretical reaction equation that neglects possible secondary reactions such as urea hydrolysis, thermal decomposition, fuel-oxidizer adduct and also nitrates decomposition that could vary the initial fuel-to-oxidizer ratio.

Chapter 2

Tin oxide

Tin (Sn) is a chemical element with atomic number 50. It is a post-transition metal in group 14 of the periodic table and it has two main oxidation states, +2 and +4, which is slightly more stable. It has two main allotropes: at room temperature, the stable allotrope is $\beta - Tin$, a white malleable metal with tetragonal structure and, at lower temperatures, the allotrope is $\alpha - Tin$, which is less dense, grey, has a diamond cubic structure and has no metallic properties at all. For the purpose of this thesis we are interested in the inorganic compounds that Tin can form, more precisely it can form two oxides: Tin (II) oxide (Stannous oxide, SnO) and Tin (IV) dioxide (Stannic oxide, SnO_2).

Stannous oxide is not as well characterized as SnO_2. For example, its electronic band gap is not accurately known but lies somewhere in the range of $2.5 - 3$ eV. Thus, SnO exhibits a smaller band gap than SnO_2, which is commonly quoted to be 3.6 eV. Also, there are no single crystals available that would facilitate more detailed studies of stannous oxide. Stannic oxide possesses the rutile structure and stannous oxide has the less common litharge structure. Stannic oxide is the more abundant form of Tin oxide and is the one of technological significance in gas sensing applications and oxidation catalysts. In addition to the common rutile (tetragonal) structured SnO_2 phase there also exists a slightly more dense orthorhombic high pressure phase.

Figure 2.1 shows the $Sn - O$ phase diagram for atmospheric pressure [34].This diagram indicates the presence of an intermediate Tin-oxide phase

Figure 2.1: $Sn - O$ phase diagram[34].

between SnO and SnO_2 at elevated temperature. Sn_3O_4 is often given for its composition but Sn_2O_3 has also been considered. In these intermediate oxides Sn is present as a mixture of Sn (II) and Sn (IV)[35]. The formation heats for stannous and stannic oxides at 298 K were determined to $\Delta H = -68$ cal/mol and $\Delta H = -138$ cal/mol, respectively[36]. This results in $\Delta H = -70$ cal/mol for the reaction $SnO(c) + 1/2O_2(g) \rightarrow SnO_2(c)$. Also the disproportionation reaction of $SnO(c) \rightarrow Sn_xO_y(c) + Sn \rightarrow SnO_2(c) + Sn$ has been reported to occur at elevated temperatures[37]. This disproportionation of SnO into Sn and SnO_2 proceeds via the aforementioned intermediate oxides. This indicates that stannic oxide is the thermodynamically most stable form of Tin oxide. The oxidation of SnO films to SnO_2 has been studied by Raman scattering, IR reflectivity and X-ray diffraction[38]. It was found that the oxidation starts with an internal disproportionation before external oxygen completes the oxidation to SnO_2. More importantly, (001)-textured SnO layers convert into (101)-textured SnO_2 films. The same behavior was observed by Geurts et al.[38]; they explain this considering the structural similarities between the Tin matrix of the SnO (001) plane and that of the SnO_2 (101) plane. Because of this structural similarity, just the incorporation of an additional oxygen layer is required to obtain the final SnO_2

structure. For comparison Figure 2.2 shows the top views of SnO (001) and SnO_2 (101). A more detailed discussion of the structure of SnO and SnO_2 is given next.

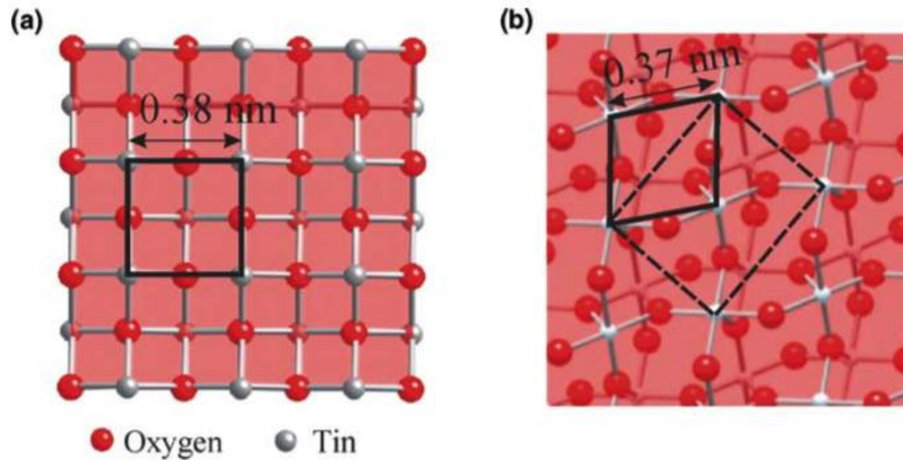

Figure 2.2: Comparison of the structure of the (a) SnO (001) and (b) SnO_2 (101) surfaces.

2.1 SnO

The crystal structure of stannous oxide (SnO) is shown in Figure 2.3.

It has a tetragonal unit cell with the litharge structure, isostructural to PbO. The symmetry space group is $P4/nmm$ and the lattice constants are $a = b = 3.8029$Å and $c = 4.8382$ Å[169]. Each Sn and O atom is fourfold coordinated with a bond length of 2.23 Å. The structure is layered in the (001) crystallographic direction with a $Sn_{1/2} - O - Sn_{1/2}$ sequence and a van der Waals gap between two adjacent Sn planes of 2.52 Å. The positive charge of the Sn^{2+} ions is screened by electron charge clouds between the Sn planes, thus reducing the Coulombic repulsion between adjacent Sn layers [39]. These charge clouds, or charge hats, arise from Sn 5s electrons that do not participate in the bonding for $Sn(II)$ and thus can be described as a lone pair.

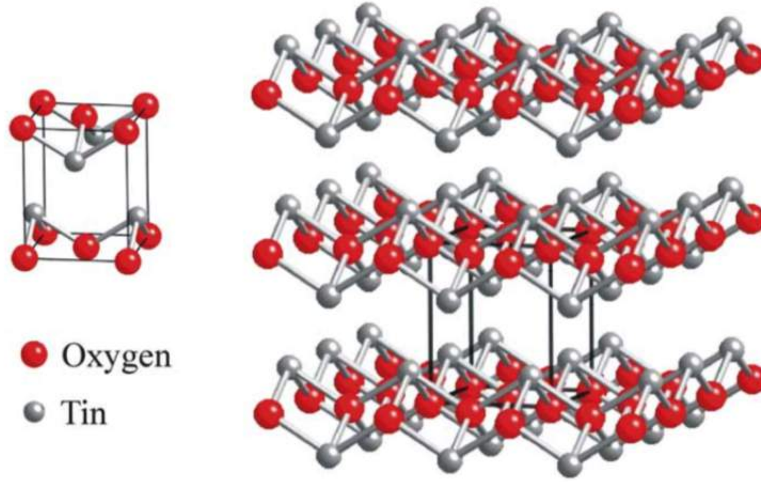

Figure 2.3: Ball-and-stick model of the litharge structure of SnO.

A change in the surface electronic structure may be expected for a variation in the surface composition. Reduction of the surface converts the surface Sn cations from a (IV) to a (II) valence state. Thus, the Sn $5s$ states that are predominantly empty for Sn (IV) are becoming filled for Sn (II) and form part of the valence band. As pointed out before, Sn $5s$ lone pair charge clouds are present in stannous oxide and thus some similarities between the surface electronic structure of reduced SnO_2 surfaces and bulk stannous oxide may be anticipated with Sn $5s$ lone pair electrons forming states confined to the surface layer. A comparison between SnO and SnO_2 band structure is shown in Figure 2.4.

The defect analysis in SnO shows O_i and V_{Sn} as the most favorable defect states under O rich conditions. However, O_i does not contribute to the hole electrical conductivity as it is not likely to get ionized at normal temperatures. The formation energy for Sn_i is high and not very likely to affect the electronic properties of SnO. On the other hand, V_{Sn} introduces acceptor like defects near valence band maximum (VBM) and is not found to affect the lone pair electron distribution in the open space[40]. Almost similar predictions were made by hybrid-DFT analysis performed by Allen et al.[41]. The observed p-type conductivity in SnO can be then considered mainly as a consequence of Sn vacancy rather than O interstitial. Experimentally, p-type conduction was reported in cation deficient SnO thin films. Pan et al.[42]

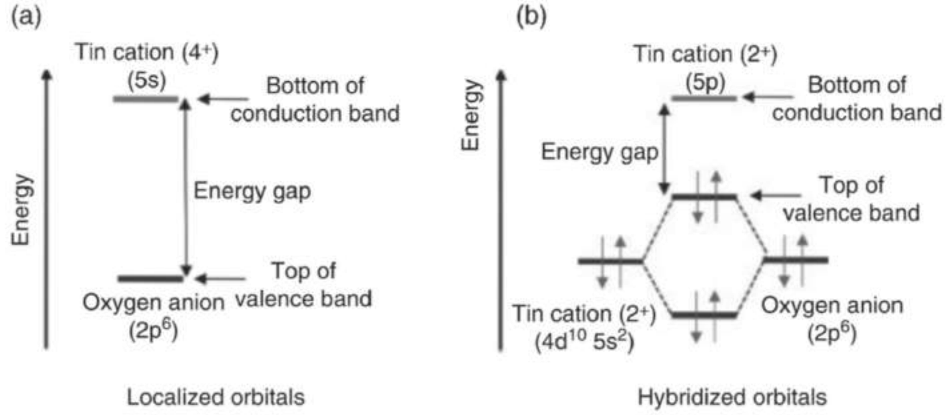

Figure 2.4: Comparison between the band structure of a) SnO_2 and b) SnO[23].

suggested that in this situation some of the Sn atoms transform to Sn^{3+} state to maintain the charge neutrality. This transformation is equivalent to Sn^{2+} and a weakly bonded hole. Deposition conditions greatly affect the electronic properties of the resulting SnO thin films. Deposition at reduced oxygen pressure reduces the O chemical potential relative to Sn chemical potential which favors small defect formation energies for p-type defects such as O_i and V_{Sn}[41].

Raman or infrared spectroscopy can be used to differentiate SnO from SnO_2. This has been utilized for example in order to investigate the oxidation processes of Sn. Phonon modes that cannot be assigned to either SnO nor SnO_2 are sometimes observed in oxidation studies of Sn or SnO and this has been taken as evidence for the intermediate Tin oxide phase with Sn_2O_3 or Sn_3O_4 mentioned before.

For SnO group theory gives the following vibrational modes[38]:

$$\Gamma = A_{1g} + B_{1g} + 2E_g + A_{2u} + E_u + 3 \ acoustic \ modes \tag{2.1}$$

In the IR modes the Tin sublattice is displaced with respect to the oxygen sub-lattice. This displacement gives rise to a dipole moment. For the A_{2u} mode this points in the c-direction (IR polarization $E \parallel c$) but for the E_u mode its orientation is perpendicular to the c-axis (IR polarization $E \perp c$).

For what concerns SnO thin films, since SnO is not a thermodynamically stable material, most of the PVD growth methods have a very narrow process window to get phase pure SnO thin films, particularly if metallic Sn is the

target material. Phase purity of the deposited films strongly depends on the deposition conditions like oxygen partial pressure, deposition rate, growth temperature and energy involved in the process. Metastability of SnO causes the coexistence of metallic Sn or SnO_2 phases along with SnO phase in the thin films. This often makes the quantitative analysis of the chemical composition of the deposited thin films essential. [43]

It has been reported that SnO possesses both direct and indirect bandgaps. Computational studies suggest an indirect bandgap of $0.3 - 0.6\ eV$, which is slightly less than experimentally reported values[44]. These smaller values are often the result of underestimation of excited states energy in DFT calculation. Hybrid DFT analysis, with empirical dispersion corrections, showed an improvement in the band structure, predicting the indirect bandgap value $0.61 - 0.67\ eV$ and direct bandgap value $2.6 - 2.76\ eV$, which are in good agreement with the experimental values[45].

It is believed that the p-type conductivity of SnO can be further improved by proper doping. However, there are only a few literature reports on metal-doped SnO, and the doping effects thereof. Guo et al. speculated that an increase in the concentration of Y doping in the SnO [46], a deterioration of crystallinity and an increase in optical bandgap of SnO have been observed. Ahn et al. reported that increasing Mg doping concentration in SnO thin films results in lower crystallite size and higher resistance [47]. In this context, there is an extreme need to develop methods to produce p-type metal-doped SnO thin films. The successful preparation of this material may have a promising future in the next-generation transparent semiconducting oxide for application in novel optoelectronic devices. In this work, Ag-doped SnO is used, in order to promote the SnO creation instead of SnO_2. Upon increasing the Ag dopant concentration, Sn^{2+} ions were replaced with Ag^{+} ions, which results in a smaller crystallite size. Ag-doped SnO thin films exhibited a p-type semiconductor behavior, with a direct optical gap and decreasing transmittance as a function of increasing Ag dopant concentration[48].

In conclusion, bipolar conduction process in SnO makes it an ideal material for developing transparent homo-junction devices even on flexible substrates. However, achieving high conductivity and mobility in SnO is still a challenge. The mechanism of doping in SnO is not clear yet, as there are controversial reports of creating donor-like and acceptor-like defects with the

same type of dopants.

2.2 SnO_2

SnO_2 belongs to the important family of oxide materials that combine low electrical resistance with high optical transparency in the visible range of the electromagnetic spectrum. Another property of SnO_2 is that although it is transparent in the visible, it is reflective for infrared light. This property is responsible for the use of SnO_2 as an energy conserving material.

SnO_2 is an n-type wide bandgap semiconducting material with wide direct bandgap energy of 3.6 eV and indirect bandgap of 2.6 eV[49], where inherent oxygen vacancies act as an n-type dopant[50].

Stannic oxide (SnO_2) is much better characterized than stannous oxide. As a mineral, stannic oxide is also called Cassiterite. It possesses the same rutile structure as many other metal oxides, e.g. TiO_2, RuO_2, GeO_2, MnO_2, VO_2, IrO_2, and CrO_2. The rutile structure has a tetragonal unit cell with a space-group symmetry of $P42/mnm$. The lattice constants are $a = b = 4.7374$ Å and $c = 3.1864$ Å[51]. In the bulk all Sn atoms are sixfold coordinated to threefold coordinated oxygen atoms. A representation of the unit cell can also be found in Figure 2.5.

As for stannous oxide, the phonon vibrational modes for stannic oxide are reported. For SnO_2 the six unit cell atoms give rise to 18 vibrational modes:

$$\Gamma = A_{1g} + A_{2g} + B_{1g} + B_{2g} + E_g + 2A_{2u} + 2B_{1u} + 4E_u \tag{2.2}$$

Of these 18 modes, two are IR active (the single A_{2u} and the triply degenerated E_u mode), four modes are Raman active (three non-degenerate modes, A_{1g}, B_{1g}, B_{2g} and the doubly degenerate E_g) and two are silent (A_{2g} and B_{1u}). One A_{2u} and two E_u modes are acoustic. In the Raman active modes the oxygen atoms vibrate while the Sn atoms are at rest. The non-degenerate modes, A_{1g}, B_{1g}, and B_{2g} vibrate in the plane perpendicular to the c-axis while the doubly degenerate E_g mode vibrates in the direction of the c-axis. The B_{1g} mode consists of rotation of the oxygen atoms around the c-axis, with all six oxygen atoms of the octahedral participating in the

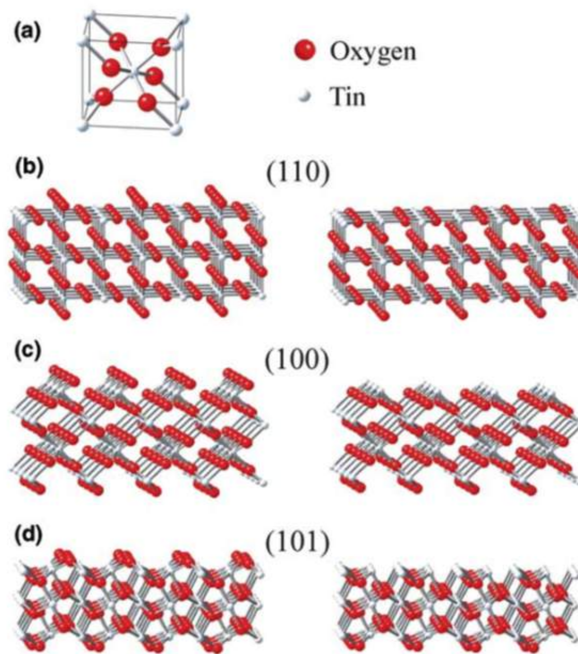

Figure 2.5: Ball-and-stick models of SnO_2, low index surfaces. The bulk rutile-unit cell is shown in (a). (b), (c), and (d) show bulk termination of the (110), (100), and (101) surfaces respectively. On the left-hand side stoichiometric bulk terminations are represented. On the right-hand side surfaces with reduced oxygen concentration are indicated.

vibration. In the A_{2g} infrared active mode, Sn and oxygen atoms vibrate in the c-axis direction, and in the E_u mode both Sn and O atoms vibrate on the plane perpendicular to the c-axis. The silent modes correspond to vibrations of the Sn and O atoms on the direction of the c-axis (B_{1u}) or in the plane perpendicular to this direction (A_{2g}).

For bulk terminated SnO_2 surfaces, i.e. surfaces with surface-Tin atoms in their bulk Sn^{4+} oxidation state, the (110) surface exhibits the lowest surface energy followed by the (100), (101), and (001) surfaces.

Representations of the bulk terminated surfaces are shown in Figure 2.5, left side panels. These surfaces are constructed in an autocompensated way, i.e. the same number of Sn-to-O as O-to-Sn bonds are cut. This is a rule that often allows assessing the most likely surface termination of ionic crystals.

A summary of physical properties of SnO_2 is given in Table 2.1.

Property		**Property**	
Mineral name	Cassiterite	Melting point [$°C$]	> 1900
Crystal structure	Tetragonal, rutile	Melting point of metal [$°C$]	232
Space group	$P4_2mnm$	Heat of formation [eV]	6.0
Lattice constants [nm]	$a = 0.474$ $b = 0.319$	Static dielectric constant ϵ_T	$\parallel c : 9.6$ $\perp c : 13.5$
Density ρ [$g \cdot cm^{-3}$]	6.99	Band gap [eV]	3.6
Mohs hardness	6.5	Common extrinsic n-type dopants	Sb, F, Cl

Table 2.1: Summary of main physical properties of SnO_2[52].

Due to its wide band-gap SnO_2 is a good TCO material. Often, in these materials, the highest possible conductivity is sought. Many of the binary TCOs already possess a high conductivity due to intrinsic defects, i.e. oxygen deficiencies. This is also the case for SnO_2, which in its stoichiometric form is a good insulator. However, non-stoichiometry, in particular oxygen deficiency, makes it a conductor. In all applications of these materials the charge carrier concentration and thus the conductivity is further increased

by extrinsic dopants. In the case of SnO_2 these are commonly Sb as a cation dopant and F as an anion dopant[53]. Although these dopants increase the conductivity of SnO_2 significantly, it does not reach the low conductivity values achievable with ITO or with doped ZnO. Figure 2.6 shows the progress that has been made in reducing the resistivities of these three materials from 1970 to 2000.

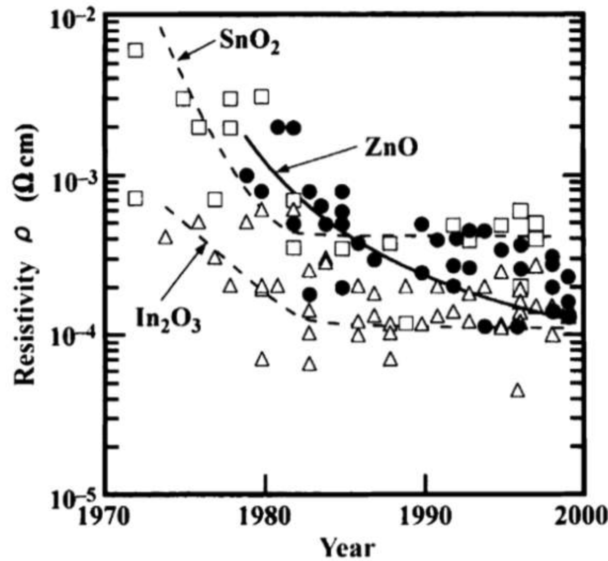

Figure 2.6: Decrease of the resistivity for TCO materials from 1970 to 2000[54].

The undoped SnO_2 has low electrical resistance and high optical transparency in the visible range of the electromagnetic spectrum. These properties make Tin oxide thin films suitable for many applications, particularly as an electrode material in solar cell, light emitting diodes, transparent electromagnetic shielding materials, etc[55]. Perfectly amorphous thin SnO_2 films show good electrical response to reducing gases in air and could hence be applied to construct semiconductor gas sensors where the metal oxide films function as a monograin-equivalent active layer[56].

Chapter 3

Materials and method

In this chapter all the techniques involved in the production and the characterization of the films and the devices will be presented. In this thesis work all the thin films were produced by spin coating and their optical, morphological, structural and electrical properties were characterized by a variety of techniques, that will be showed in the following sections.

3.1 Precursors solution

The solutions used were $0.1M\ SnO_x$ in $10\ mL$ of 2-methoxyethanol prepared using the solution combustion synthesis (SCS) with different precursors, as showed in the following equations:

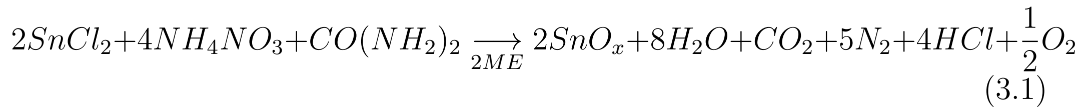

$$2SnCl_2 + 4NH_4NO_3 + CO(NH_2)_2 \underset{2ME}{\longrightarrow} 2SnO_x + 8H_2O + CO_2 + 5N_2 + 4HCl + \frac{1}{2}O_2 \tag{3.1}$$

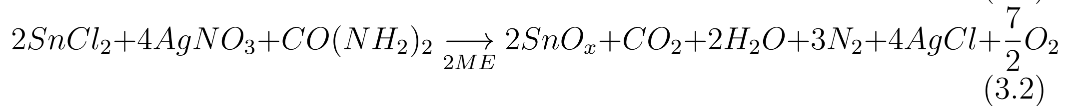

$$2SnCl_2 + 4AgNO_3 + CO(NH_2)_2 \underset{2ME}{\longrightarrow} 2SnO_x + CO_2 + 2H_2O + 3N_2 + 4AgCl + \frac{7}{2}O_2 \tag{3.2}$$

The precursor solutions were prepared with Tin (II) Chloride ($SnCl_2$, Sigma Aldrich, 99%) and Ammonium Nitrate (NH_4NO_3, Carl Roth, 98%) or Silver Nitrate ($AgNO_3$, Sigma Aldrich, 99%) dissolved in 2-Methoxyethanol ($2-ME$, Sigma Aldrich, $99,5\%$). For combustion reaction precursor solutions, the fuel, Urea (CH_4N_2O, Sigma Aldrich, 98%) was added to the prepared solutions which were maintained under constant stirring for at least

1 h.

All the equations are balanced in order to set the fuel/oxidation ratio ϕ, introduced in the first chapter, equal to 1.

To ensure the redox stoichiometry of the reaction, using the relationship between redox stoichiometry and the molar ratio of the reactants, it is necessary to determine the valence of the reducing/oxidizing reagent (RV:OV)[57]:

$$\phi = \frac{RV}{OV} \cdot n \iff n = 1 \cdot \frac{OV}{RV} \tag{3.3}$$

Where n is the number of moles of fuel per mole of oxidant. In order to get $\phi = 1$, we have to calculate the oxidizing/reducing valences of a redox mixture. Metals, carbon and hydrogen are considered as reducing elements with the corresponding metal valence, +2 for Tin (II), +4 for Carbon and +1 for Hydrogen. Oxygen is seen as an oxidizer with valence −2 and Nitrogen is considered with valence 0[58].

As for the reaction with $AgNO_3$, before calculations, is necessary to note the reduction reaction between $SnCl_2$ and $AgNO_3$:

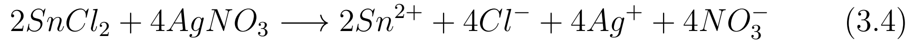

$$2SnCl_2 + 4AgNO_3 \longrightarrow 2Sn^{2+} + 4Cl^- + 4Ag^+ + 4NO_3^- \tag{3.4}$$

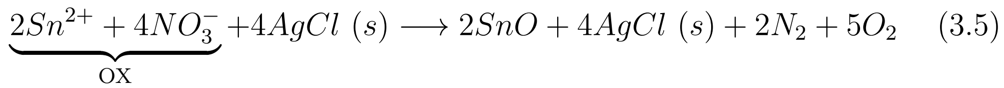

$$\underbrace{2Sn^{2+} + 4NO_3^-}_{\text{OX}} + 4AgCl\ (s) \longrightarrow 2SnO + 4AgCl\ (s) + 2N_2 + 5O_2 \tag{3.5}$$

So both Sn^{2+} and NO_3^+ act as oxidizer. Table 3.1 sums up all the valences used in this work.

Reagents	**Chemical Formula**	**Calculation**	**Total**
Oxidizing reagents (OV)	NH_4NO_3	$0 + (1 \cdot 4) + 0 + [3 \cdot (-2)]$	-2
	Sn^{2+} and NO_3^+	$2 + 0 + [3 \cdot (-2)]$	-4
Reducing reagent (RV)	$CO(NH_2)_2$	$4 - 2 + 2 \cdot (0 + 2 \cdot 1)$	$+6$

Table 3.1: Oxidizing and reducing valences of reagents.

Moreover, in order to prove the effectiveness of the SCS method, other solutions were prepared without combustion:

$$SnCl_2 \underset{2ME}{\longrightarrow} SnO_x + 6AgCl + 2HCl \quad (3.6)$$

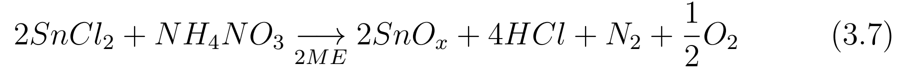

$$2SnCl_2 + NH_4NO_3 \underset{2ME}{\longrightarrow} 2SnO_x + 4HCl + N_2 + \frac{1}{2}O_2 \quad (3.7)$$

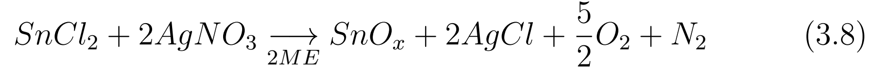

$$SnCl_2 + 2AgNO_3 \underset{2ME}{\longrightarrow} SnO_x + 2AgCl + \frac{5}{2}O_2 + N_2 \quad (3.8)$$

Finally, in order to have Ag-doped Tin oxide, solutions with, respectively, 0.1 $mmol$, 0.2 $mmol$ and 0.4 $mmol$ additional $AgNO_3$ were prepared. For all solutions with Silver, before the addition of fuel these were centrifuged for 4 min at 4000 rpm (Focus instruments, model F140) to remove $AgCl$ powder formed.

All precursor solutions were magnetically stirred at 430 rpm in air environment at room temperature for 1 h, to a volume of 10 mL and were filtrated through 0.20 μm hydrophilic filters[59][60].

Thermal and chemical characterizations of precursor solutions were performed by thermogravimetry, differential scanning calorimetry (TG-DSC) and pH test. TG-DSC analysis were performed under air atmosphere up to 540 $°C$ with a 5 $°C/min$ heating rate in an aluminum crucible with a punctured lid using a simultaneous thermal analyzer, Netzsch (TG-DSC - STA 449 F3 Jupiter).

In order to evaluate if deep ultraviolet (DUV) photochemical activation would have been useful, the absorbance (A) was measured from 190 to 800 nm. The optical properties were obtained using a Perkin Elmer lambda 950 UV/VIS/NIR.

3.2 Film deposition and characterization

Before deposition all substrates (silicon wafer, silicon-oxide wafer and glass with an area of 2.5×2.5 cm^2) were cleaned in an ultrasonic bath at $60°C$ in Acetone for 15 min, then in 2-Isopropanol for 15 min and dried under N_2; followed by a 15 min UV/Ozone surface activation step with a distance from the lamp of 5 cm, using a PSD-UV Novascan system.

Thin films were deposited by spin coating the SnO_x precursor solutions with a concentration of $0.1M$ for 35 s at 2000 rpm (Laurell Technologies)

followed by an immediate hot plate annealing at 300 $°C$, 250 $°C$ and 180 $°C$ for 30 min in ambient conditions or by combining a short-wavelength deep ultraviolet (DUV) photochemical activation with a lamp (NOVASCAN - PSD Pro Series + OES -1000D) at a distance of 9 cm with conventional thermal annealing at 150 $°C$ for 30 min in N_2 condition after each layer deposited. Figure 3.1 shows the samples deposited on glass, $p-Si$ and $p-Si/SiO_2$ after annealing at 300 $°C$.

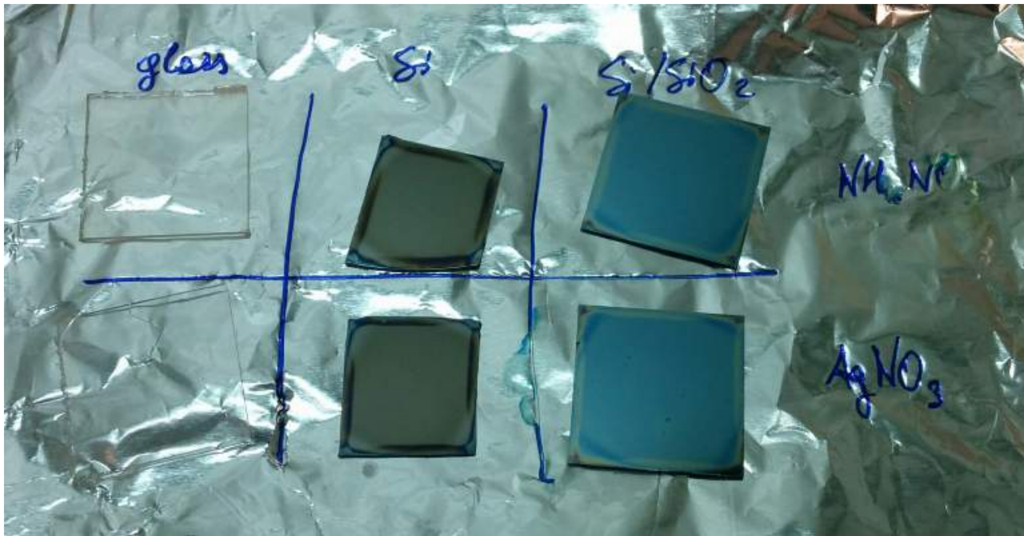

Figure 3.1: Samples deposited on glass, $p-Si$ and $p-Si/SiO_2$ respectively. In the first row there are the samples with NH_4NO_3 while in the second row there are the samples with $AgNO_3$.

Unlike sputtering or electron beam evaporation, spin coating is a non vacuum process and makes use of a very simple apparatus, which is reflected in fast processing times and low equipment costs. The process is typically initiated by dropping an excess amount of a liquid precursor on top of a substrate. The substrate is held in vacuum to a chuck, which is then rotated at high speed in order to spread the liquid precursor over the entire substrate, forming a thin film whose thickness is determined by the properties of the liquid precursor itself (viscosity, drying rate, surface tension, etc.) and also by deposition parameters such as rotation speed and acceleration[61]. After this process, the thin film still includes not only the desired chemical constituents but also some portion of the solvents included in the initial liquid

precursor. These solvents are removed by a dehydration process, normally consisting of heating the substrate in a hot plate. Higher film thickness or multilayer structures with different materials can be obtained by repeating the processes described above. Despite being a fast and low-cost process, spin coating has the disadvantage of generally requiring high annealing temperatures to attain thin films with reasonable electronic properties, and even when optimized, these properties are typically far from the ones obtained using vacuum deposition techniques. Figure 3.2 shows a schematic of the procedure.

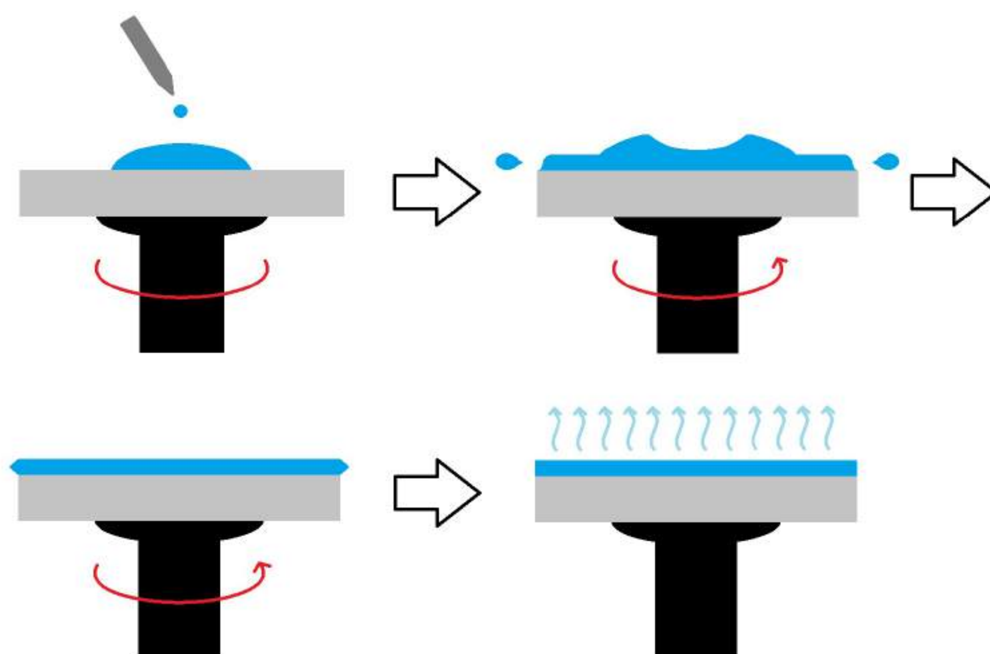

Figure 3.2: Scheme of spin coating deposition. An excess amount of a liquid precursor is dropped. The substrate is held by vacuum and an high speed rotation spread the liquid over the entire substrate. A final anneal remove the solvents that are left in the film.

Films were deposited in four layers. In order to study the thickness role, samples with different numbers of layers (one to eight) were also deposited. After deposition, properties of the films were analysed. Chemical characterization was performed by Fourier Transform Infra-Red (FTIR) spectroscopy, FTIR data were recorded using an Attenuated Total Reflectance (ATR) sam-

pling accessory (Smart iTR) equipped with a single bounce diamond crystal on a Thermo Nicolet 6700 Spectrometer. The spectra were acquired with a 45° incident angle in the range of $4500 - 525\ cm^{-1}$ and with a $2\ cm^{-1}$ resolution.

Films structure was assessed by grazing angle X-ray diffraction (GAXRD) performed by an X'Pert PRO PANalytical powder diffractometer using with $Cu\ K_\alpha$ line radiation ($\lambda = 1.540598\ \mathring{A}$) with angle of incidence of the X-ray beam fixed at 0.9°.

The surface morphology was investigated by Atomic Force Microscopy (AFM, Asylum MFP3D) and scanning electron microscopy (SEM, Zeiss Auriga Crossbeam electron microscope). The determination of the surface roughness (Rms) was acquired by AFM in alternate mode and the topographic images were analysed in data analysis software Gwyddion. Film thickness was measured by ellipsometry (Tobin-Yvon Horiba Uvisel ellipsometer) due to their small thickness, as shown in Figure 3.3.

Figure 3.3: Image of the ellipsometer used for thickness evaluation.

The model used is a model adapted from one used for film made by Zinc Tin Oxide (ZTO) and the samples were measured with both silicon substrate and silicon oxide substrate.

As for solutions, optical properties were obtained using a Perkin Elmer lambda 950 UV/VIS/NIR. The absorbance (A) and the transmittance (T)

was obtained from 190 to 2500 nm.

Both optical properties and thickness energy gap were measured using the Tauc plot, which has in the y-axis the value $(\alpha h\nu)^t$, where α is the absorption and t depends on the nature of the transition[62] and has $h\nu$ in the x-axis. Due to direct band gap of SnO_2 there is $\sqrt{\alpha h\nu}$ in the y-axis.

3.3 Device fabrication and characterization

The TFTs were produced in staggered bottom-gate structure. Source and drain aluminum electrodes (100 nm thick) were deposited by thermal evaporation via shadow mask under high vacuum onto annealed films, defining a channel width (W) and length (L). A 100 nm thick aluminum film was also deposited on the back of the silicon wafer to improve electrical contact as gate electrode. After deposition, a post-annealing at 160 $°C$ for 1 h in ambient conditions was performed. Figure 3.4 shows a sample after source and drain electrodes deposition.

Figure 3.4: Sample after source and drain electrodes deposition and after a post-annealing at 160 $°C$ for 1 h.

Transfer and output characteristics were measured in the dark, using semiconductor parameter analyzer (Agilent 4155C).

Contacts for TCOs were produced using Silver conductive paste dried for 1 h. Resistivity, mobility and carrier concentration were measured using the Hall measurement system (BIO-RAD / ACCENT HL 5500 PC).

In order to do this kind of measures, the van der Pauw technique was used. Samples were sized down to square $1x1$ cm^2 and ohmic contacts were deposited on the corners, as shown in Figure 3.5.

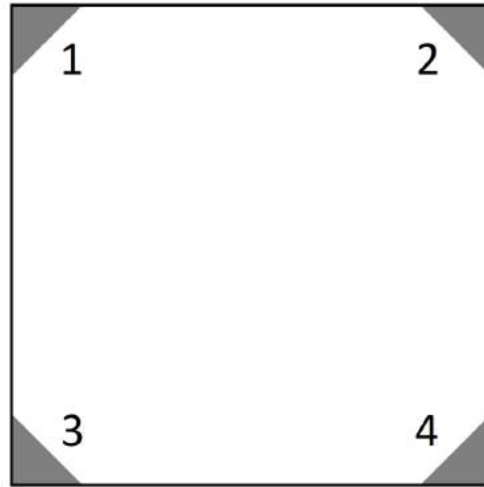

Figure 3.5: Van der Pauw pattern and contact positions used in this work.

The current source is applied to contacts 12 (I_{12}) and the voltage measured across 43 (V_{43}). The current source is next applied to contacts 14 (I_{14}) and voltage V_{23} is measured. The resistivity is given by:

$$\rho = \frac{\pi t}{2\ln(2)} \left[\frac{V_{43}}{I_{12}} + \frac{V_{23}}{I_{14}}\right] \cdot F \cdot Q \qquad [\Omega \cdot cm] \tag{3.9}$$

Where t is the thickness of the active layer, Q and F the symmetry and correction factors respectively, that the machine calculate by itself. Other permutations in the resistivity measurements are obtained by the rotation of the indices in equation 3.9. Sheet resistivity is given by:

$$\rho_s = \frac{\rho}{t} \qquad [\Omega \ / \ square] \tag{3.10}$$

Resistivity is measured with the same value of constant current I for all six permutations and the voltages V_{xy} are measured for both current directions and averaged in order to cancel thermoelectric and other effects.

For measuring the Hall effect in semiconductors, a constant current I is injected at two non-adjacent contacts and the difference in potential measured across the remaining two contacts, for a constant magnetic field B perpendicular to the sample surface. Balancing magnetic and electrostatic forces on a mobile charge, the vector equation results to be:

$$q = \vec{v} \cdot \vec{B} = q \cdot \vec{E} \qquad (3.11)$$

relating the electric field $\vec{E}$ to the magnetic field $\vec{B}$ and the carrier velocity $\vec{v}$. q is the elementary charge of an electron or hole. The current can be expressed as:

$$\vec{I} = q \cdot N \cdot t \cdot W \cdot \vec{v} \qquad (3.12)$$

where N is the carrier density and W the separation between the two contacts. The above equation assumes a constant carrier distribution and velocity through the layer, which is also assumed to be isotropic. In a real sample, the contacts arrangement is chosen such that the current I is perpendicular to the electric E and magnetic B field directions. The vector quantities can then be replaced with scalars and the last two equations lead to:

$$\frac{1}{q \cdot N} = \frac{V_h \cdot t}{I \cdot B} = R_H \qquad [m^3 \ / \ C] \qquad (3.13)$$

where V_h is the measured Hall voltage ($V_h = E \cdot W$) and R_H is the Hall coefficient. Moreover, the sheet Hall coefficient is defined as:

$$R_{Hs} = \frac{R_H}{t} = \frac{V_h}{I \cdot B} \qquad [m^2 \ / \ C] \qquad (3.14)$$

The sheet carrier density N_s is calculated from the measured sheet Hall coefficient R_{Hs}:

$$N_s = \frac{1}{q \cdot R_{Hs}} \qquad [cm^{-2}] \qquad (3.15)$$

If the thickness t is known then the bulk carrier density N is:

$$N = \frac{1}{q \cdot t \cdot R_{Hs}} \qquad [cm^{-3}] \tag{3.16}$$

The Hall mobility μ_H calculation does not depend on sample geometry but only on the measured values of sheet resistivity ρ_s and sheet Hall coefficient R_{Hs}. μ_H is given by:

$$\mu_H = \frac{R_{Hs}}{\rho_s} \tag{3.17}$$

Chapter 4

Experimental results

In this chapter, the experimental results regarding the solutions characterization, the thin film characterization and the final device characterization will be presented and discussed.

4.1 Solutions characterization

In order to investigate the behavior of the solutions under different temperatures, a thermal analysis was performed. Figure 4.1 shows the differential scanning calorimetry (DSC) and thermogravimetry (TG) results for the solution with Silver Nitrate ($AgNO_3$) with combustion.

In Figure 4.1 the solution presents a first endothermic peak at 132 $°C$, due to the organic components in the solution. Around 212 $°C$ there is the exothermic peak that is characteristic of the combustion process. At 335 $°C$ there is another endothermic peak, due to the degradation of the residual organics. Therefore, thermal analysis of the precursor solutions indicates that the minimum temperature required for full degradation is around 212 $°C$ for Silver Nitrate precursor solution with urea. For that, ultraviolet (UV) irradiation was used on the annealing process to reduce the temperature required because that aids on the degradation of residual organics. In order to assess if the solution absorbed UV irradiation, due to the deep UV lamp (which has a peak of intensity at 253.7 nm) in combination with the annealing of the films, the absorbance of the solution in that region was measured, showing high absorption from 190 nm to 400 nm. Moreover, the pH of the

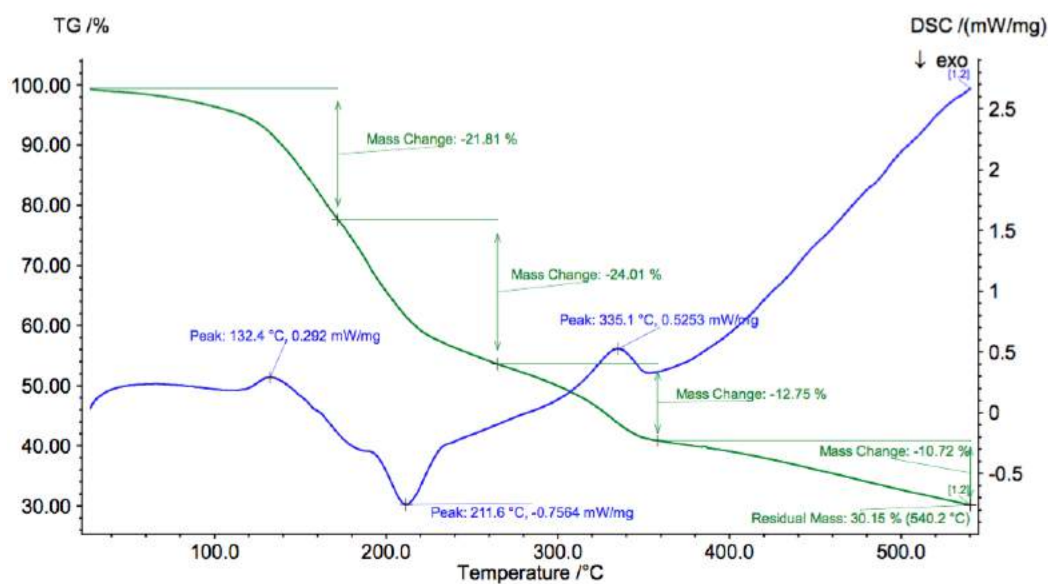

Figure 4.1: DSC-TG analysis for the solution with $SnCl_2$, $AgNO_3$, $Urea$ and $2-ME$ as solvent.

solution with $AgNO_3$ was tested with pH paper. Particularly, this was done to determine if any differences occur when the order of the reagents added to the solution changes. Table 4.1 shows the results obtained. As shown, there is no notable difference between the order followed during the solutions preparation.

Normal mode		Inverse mode	
Operation	pH	Operation	pH
+ 2-ME	6	+ 2-ME	6
+ $SnCl_2$	2	+ $AgNO_3$	5.5
+ $AgNO_3$	2	+ $SnCl_2$	2
Centrifuge	2	Centrifuge	2.5
+ Urea	3	+ Urea	4
After 2 h	2	After 2 h	2

Table 4.1: pH of solution with $AgNO_3$ by varying the reagents order.

4.2 Thin film characterization

4.2.1 Samples with stoichiometric precursors

As shown in the previous chapter, two different solutions were used in order to obtain Tin oxide: one using ammonium nitrate (NH_4NO_3) and one using Silver Nitrate ($AgNO_3$). The first samples deposited were with four layers and annealed at 180 $°C$, 250 $°C$ and 300 $°C$ for 30 min after each layer deposition. Moreover, in order to make a comparison with the normal sol-gel deposition technique (with no combustion) samples with no urea annealed at 350 $°C$ for 30 min after each deposition were also deposited. To prove that there are no organic residues in the films, a fourier transform infrared (FTIR) spectroscopy was performed, Figure 4.2, that shows the FTIR spectra for samples with and without annealing and samples with no combustion process.

There are no peaks over 1500 cm^{-1} that prove that there are no organic bounds. In the fingerprint region (from about 1500 to 500 cm^{-1}) a peak around 1100 cm^{-1}, something that is typical of metal bounds, is visible .

Since even the samples annealed at 180 $°C$ do not present organic residues in the films, other samples were produced with annealing temperature of 150 $°C$ under deep UV radiation for 30 min after the deposition of each layer. The samples deposited were the ones with $AgNO_3$ and the non combustion version with $AgNO_3$. First of all, in order to be sure that no organic residues

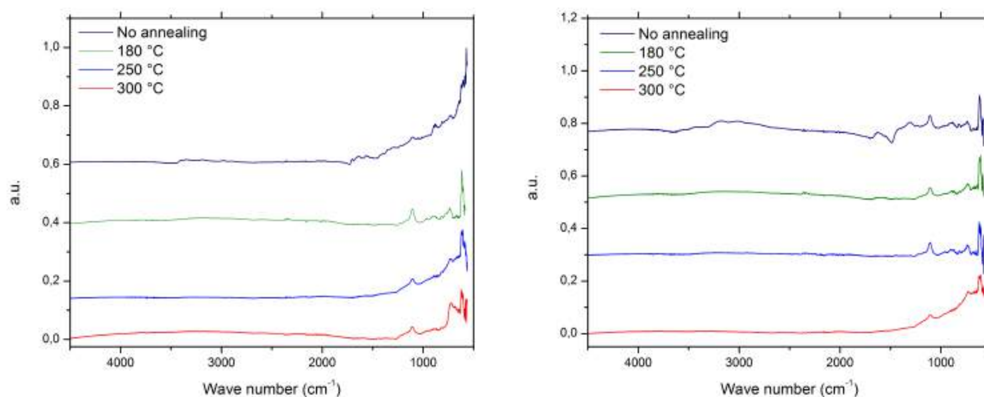

(a) Samples with $AgNO_3$.

(b) Samples with NH_4NO_3.

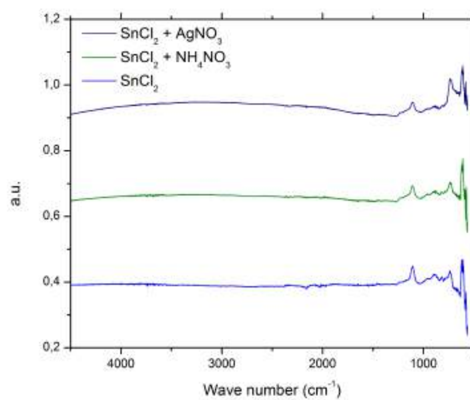

(c) Samples with no combustion at $350\ ^{\circ}C$.

Figure 4.2: The graphs show the FTIR spectra of the samples (a) with $AgNO_3$, (b) with NH_4NO_3 and (c) with no combustion process at $350\ ^{\circ}C$. There are no peaks over $1500\ cm^{-1}$ for the samples annealed that prove that there are no organic bounds. In the fingerprint region the peaks are located at the same wavenumbers for samples with the same precursors.

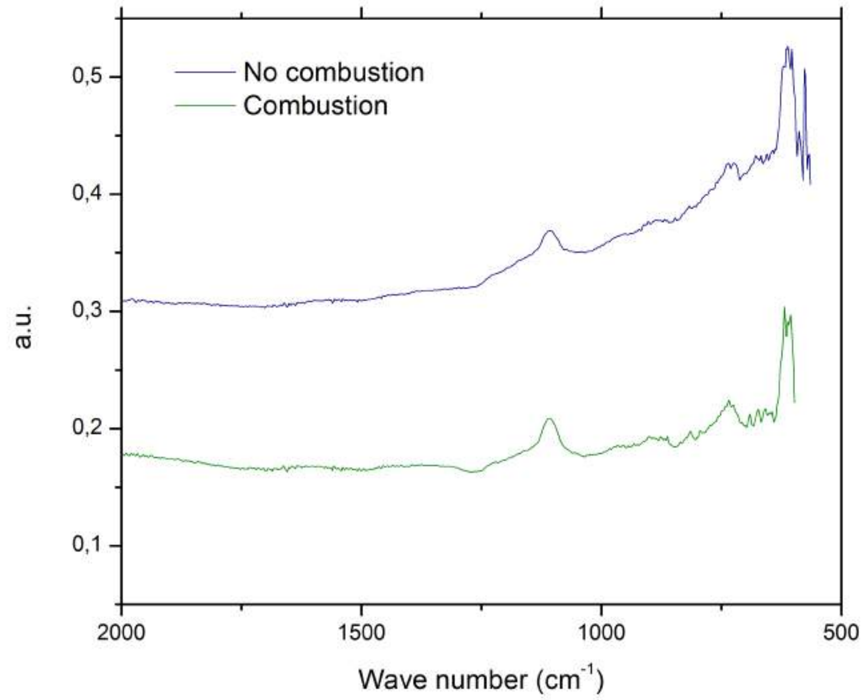

Figure 4.3: The graph shows the FTIR spectra of the samples annealed at $150\ ^{\circ}C$ and the deep UV radiation. There are no peaks over $1500\ cm^{-1}$ that prove that there are no organic bounds. In the fingerprint region the peaks are located at the same wavenumbers in both of the samples. Data are presented only until $2000\ cm^{-1}$ because there are no peaks between $2000\ cm^{-1}$ and $5000\ cm^{-1}$.

are left in the films, the FTIR measure was performed, as shown in Figure 4.3.

Another optical measure performed is the transmittance of the samples. The transmittance of Tin oxide thin films with different precursors was measured on glass between 190 nm and 2500 nm with wavelength steps of 2 nm. Looking at Figure 4.4, it is clear that transmittance is over 80% in the visible region for samples with $AgNO_3$ and samples with NH_4NO_3 but there are lower values for the sample with NH_4NO_3 annealed at 250 $^{\circ}C$ and for the sample annealed at 150 $^{\circ}C$ under DUV. For samples annealed at 300 $^{\circ}C$ the transmittance is over 80% for the thin films, regardless of the precursors.

The measure of the thickness of the samples was performed by ellipsom-

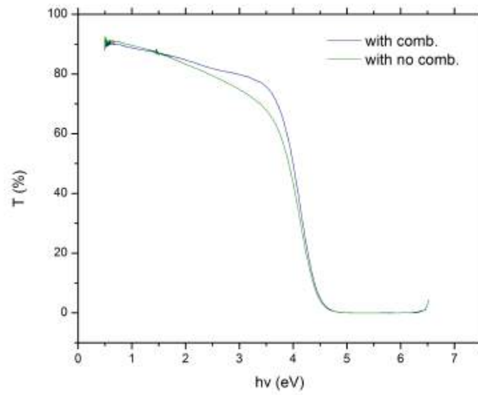

(a) Samples annealed at $150\ °C$ with DUV.

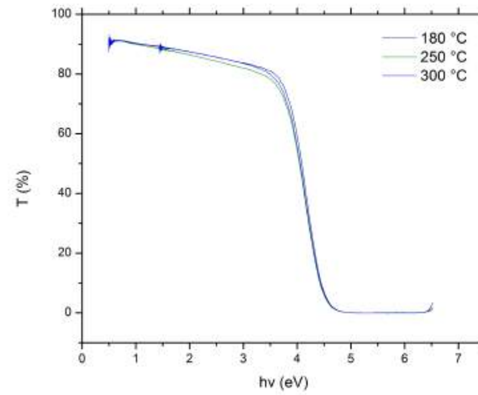

(b) Samples with $AgNO_3$.

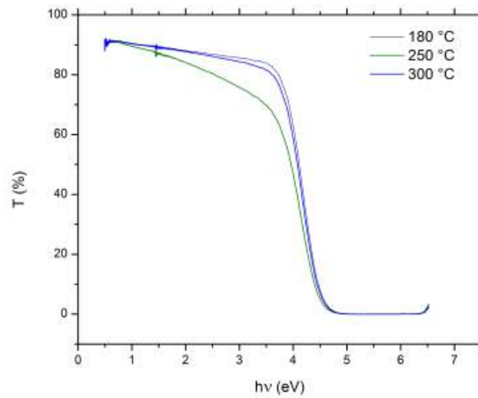

(c) Samples with NH_4NO_3.

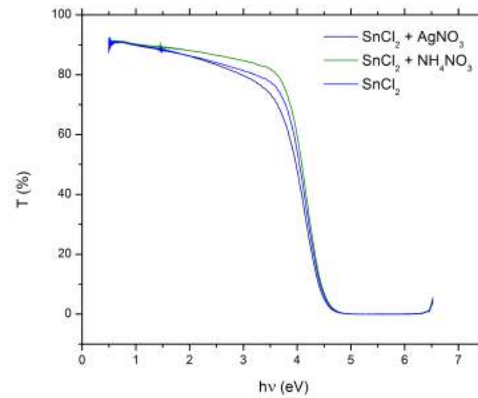

(d) Samples with no combustion at 350 °C.

Figure 4.4: The graphs show the transmittance of the samples (a) annealed at $150\ °C$ under DUV, (b) with $AgNO_3$, (c) with NH_4NO_3 and (d) with no combustion process at $350\ °C$. Is visible that all the samples have a transmittance of at least over 80% in the visible range, except for the sample annealed at $150\ °C$ under DUV with no combustion and the sample with NH_4NO_3 annealed at $250\ °C$.

etry. These measures were performed on samples deposited on $p-Si$ and $p-SiO_2$ substrates. Table 4.2 presents the values of the thickness evaluated on films deposited on $p-Si$ substrate. It is possible to see the influence of the temperature to the thickness, as show in Figure 4.5. The higher the temperature, the lower the thickness. Thanks to the measured values, the energy gap (E_G) of the samples was calculated using the Tauc plot. The results are also reported in Table 4.2.

Sample	**Thickness (nm)**	χ^2	E_G **(eV)**
with combustion at 150 $°C$	52.90	1.219	3.76 ± 0.03
with no combustion at 150 $°C$	45.90	0.380	3.72 ± 0.03
with $AgNO_3$ at 180 $°C$	51.71	0.462	3.81 ± 0.04
with $AgNO_3$ at 250 $°C$	45.20	1.999	3.80 ± 0.08
with $AgNO_3$ at 300 $°C$	34.13	5.463	3.80 ± 0.05
with NH_4NO_3 at 180 $°C$	68.15	0.329	3.82 ± 0.03
with NH_4NO_3 at 250 $°C$	46.92	0.424	3.76 ± 0.03
with NH_4NO_3 at 300 $°C$	36.03	0.515	3.80 ± 0.04
$SnCl_2 + AgNO_3$ at 350 $°C$	29.90	2.123	3.77 ± 0.02
$SnCl_2 + NH_4NO_3$ at 350 $°C$	27.32	0.822	3.82 ± 0.04
$SnCl_2$ at 350 $°C$	26.27	0.730	3.80 ± 0.07

Table 4.2: Thickness and energy gap of the samples. χ^2 is referred to the correlation between samples and the models used.

In order to analyze the structure of the devices an X-Ray diffraction (XRD) measure was performed for all the samples. The measures were performed on the films deposited on silicon substrate. In Figure 4.6 the role of the annealing temperature after the deposition of the films is visible. In fact, the absence of diffraction peaks in XRD diffractograms for samples annealed at 150 $°C$, 180 $°C$ and 250 $°C$ means that these samples are amorphous. On the other hand, the samples annealed at 300 $°C$ and 350 $°C$ show the typical structure of Tin dioxide (SnO_2).

As for the surface morphology, three kinds of investigation techniques

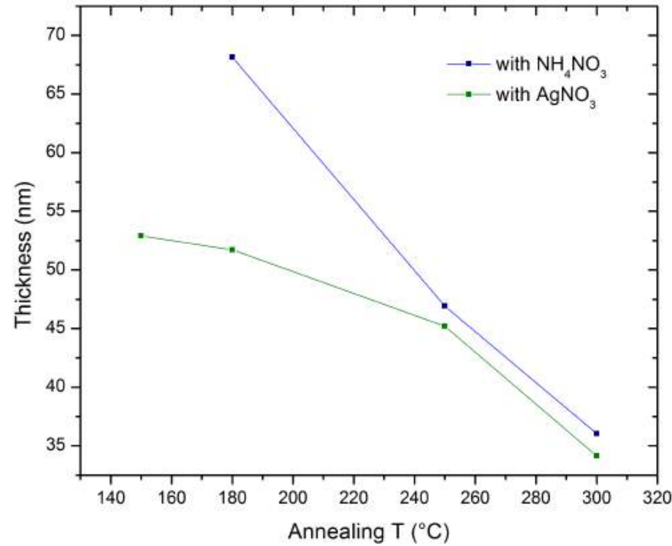

Figure 4.5: Thickness of the films depending on the annealing temperature. Thickness values are referred to samples deposited on $p - Si$ substrate.

were used: scanning electron microscope (SEM), energy dispersive X-Ray spectrometry (EDS) and atomic force microscope (AFM). These measurements were performed only on samples with $AgNO_3$ annealed at 150 $°C$ under DUV (Figure 4.7), at 180 $°C$ (Figure 4.8) and at 300 $°C$ (Figure 4.9). The determination of the surface roughness (Rms) was acquired by AFM in alternate mode and the topographic images were analysed with data analysis software Gwyddion. In Figure 4.9 some grains are visible, as we expected due to the crystalline nature noticed from the XRD measure while in Figure 4.8 some smaller structures are visible. The surface roughness is 0.211 nm for the sample annealed at 150 $°C$ under DUV, 2.32 nm for the sample annealed at 180 $°C$ and 0.711 nm for the sample annealed at 300 $°C$.

For the sample annealed at 300 $°C$ in Figure 4.10 the surface acquired by the SEM at two different magnifications is also reported. Here, two things are mainly visible: the crystalline structure of SnO_2 and some agglomerations. The same sample was also investigated with EDS analysis, reported in Figure 4.11, where is visible that the agglomerations are mainly composed by Silver, with a small quantity of Tin and Oxygen.

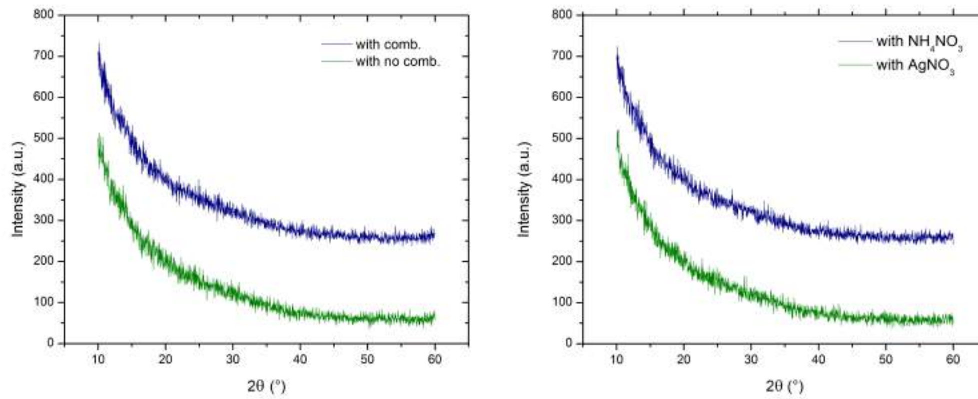

(a) Samples annealed at 150 $°C$ with DUV.

(b) Samples annealed at 180 $°C$.

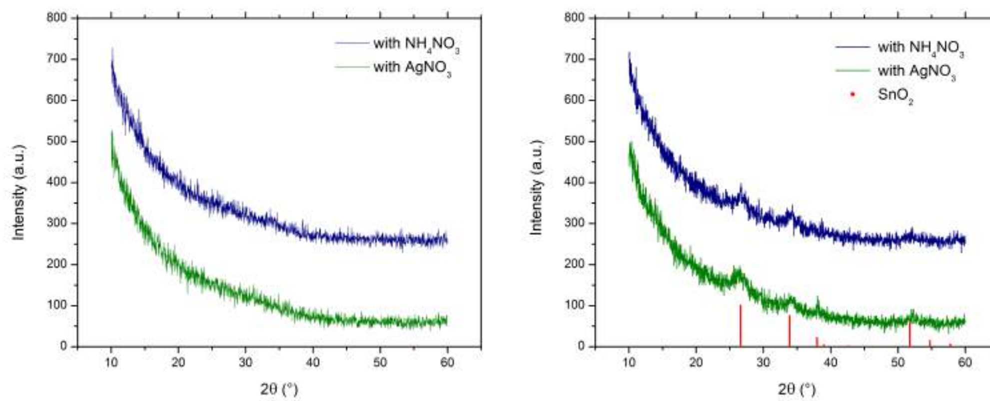

(c) Samples annealed at 250 $°C$.

(d) Samples annealed at 300 $°C$.

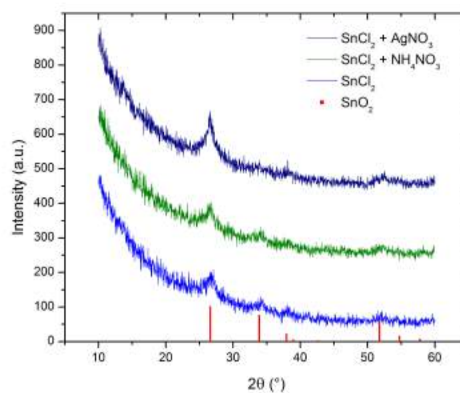

(e) Samples with no combustion annealed at 350 $°C$.

Figure 4.6: XRD diffractograms of samples annealed at (a) 150 $°C$ under DUV, (b) 180 $°C$, (c) 250 $°C$, (d) 300 $°C$ and (e) 350 $°C$ with no combustion process. Is visible how the structure of the thin films changes due to the annealing temperature. At 150 $°C$, 180 $°C$ and 250 $°C$ there is no crystalline structure while at 300 $°C$ and 350 $°C$ the samples have the characteristic peaks of the SnO_2.

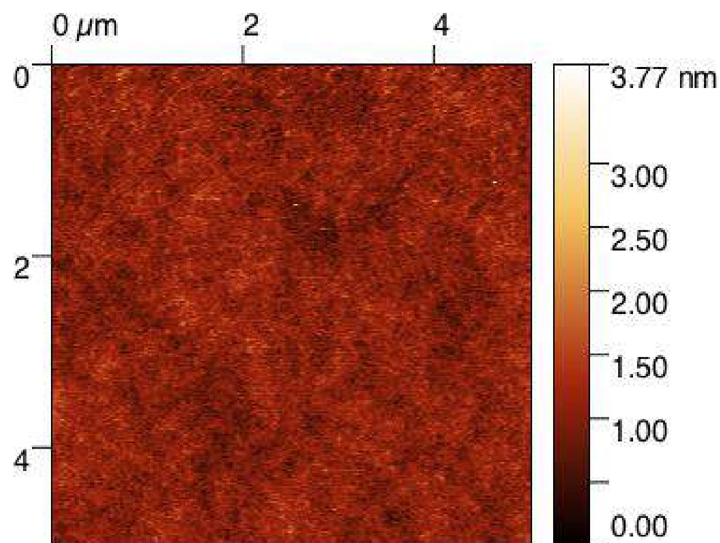

Figure 4.7: Topographic height map of sample with $AgNO_3$ annealed at $150\ ^{\circ}C$ under DUV acquired by AFM in alternate mode.

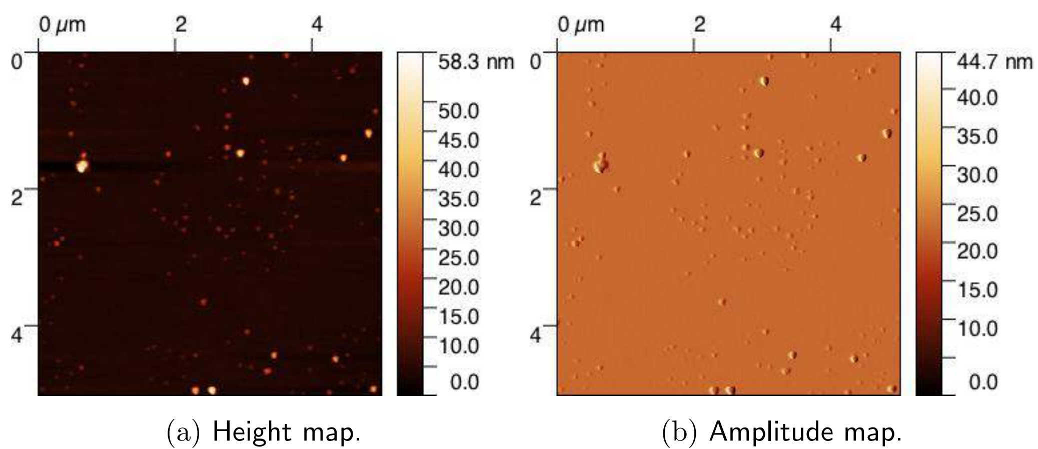

(a) Height map.

(b) Amplitude map.

Figure 4.8: Topographic maps of sample with $AgNO_3$ annealed at $180\ ^{\circ}C$ acquired by AFM in alternate mode.

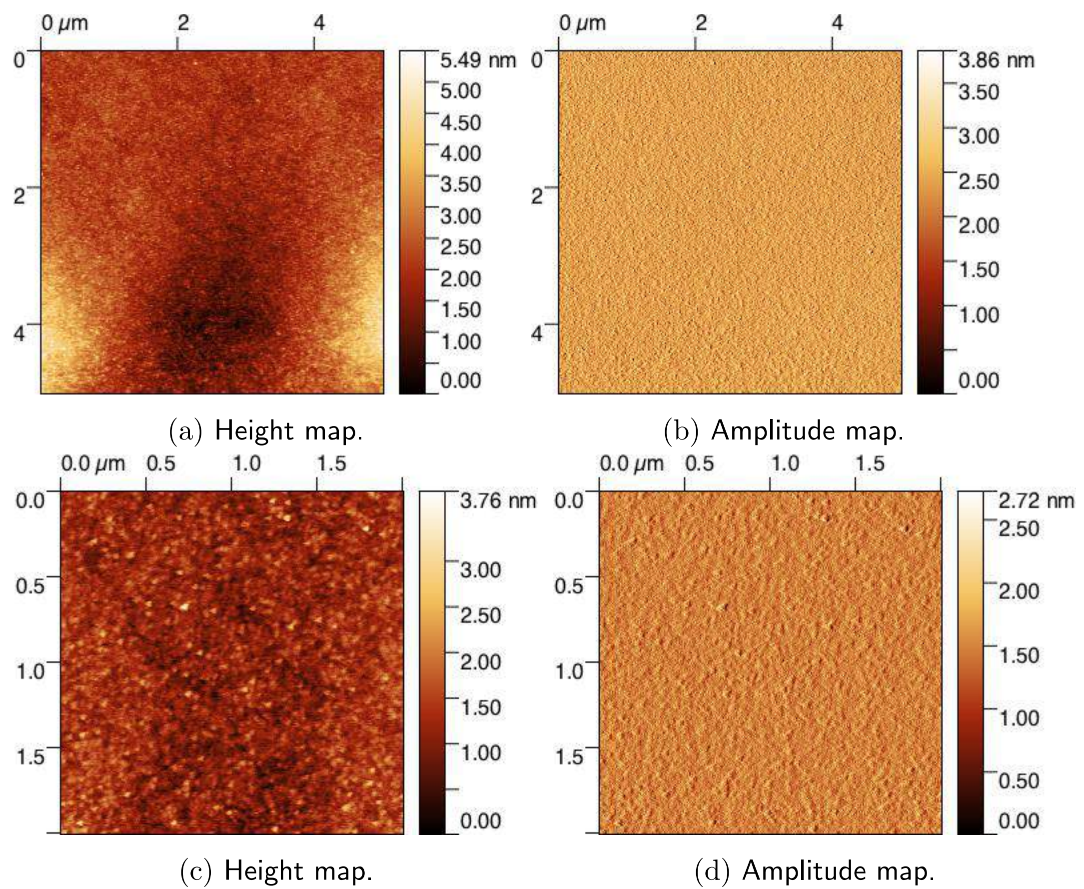

(a) Height map.

(b) Amplitude map.

(c) Height map.

(d) Amplitude map.

Figure 4.9: (a)(b) 5x5 μm and (c)(d) 2x2 μm topographic maps of sample with $AgNO_3$ annealed at $300\ ^{\circ}C$ acquired by AFM in alternate mode.

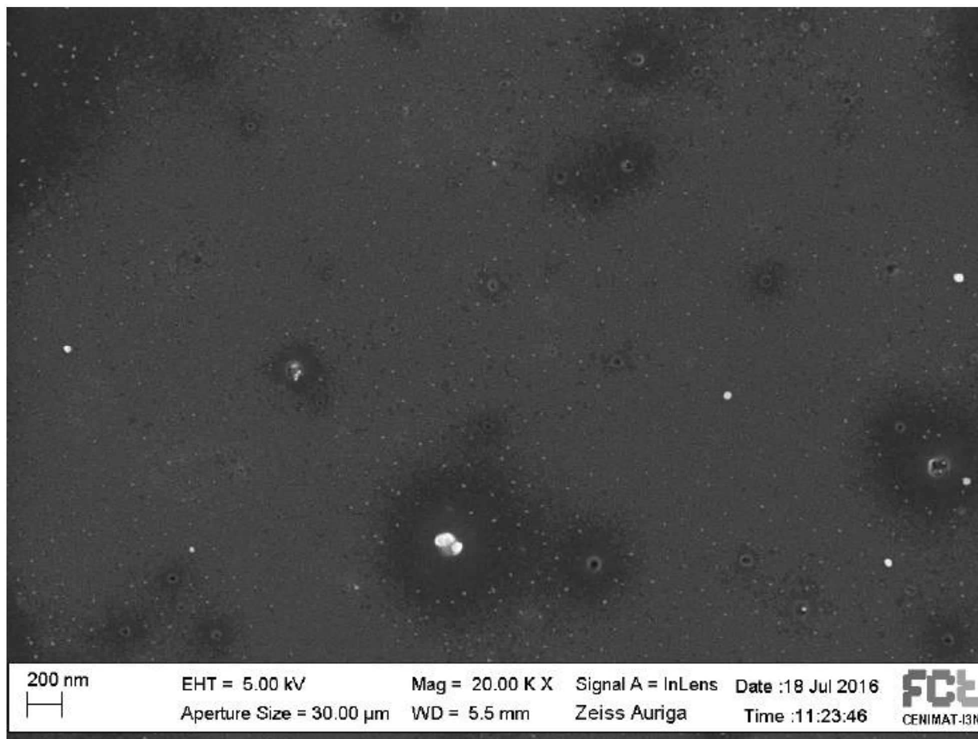

(a) 20k magnificaton.

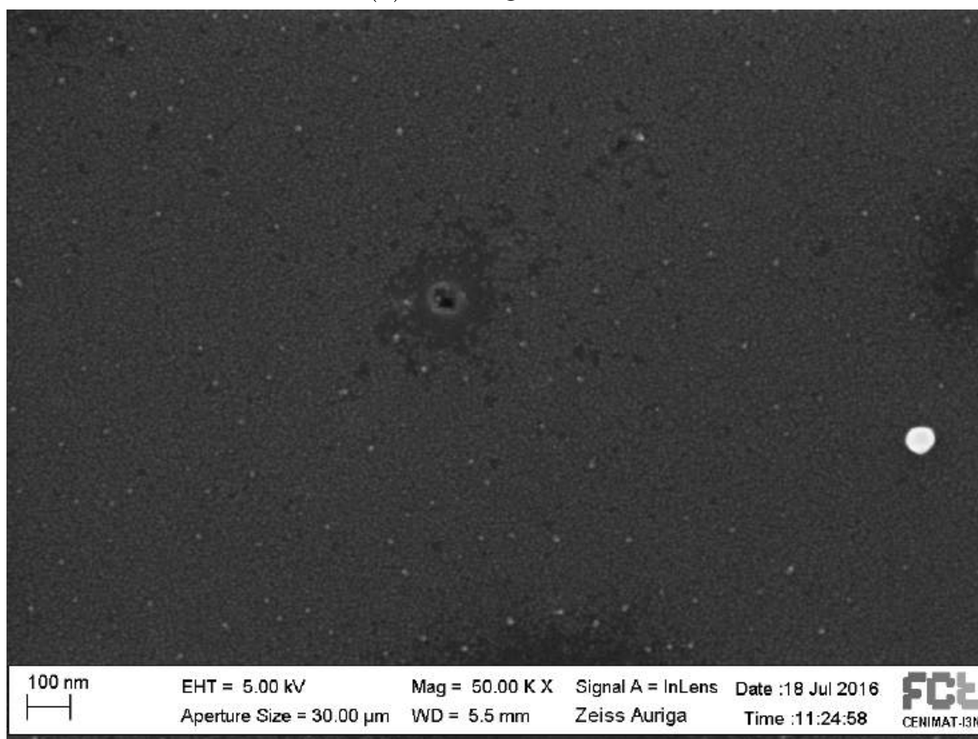

(b) 50k magnification.

Figure 4.10: SEM surface of the sample with $AgNO_3$ at two different magnification, (a) 20k and (b) 50k. Some agglomerations and the crystalline structure are visible.

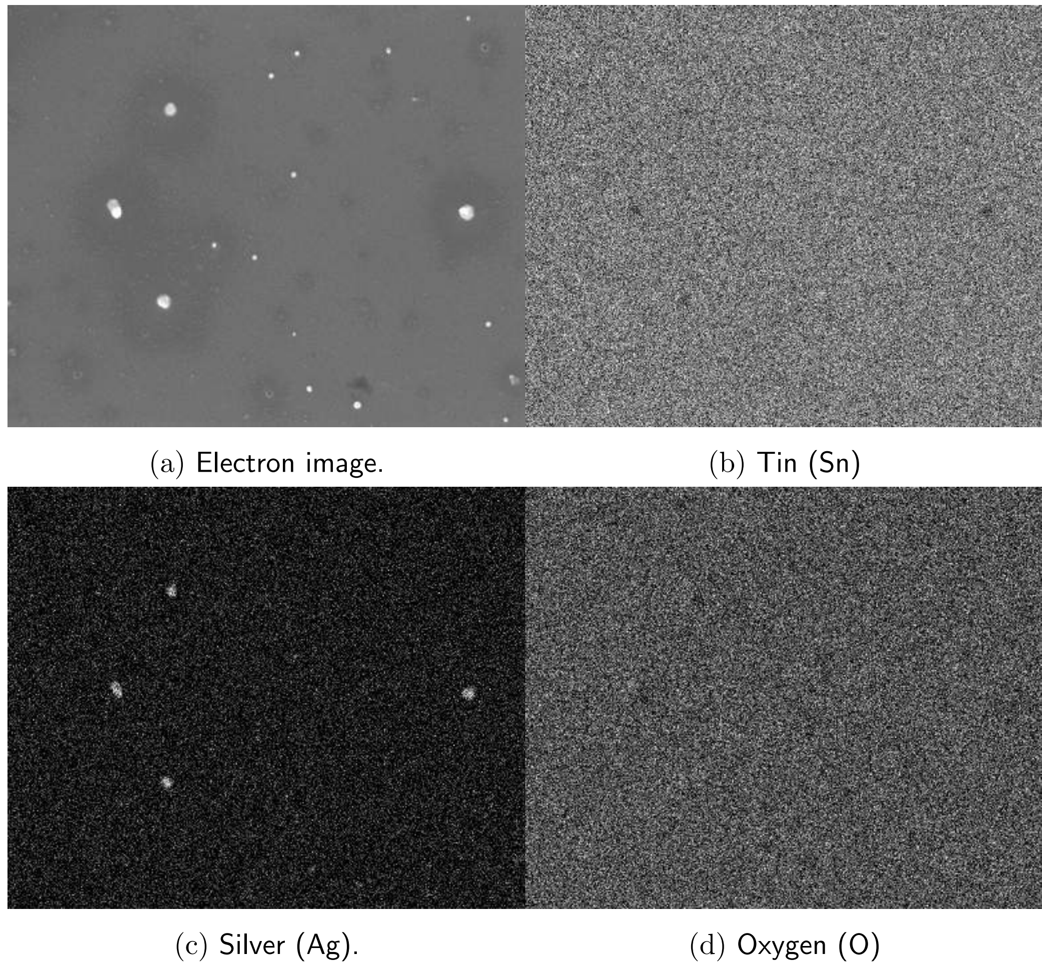

(a) Electron image. (b) Tin (Sn)

(c) Silver (Ag). (d) Oxygen (O)

Figure 4.11: Surface map of sample with $AgNO_3$ annealed at $300\ °C$ acquired by EDS. Here are reported the (a) electron map and the presence of (b) Tin, (c) Silver and (d) Oxygen. Is clearly visible that the agglomerations are mainly composed by Silver.

After contacts deposition, the electrical properties of the samples were analysed. Figure 4.12 shows the transfer characteristic of the samples considered until now. The width/length ratio (W/L) for all the devices is 14. Is clearly visible how none of the samples show the typical shape of a transfer curve but, instead, the films act as a conductive layers. For this reason, output characteristics are not reported in this work.

Samples that were annealed at 300 $°C$ show the best conductive property, therefore, resistivity, mobility and carrier concentration were measured using Hall measurement system for the sample with $AgNO_3$ annealed at 300 $°C$.

Resistivity		**Mobility**		**Carrier concentration**	
R_s (Ω/sq)	ρ $(\Omega \cdot cm)$	μ_H (m^2/C)	μ $(cm^2/V\ s)$	n_s/cm^2	n/cm^3
$1.16 \cdot 10^8$	$3.95 \cdot 10^2$	$-2.11 \cdot 10^5$	18.20	$-3.22 \cdot 10^9$	$-9.46 \cdot 10^{14}$

Table 4.3: Electrical properties measured using Hall measurement system for sample with $AgNO_3$ annealed at 300 $°C$.

The results are reported in Table 4.3, where R_s is the sheet resistance, ρ is the resistivity, μ_H is the Hall mobility, μ is the carrier mobility, n_s is the sheet carrier density and n is the bulk carrier density.

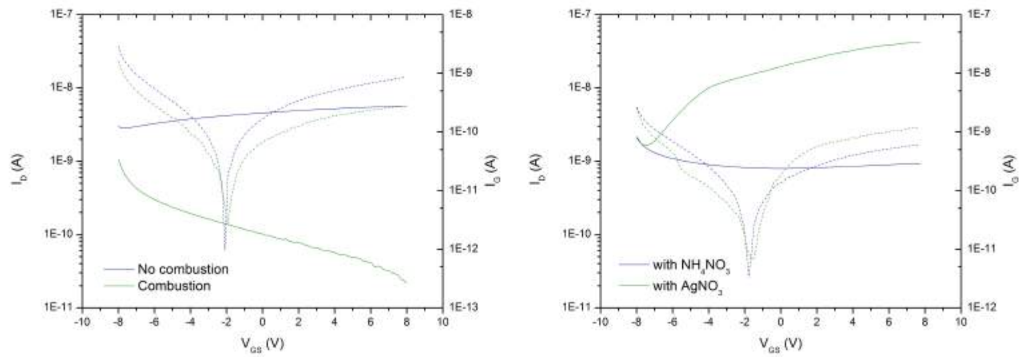

(a) Samples annealed at $150\ °C$ with DUV. (b) Samples annealed at $180\ °C$.

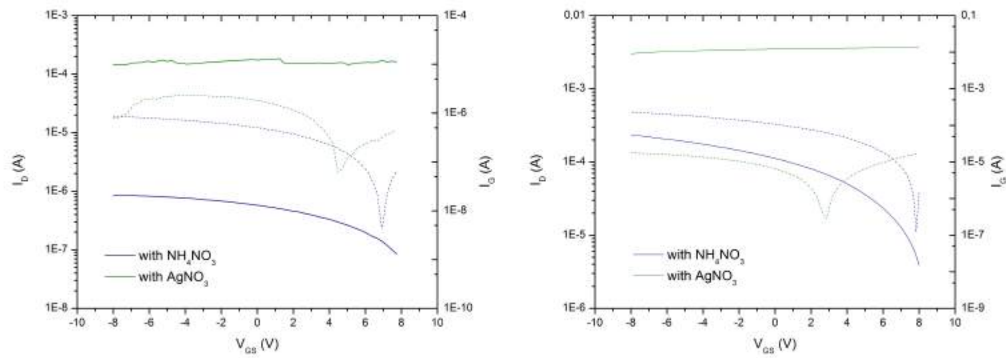

(c) Samples annealed at $250\ °C$. (d) Samples annealed at $300\ °C$.

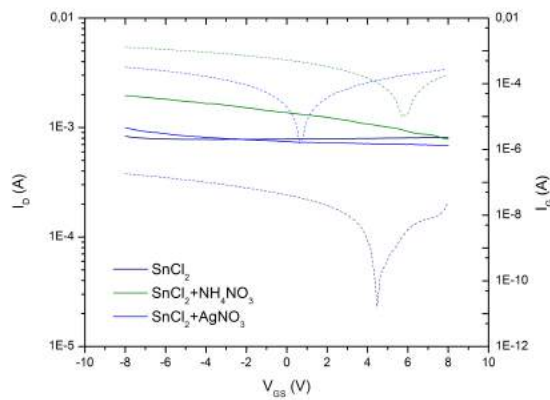

(e) Samples with no combustion annealed at $350\ °C$.

Figure 4.12: Transfer characteristic curves for the samples annealed at (a) $150\ °C$ under DUV, (b) $180\ °C$, (c) $250\ °C$, (d) $300\ °C$, (e) $350\ °C$. In the left y-axis the drain current (I_D) values are reported while in the right y-axis the gate leakage current (I_G) values are reported with dashed lines. All the measures were made with $V_D = 8\ V$ and V_{GS} that sweep from $-8\ V$ to $+8\ V$. The width/length ratio (W/L) is 14 for all the devices.

4.2.2 Different number of layers

In order to study the differences between films with different thickness, samples with 1, 2, 3, 6 and 8 layers were deposited. In particular, the samples prepared with the precursor with $AgNO_3$ were made with 1, 2, 3 and 6 layers annealed at 300 $°C$ for 30 min after each layer deposition and samples with 6 and 8 layers annealed at 300 $°C$ for 1 min after each layer deposition and for 30 min at the end. The samples prepared with the precursor with NH_4NO_3 were made with 1, 2 and 3 layers annealed at 300 $°C$ for 30 min after each layer deposition. The FTIR spectra of the samples are not reported in this work because it has already been shown that with annealing at 300 $°C$ there are no organic residues in the films.

As for other samples, the same measures were performed. XRD analyses are shown in Figure 4.13. It is important to note that only samples with 3 and 4 layer deposited show the SnO_2 structure, while the others are amorphous, even if they are annealed at 300 $°C$. The transmittance is over 80% in the visible region regardless of the number of layers.

Due to transmission and thickness measures, using the Tauc method, energy gaps were calculated and are reported in Table 4.4, the 4-layered samples that have already been considered are also reported. For the sample with 8 layers deposited with 1 min of annealing after each deposition the high value of χ^2 is visible, which means that the model used does not fit well with the sample. For this reason the value is not very reliable and as a result of this, its value of band gap is not reliable. It is possible to see the influence of the number of layers to the thickness, as shown in Figure 4.14. A sort of linear relation between the number of layers deposited and the thickness of the film is visible.

Considering the electrical properties, Figure 4.15 shows the transfer characteristics of the samples with different number of layers. The width/length ratio (W/L) for all the devices is 14. Is clearly visible how none of the samples show the typical shape of a transfer curve and that samples with 4 or 6 layers for samples with $AgNO_3$ as precursor and with 3 or 4 layers with NH_4NO_3 as precursor present the best conductive proprieties. Moreover, the two samples with only 1 min annealing show worse electrical properties, meanings that the annealing time was not enough to optimise the device. Even in this case is meaningless to report the output characteristics curves.

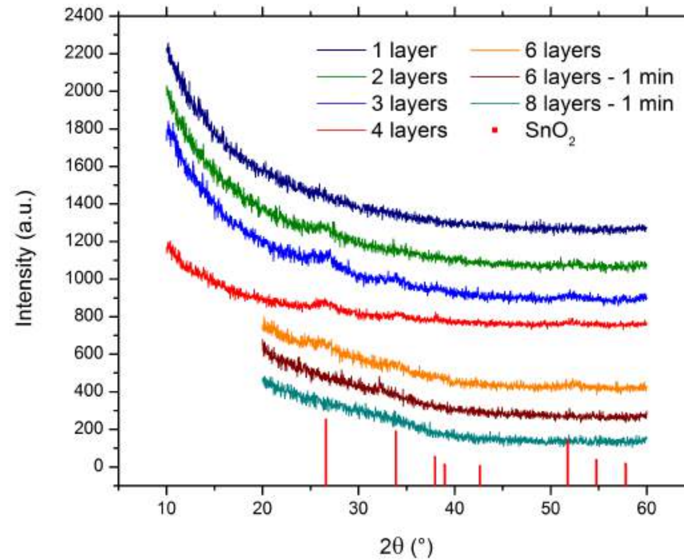

(a) Samples with $AgNO_3$.

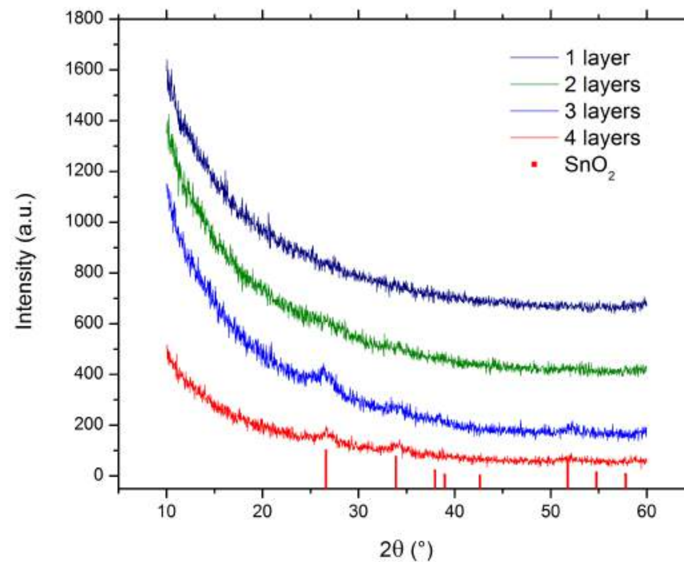

(b) Samples with NH_4NO_3.

Figure 4.13: XRD diffractograms of the samples with (a) $AgNO_3$, (b) NH_4NO_3 with different number of layers. Is visible how the structure of the thin films changes due to the number of layers. In both of the cases only the films with 3 and 4 layers show a crystal structure.

Sample		**Thickness (nm)**	χ^2	E_G **(eV)**
with NH_4NO_3	1 layer	11.66	0.073	3.79 ± 0.02
	2 layers	19.60	0.225	3.80 ± 0.03
	3 layers	24.51	0.539	3.78 ± 0.02
	4 layers	36.03	0.515	3.80 ± 0.05
with $AgNO_3$	1 layer	11.98	0.029	3.79 ± 0.03
	2 layers	18.79	0.232	3.81 ± 0.04
	3 layers	25.96	2.818	3.80 ± 0.05
	4 layers	34.13	5.463	3.80 ± 0.05
	6 layers, 30 *min* ann	62.85	3.647	3.79 ± 0.06
	6 layers, 1 *min* ann	69.80	3.087	3.81 ± 0.08
	8 layers, 1 *min* ann	201	260	3.83 ± 0.13

Table 4.4: Thickness and energy gap of the samples with different number of layers. Thickness values are referred to samples deposited on $p - Si$ substrate.

In conclusion, the sample with the best electrical properties is the one with 4 layers, already investigated in the section before. Adding or subtracting layers only results in getting worse properties.

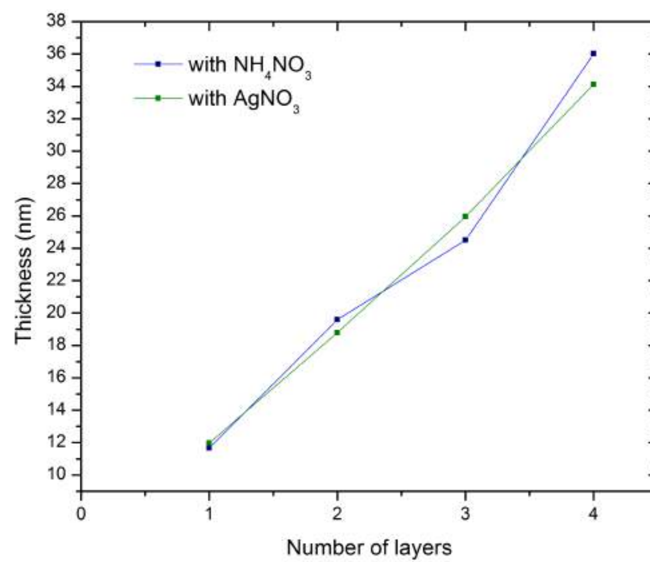

Figure 4.14: Thickness of the films depending on the number of layers. There is a linear-like relation between the number of layers of a film and its thickness.

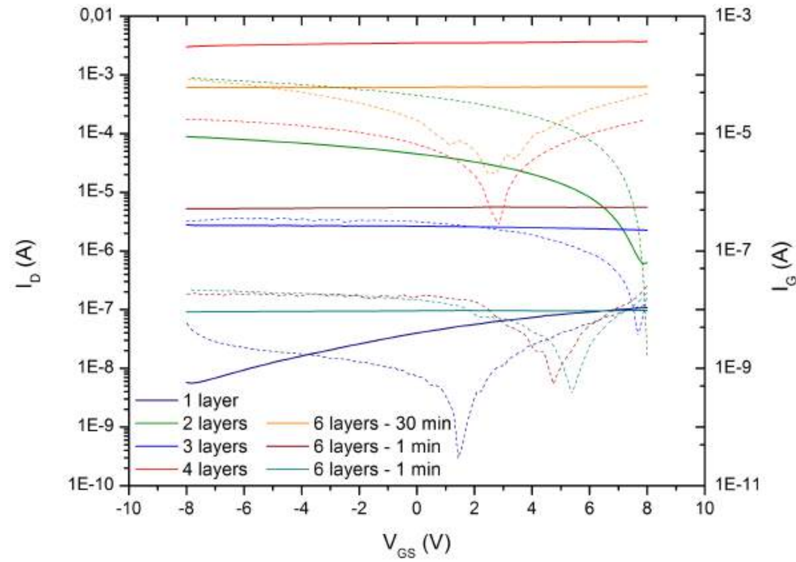

(a) Samples with $AgNO_3$.

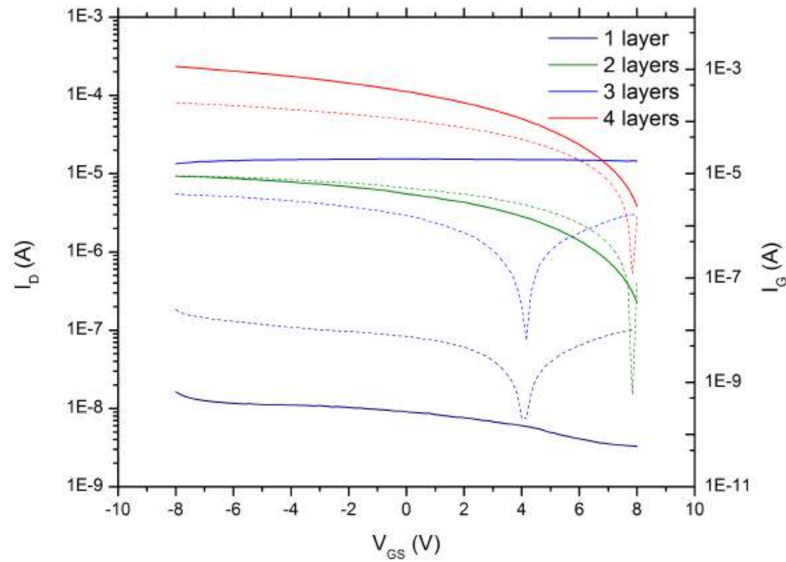

(b) Samples with NH_4NO_3.

Figure 4.15: Transfer characteristic curves for samples with different number of layers with (a) $AgNO_3$ and (b) NH_4NO_3 as precursor. In the left y-axis the drain current (I_D) values are reported while in the right y-axis the gate leakage current (I_G) values are reported with dashed lines. All the measures were made with $V_D = 8\ V$ and V_G that sweep from $-8\ V$ to $+8\ V$. The width/length ratio (W/L) is 14 for all the devices.

4.2.3 Using Silver as dopant

In the first chapter is reported that in literature Silver was being used as dopant in Tin oxide to produce SnO, promoting holes as majority carriers. In order to do that, extra Ag was added in the solution with $AgNO_3$. This way, the reaction is not stoichiometric anymore and there will be Ag, that does not react with Chlorine (forming $AgCl$ powder), in the solution deposited by spin coating.

In particular, solutions with extra 0.1, 0.2 and 0.4 $mmol$ of Ag were used, respectively. Samples with 4 layers annealed at 150 $°C$ under DUV, at 180 $°C$ and at 300 $°C$ for 30 min after each layer deposition were deposited.

For all samples the FTIR spectra were acquired (Figure 4.16) and none of them presents peaks over 1500 cm^{-1} that prove that there are no organic bounds. As other samples, in the fingerprint region a peak around 1100 cm^{-1} is visible, typical of metal bounds, but other peaks are not the same for all the films, as expected since the composition of samples is not the same.

The transmittance of samples in function of the energy of the light are reported in Figure 4.17 where a drop in transmittance around 2.5 eV is visible for some samples. This means that these samples are not fully transparent in the visible range. The quantity of Silver in the solutions and the amount of transmittance lost cannot be described by a linear relationship.

As for other samples, the measure of the thickness was performed by ellipsometry, using the same models. In Table 4.5 the values of the thickness are presented. Using transmittance and those values measured, the energy gap (E_G) of the samples was calculated and reported on the same table.

For some samples there are high values of χ^2 (above 10) which means that the model used doesn't fit well with the sample. For this reason the values are not really reliable and therefore, a relation between thickness and amount of Ag was not studied. For sample deposited on $p-SiO_2$ and annealed at 300 $°C$ the thickness was evaluated with cross section analysis by SEM and reported in Figure 4.18. The thickness obtained this way was used to calculate the energy gap values. In the images, the higher layer is the deposited contact, the layer below is the considered film and under it there are around 100 nm of $p - SiO_2$.

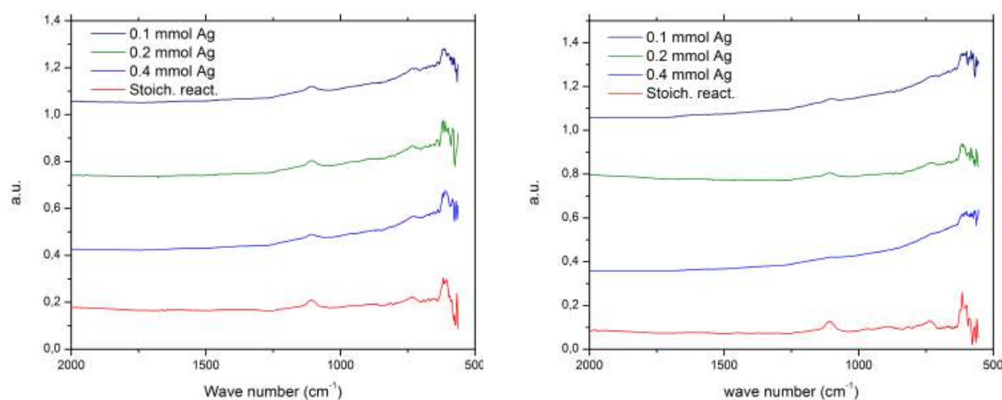

(a) Samples annealed at 150 $°C$ with DUV.

(b) Samples annealed at 180 $°C$.

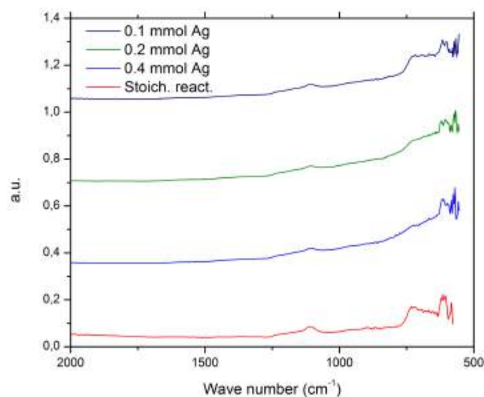

(c) Samples annealed at 300 $°C$.

Figure 4.16: The graphs show the FTIR spectra of the samples annealed at (a) 150 $°C$ under DUV, (b) 180 $°C$ and (c) 300 $°C$. There are no peaks over 1500 cm^{-1} for the samples that prove that there are no organic bounds. In the fingerprint region the peaks are not located at the same wavenumbers.

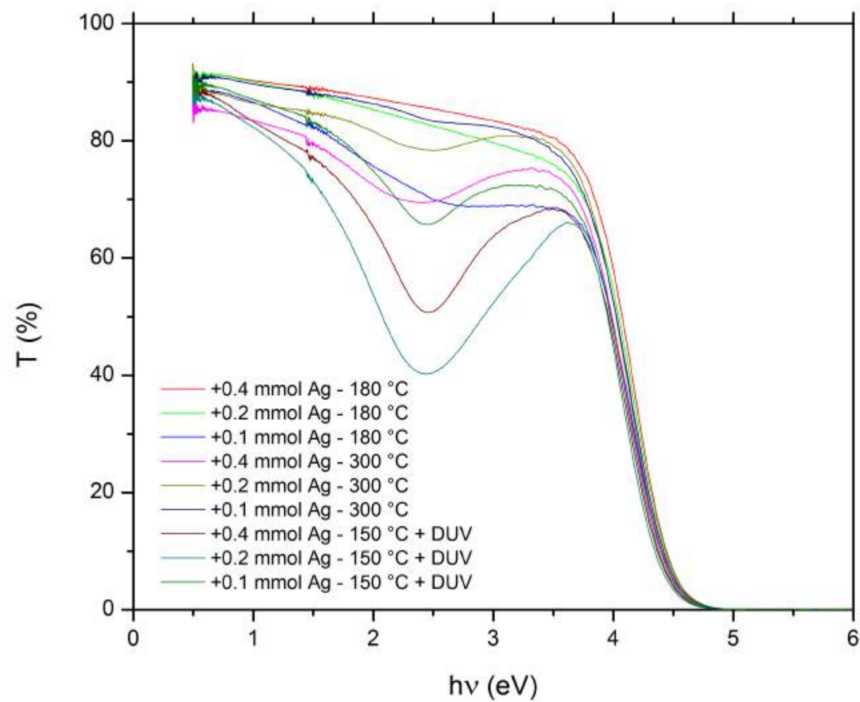

Figure 4.17: The graph shows the transmittance of samples doped with Ag, annealed at different temperatures. Most of the samples have a drop of transmittance around $2.5\ eV$, which makes them not fully transparent in the visible range.

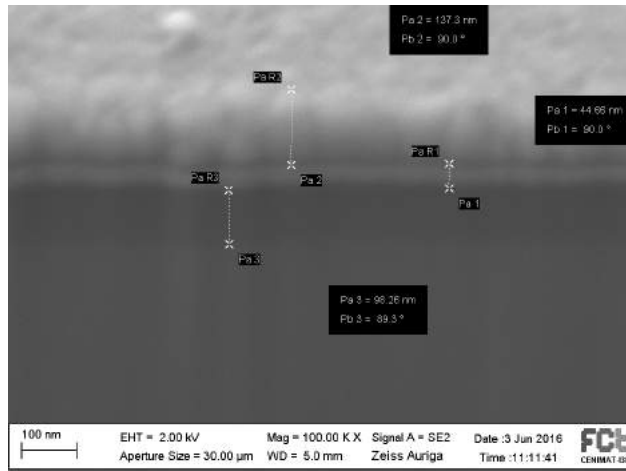

(a) Sample with + 0.1 $mmol\ Ag$.

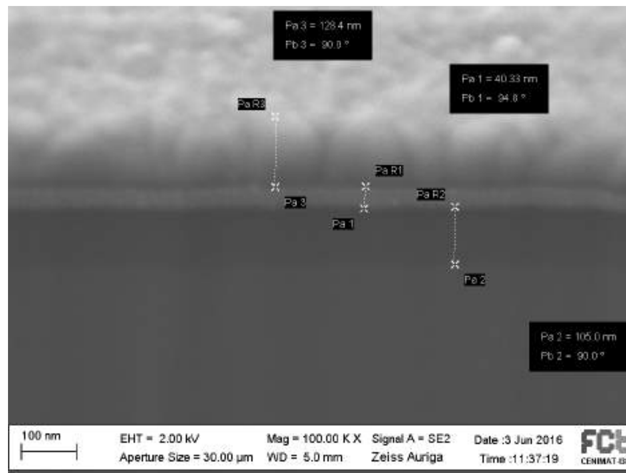

(b) Sample with + 0.2 $mmol\ Ag$.

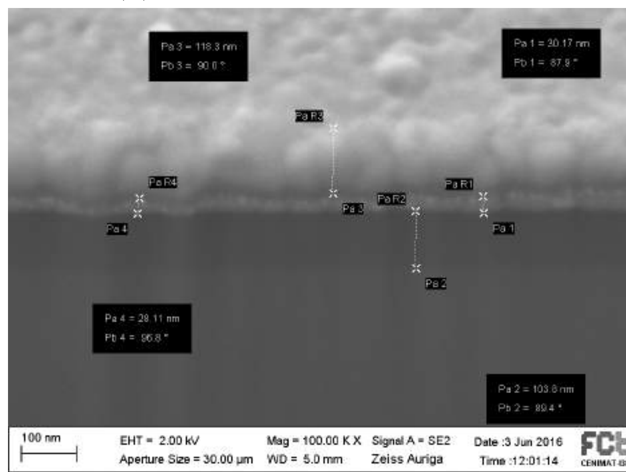

(c) Sample with + 0.4 $mmol\ Ag$.

Figure 4.18: Cross section of films annealed at 300 $°C$. The images report the thickness of the contacts deposited, of the film and of the $p - SiO_2$ substrate.

Sample		**Thickness (nm)**	χ^2	E_G **(eV)**
Annealed at 150 °C under UV	+0.1 $mmol\ Ag$	45.7	49	3.73 ± 0.04
	+0.2 $mmol\ Ag$	46.0	21	3.71 ± 0.07
	+0.4 $mmol\ Ag$	54.0	11	3.72 ± 0.03
Annealed at 180 °C	+0.1 $mmol\ Ag$	67.2	8.464	3.76 ± 0.04
	+0.2 $mmol\ Ag$	53.8	1.391	3.81 ± 0.04
	+0.4 $mmol\ Ag$	52.0	1.219	3.81 ± 0.03
Annealed at 300 °C	+0.1 $mmol\ Ag$	37.0	10	3.77 ± 0.06
	+0.2 $mmol\ Ag$	38.7	15	3.75 ± 0.04
	+0.4 $mmol\ Ag$	48.0	3.436	3.80 ± 0.11

Table 4.5: Thickness and energy gap of the samples doped with Ag. Thickness values are referred to samples deposited on $p - Si$ substrate.

The films structures, analysed by XRD, are reported in Figure 4.19. Samples annealed at 180 °C are amorphous as expected while samples annealed at 150 °C under DUV present a peak typical of Silver in heavily doped samples. The main differences compared to the films deposited with stoichiometric reactions are in samples annealed at 300 °C. Here, many high peaks due to Silver and to Silver Chloride are visible while the ones due to SnO_2 disappeared.

In order to better understand things in these doped samples, surface morphology investigation techniques were used, in particular SEM, EDS and AFM analysis were performed. Figure 4.20 and Figure 4.21 show the topographic images acquired with AFM. For the most interesting samples the amplitude images are also showed. The surface roughness is reported in Table 4.6.

In particular, agglomeration structures are visible in films doped with 0.1 $mmol$ of Ag for both 180 °C and 300 °C annealing temperatures. Further information were acquired by SEM and EDS investigations, in Figure 4.22, Figure 4.23, Figure 4.24, Figure 4.25, Figure 4.26, Figure 4.27, Figure 4.28 and Figure 4.29 the surface images acquired using SEM investigations are reported.

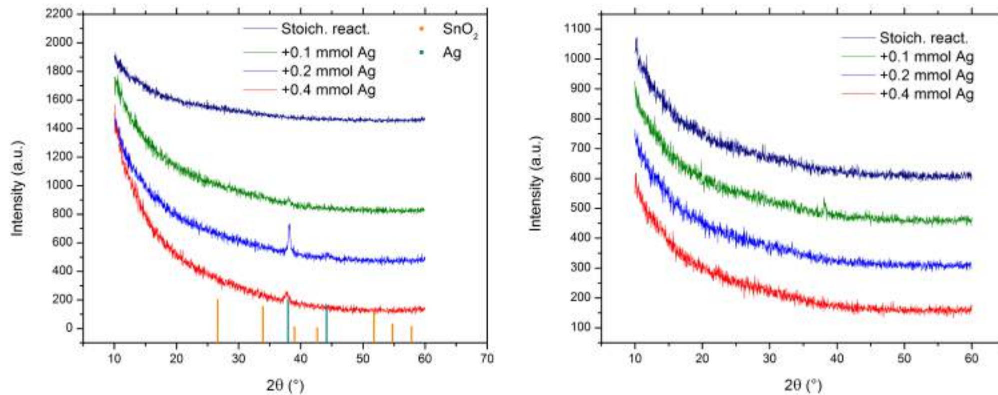

(a) Samples annealed at $150\ °C$ with DUV. (b) Samples annealed at $180\ °C$.

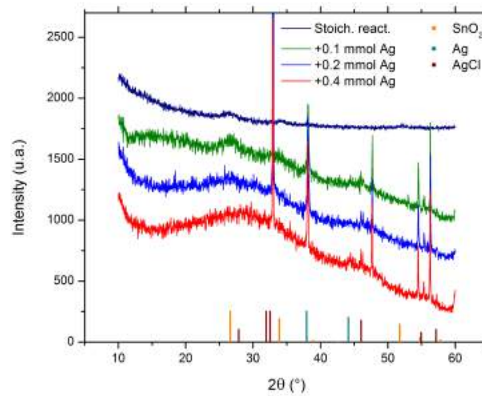

(c) Samples annealed at $300\ °C$.

Figure 4.19: XRD diffractograms of samples deposited with stoichiometric reactions and doped with Ag annealed at (a) $150\ °C$ under DUV, (b) at $180\ °C$ and (c) at $300\ °C$. Is visible how the structure of the thin films changes due to the annealing temperature. At $150\ °C$ and $180\ °C$ there is no crystalline structure except for a peak due to Ag in samples heavily doped while at $300\ °C$ the samples have the characteristic peaks of Ag and $AgCl$.

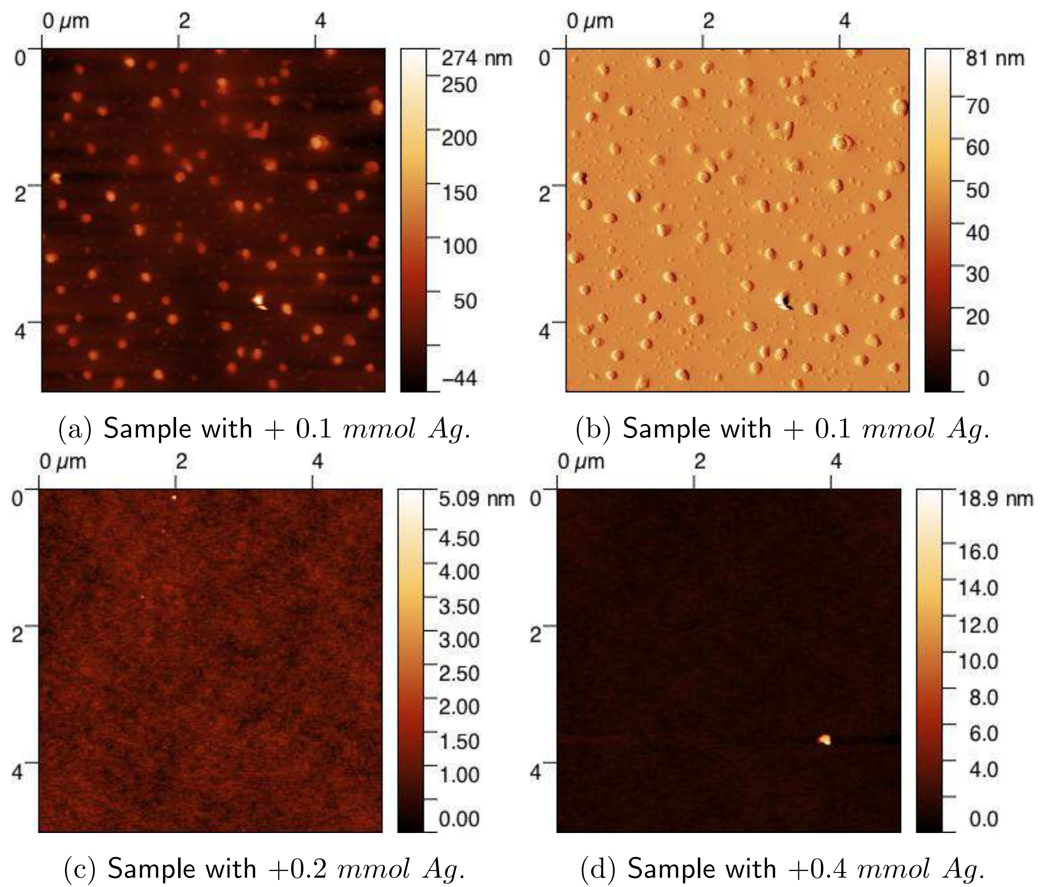

(a) Sample with + $0.1\ mmol\ Ag$.

(b) Sample with + $0.1\ mmol\ Ag$.

(c) Sample with $+0.2\ mmol\ Ag$.

(d) Sample with $+0.4\ mmol\ Ag$.

Figure 4.20: Height (a, c, d) and amplitude (b) map of samples doped with Ag annealed at $180\ ^{\circ}C$ acquired by AFM in alternate mode.

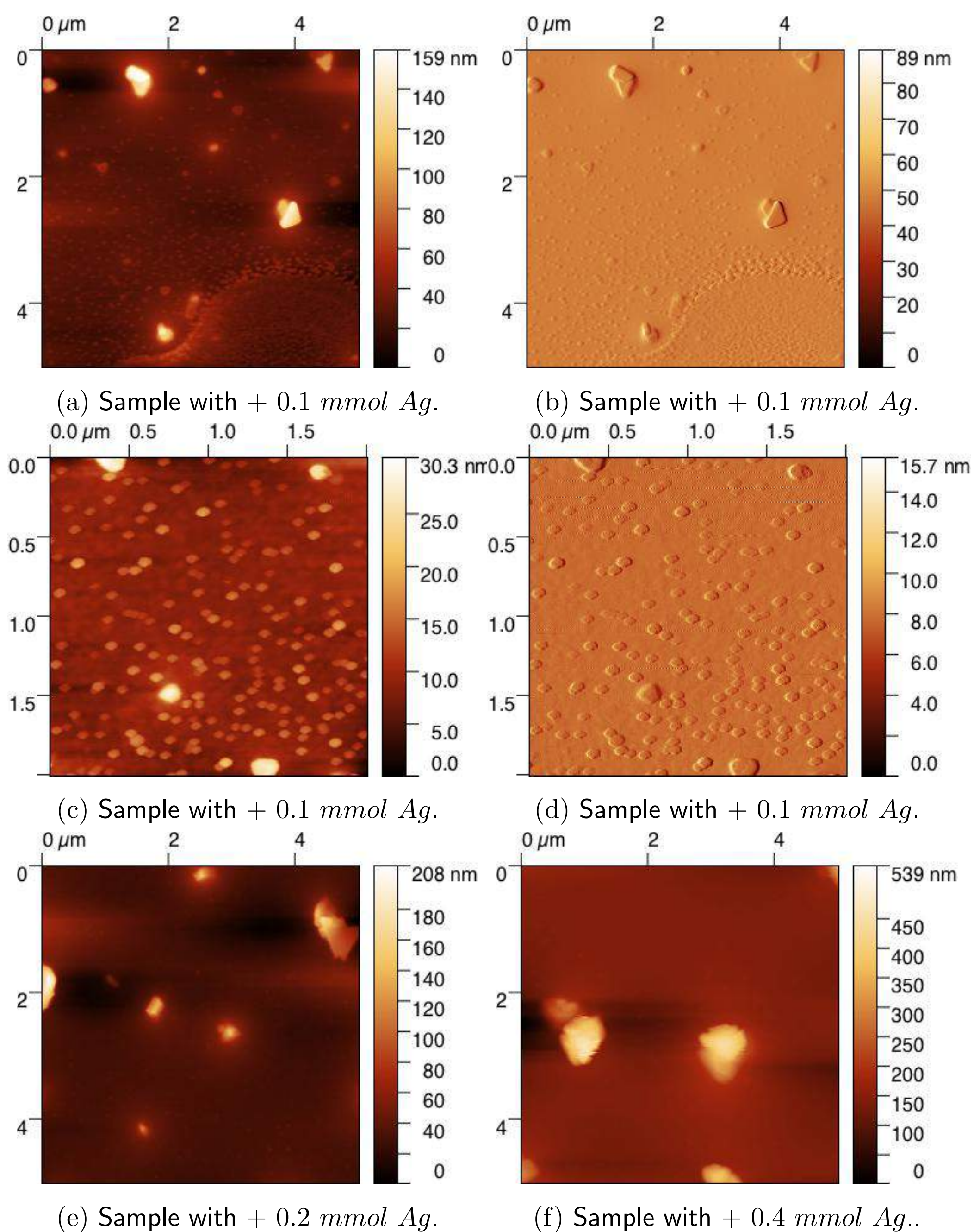

(a) Sample with + 0.1 $mmol$ Ag.

(b) Sample with + 0.1 $mmol$ Ag.

(c) Sample with + 0.1 $mmol$ Ag.

(d) Sample with + 0.1 $mmol$ Ag.

(e) Sample with + 0.2 $mmol$ Ag.

(f) Sample with + 0.4 $mmol$ Ag..

Figure 4.21: Height (a, c, e, f) and amplitude (b, d) map of samples doped with Ag annealed at 300 $°C$ acquired by AFM in alternate mode.

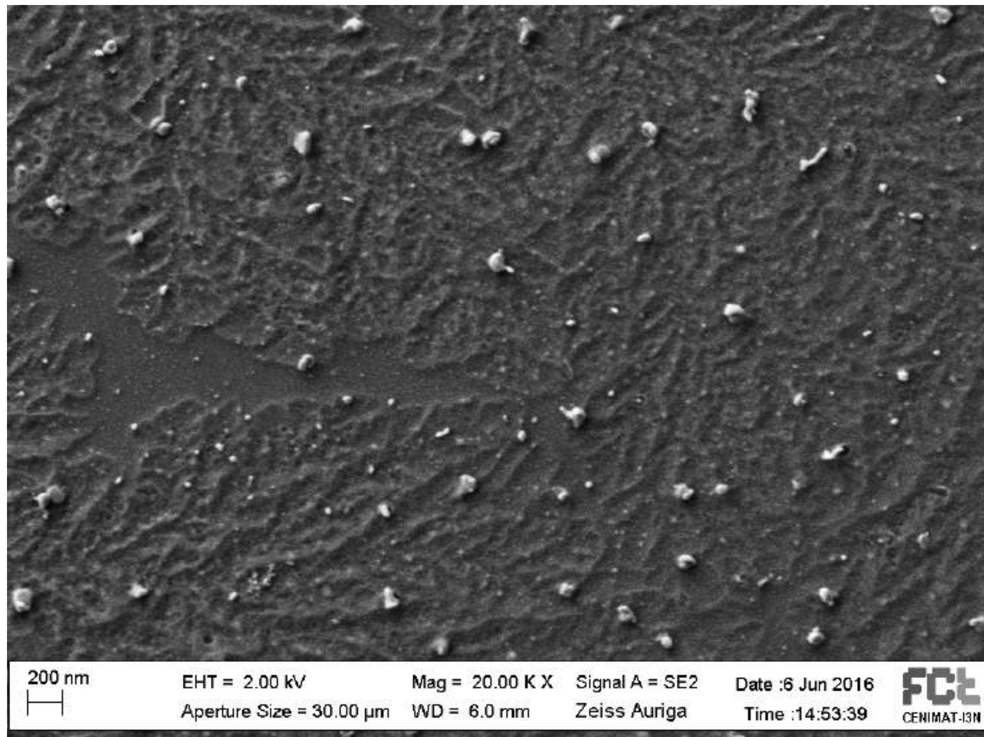

(a) 20k magnificaton.

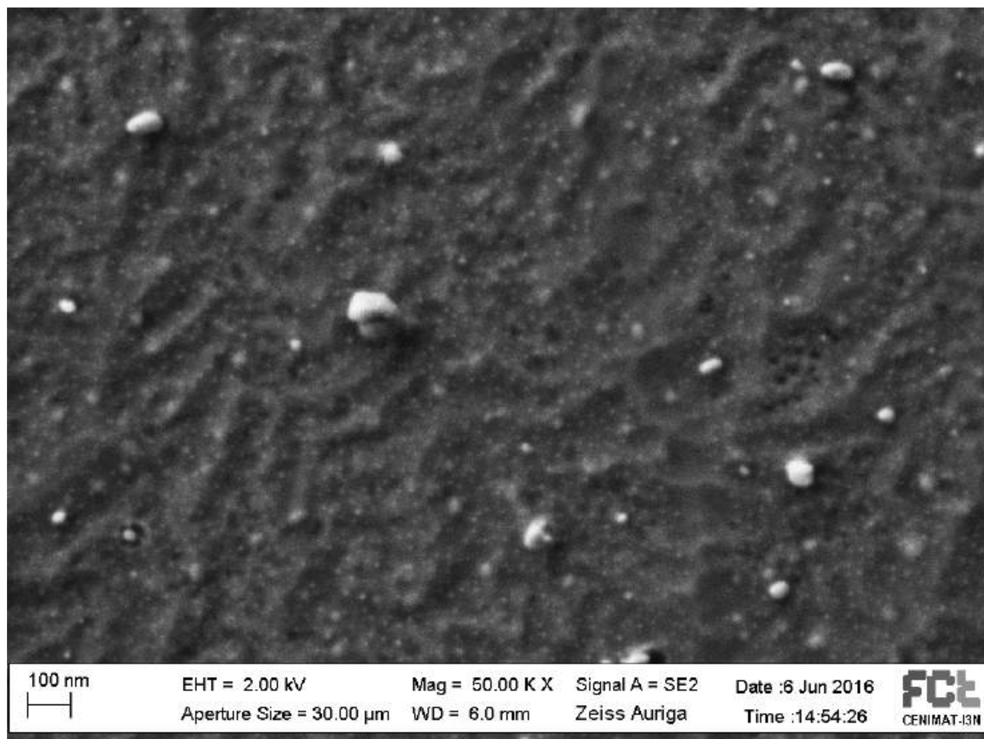

(b) 50k magnification.

Figure 4.22: SEM surface of the sample doped with 0.1 $mmol$ of Ag annealed at 150 $°C$ under DUV at two different magnifications, (a) 20k and (b) 50k. Agglomerations are visible.

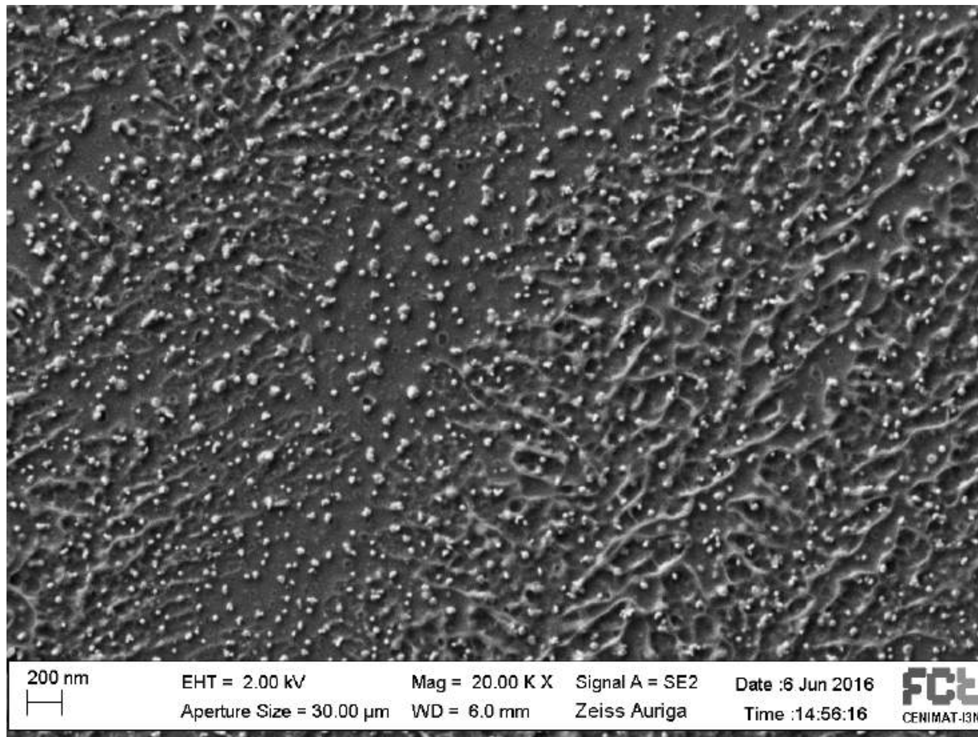

(a) 20k magnificaton.

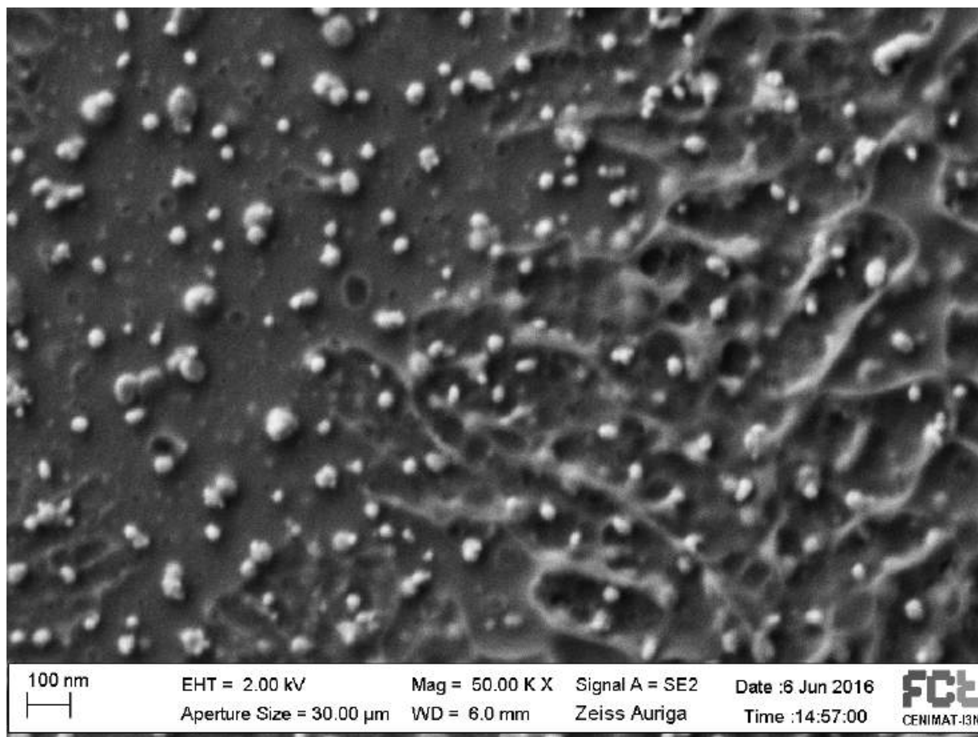

(b) 50k magnification.

Figure 4.23: SEM surface of the sample doped with $0.2\ mmol$ of Ag annealed at $150\ °C$ under DUV at two different magnifications, (a) 20k and (b) 50k. Agglomerations are visible.

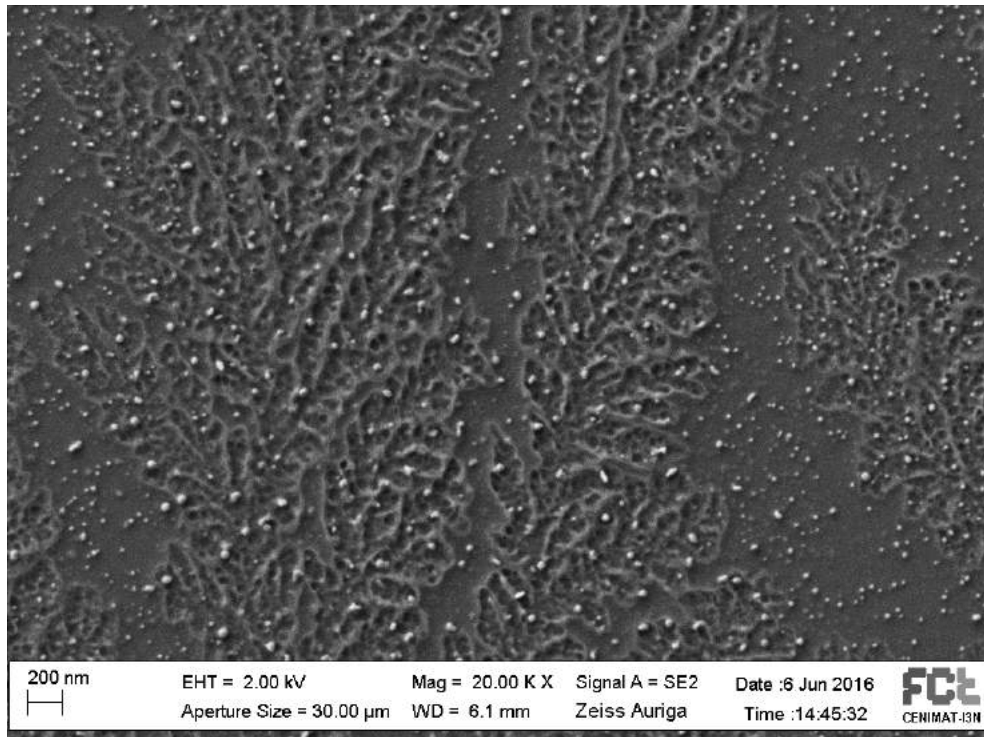

(a) 20k magnificaton.

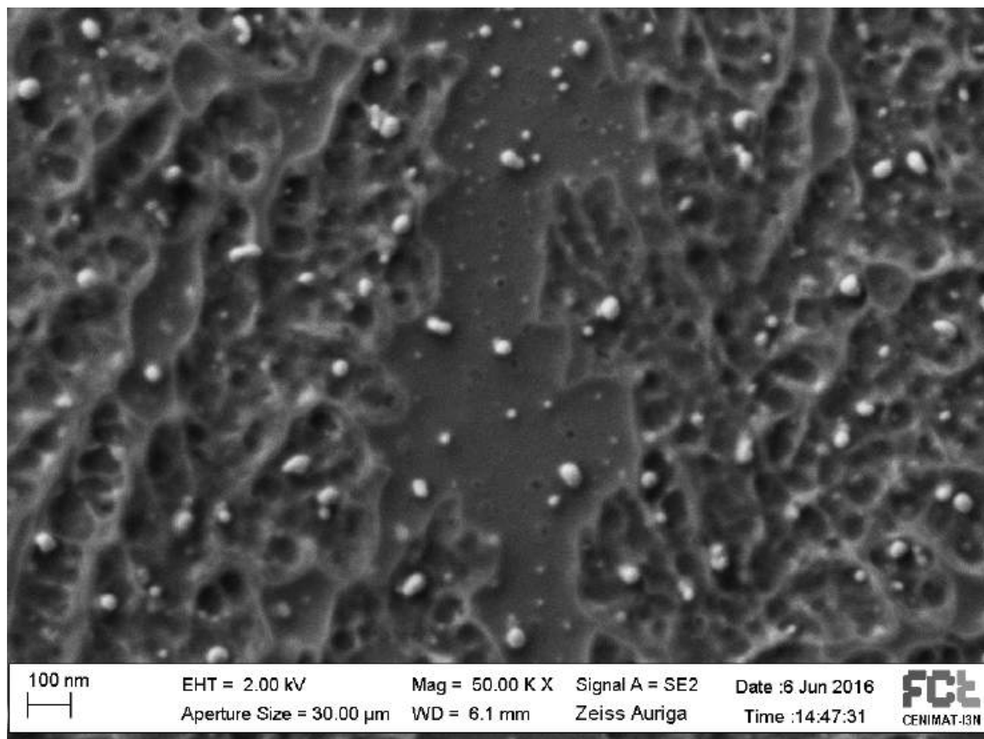

(b) 50k magnification.

Figure 4.24: SEM surface of the sample doped with $0.4\ mmol$ of Ag annealed at $150\ °C$ under DUV at two different magnifications, (a) 20k and (b) 50k. Agglomerations are visible.

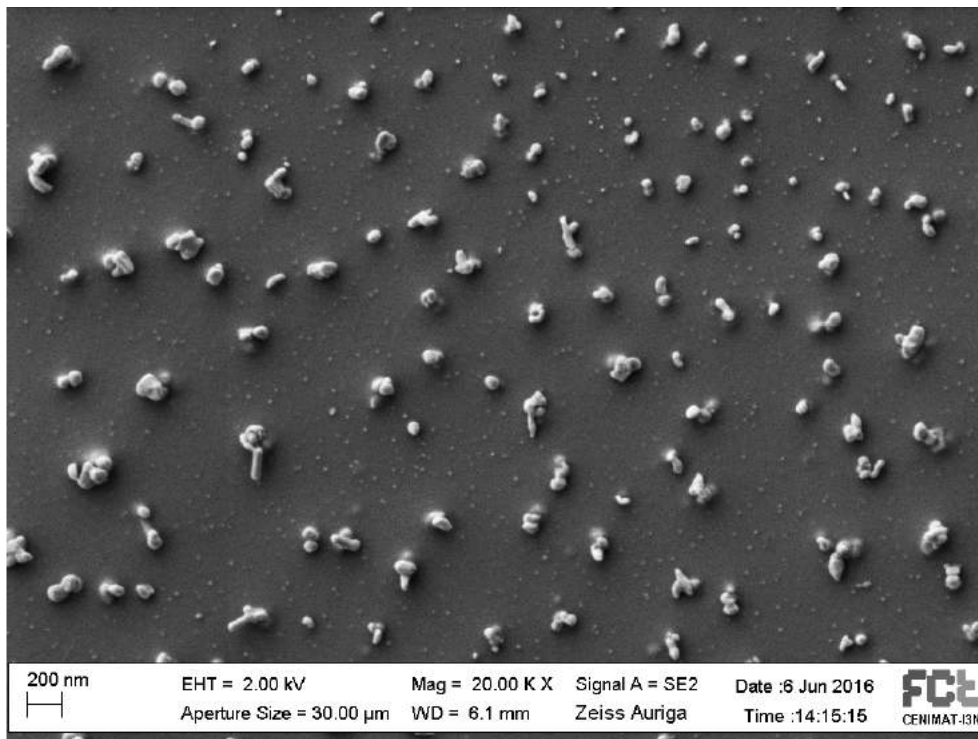

(a) 20k magnificaton.

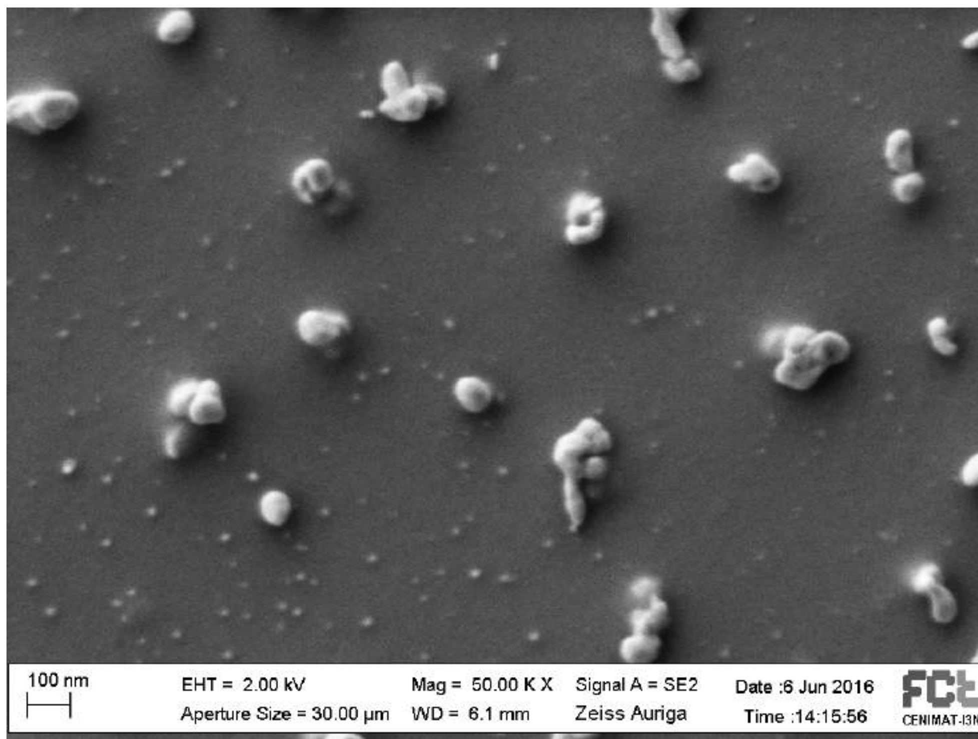

(b) 50k magnification.

Figure 4.25: SEM surface of the sample doped with $0.1\ mmol$ of Ag annealed at $180\ °C$ at two different magnifications, (a) 20k and (b) 50k. Agglomerations are visible.

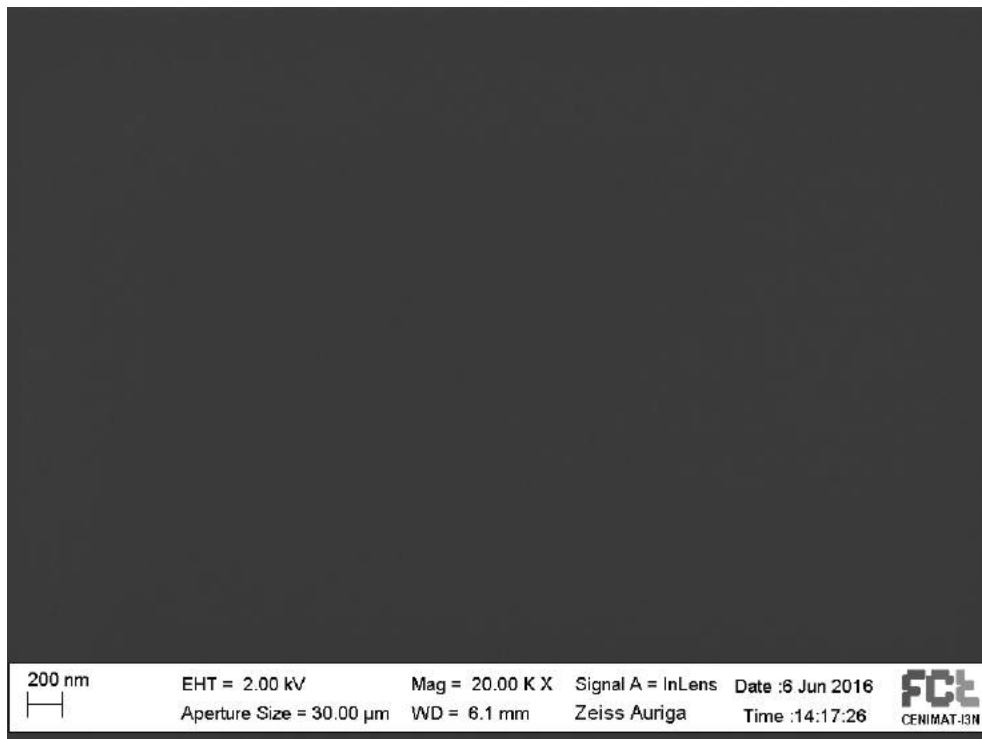

(a) 20k magnificaton.

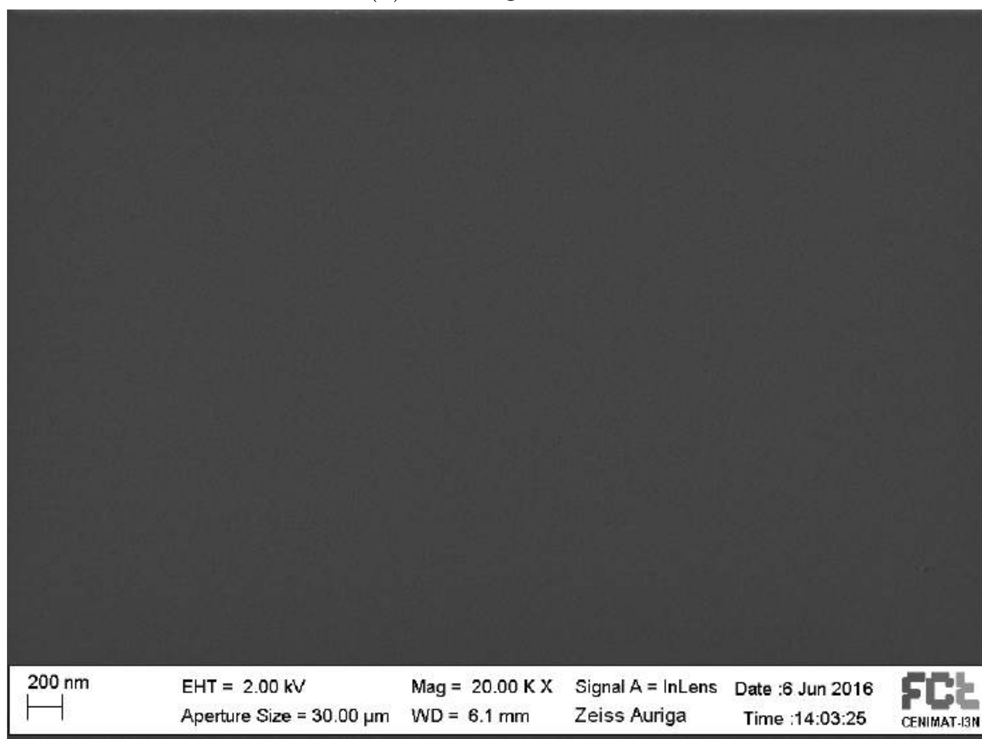

(b) 20k magnification.

Figure 4.26: SEM surface of the samples doped with (a) 0.2 and (b) 0.4 $mmol$ of Ag annealed at 180 $°C$ at 20k of magnification. The surfaces are smooth.

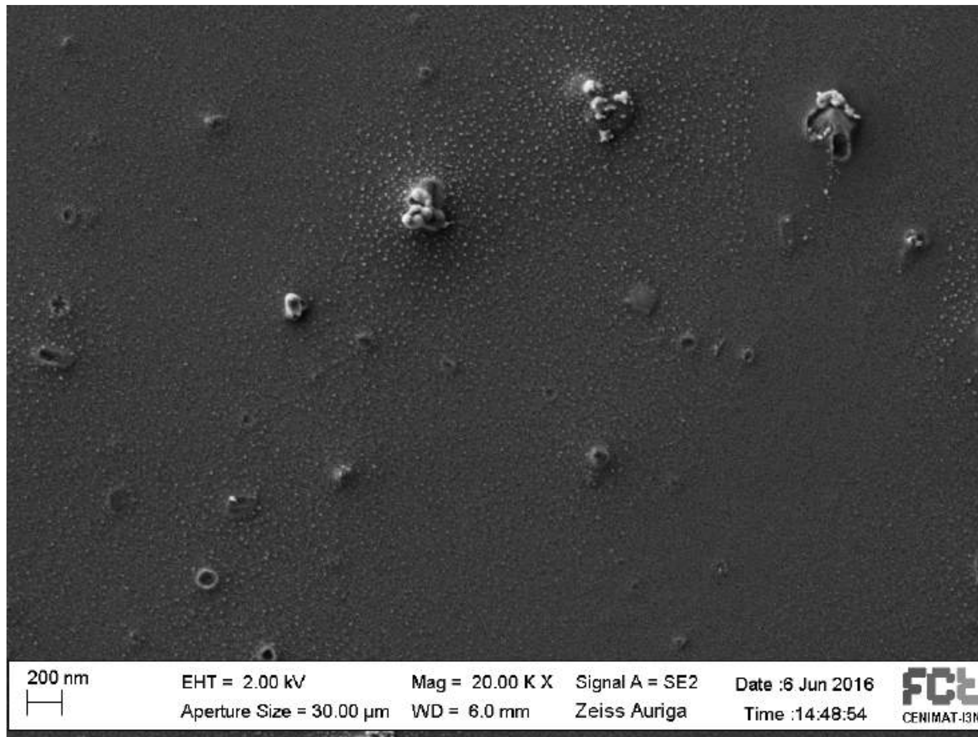

(a) 20k magnificaton.

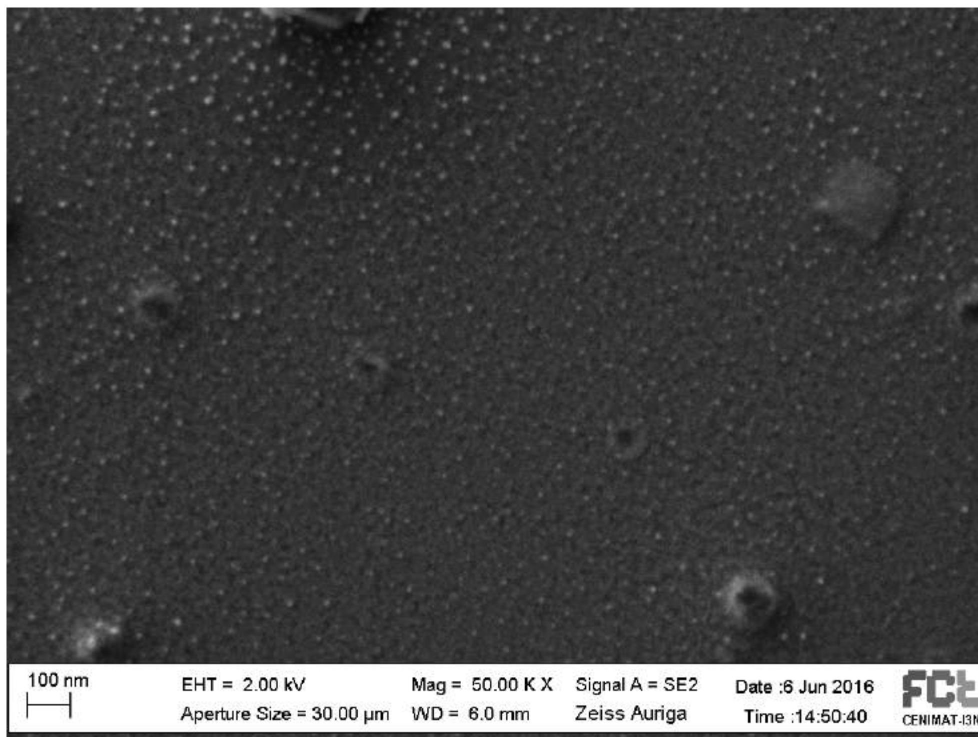

(b) 50k magnification.

Figure 4.27: SEM surface of the sample doped with $0.1\ mmol$ of Ag annealed at $300\ ^{\circ}C$ at two different magnifications, (a) 20k and (b) 50k. Some big clusters are visible.

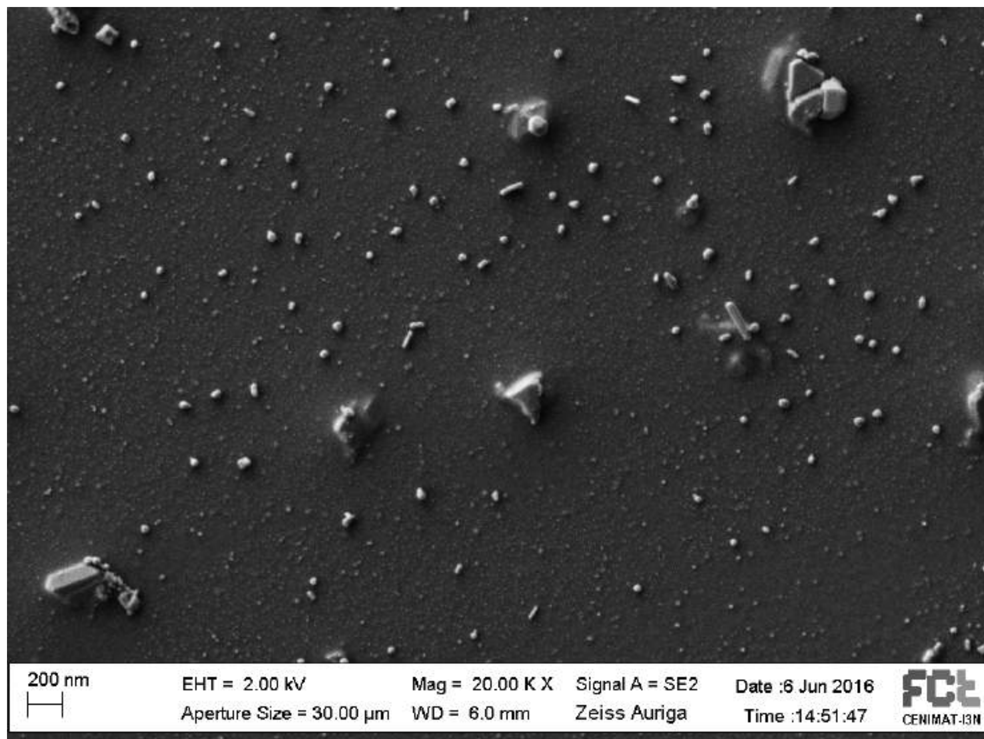

(a) 20k magnificaton.

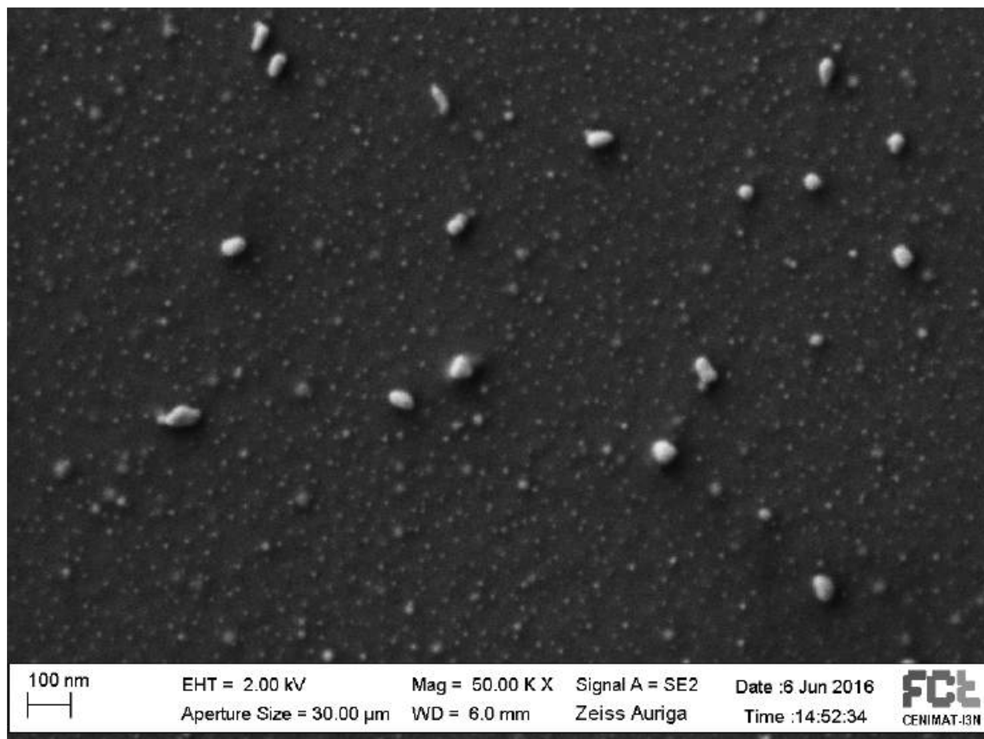

(b) 50k magnification.

Figure 4.28: SEM surface of the sample doped with $0.2\ mmol$ of Ag annealed at $300\ °C$ at two different magnifications, (a) 20k and (b) 50k. Some big clusters and agglomerations are visible.

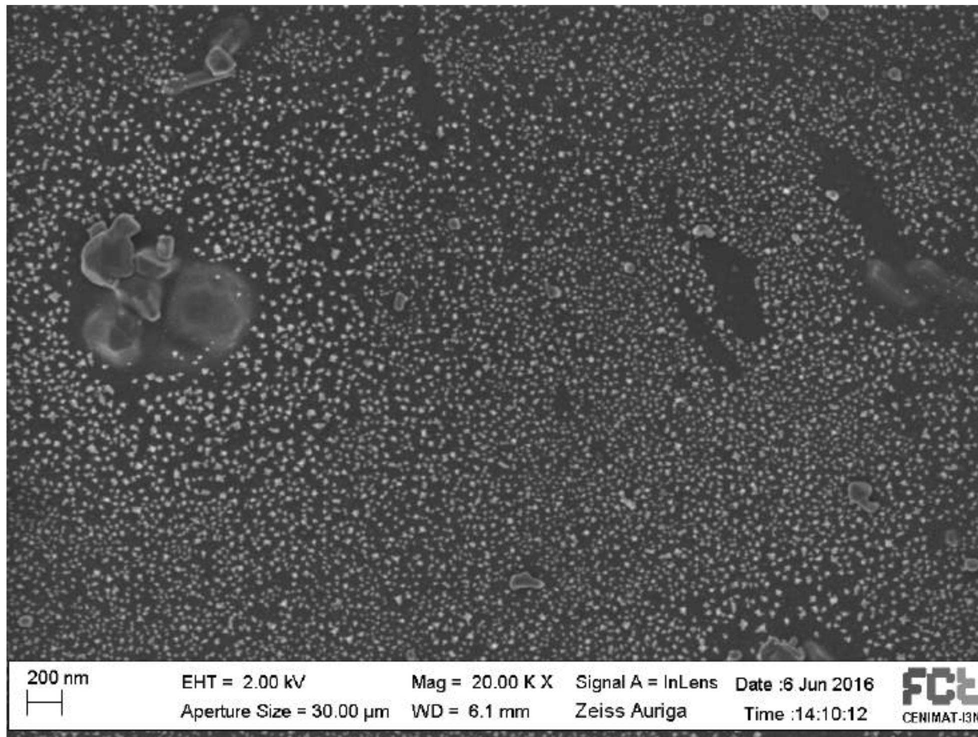

(a) 20k magnificaton.

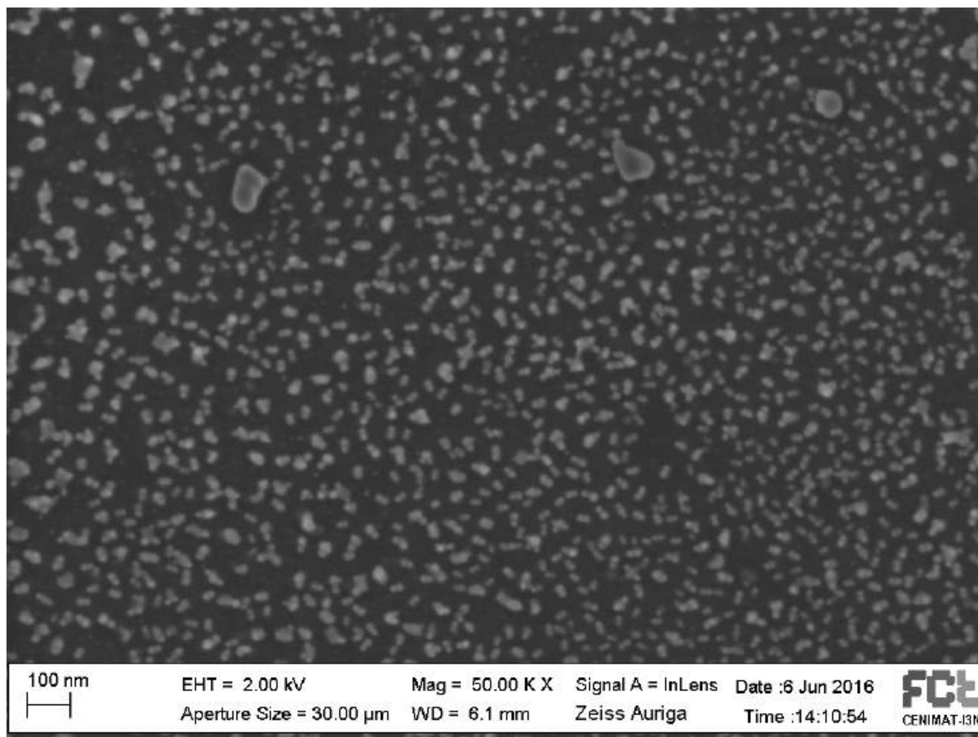

(b) 50k magnification.

Figure 4.29: SEM surface of the sample doped with $0.4\ mmol$ of Ag annealed at $300\ °C$ at two different magnifications, (a) 20k and (b) 50k. Several agglomerations are visible.

Sample		Rms roughness (nm)
Annealed at 180 $°C$	+0.1 $mmol\ Ag$	20.4
	+0.2 $mmol\ Ag$	0.192
	+0.4 $mmol\ Ag$	0.373
Annealed at 300 $°C$	+0.1 $mmol\ Ag$	46.9
	+0.2 $mmol\ Ag$	16.0
	+0.4 $mmol\ Ag$	13.6

Table 4.6: Root mean square roughness of samples analysed with AFM.

In all the films except two (annealed at 180 $°C$), which are amorphous, clusters of agglomerations of particles are present. In order to understand the nature of these structures EDS were acquired and reported in Figure 4.30, Figure 4.31, Figure 4.32, Figure 4.33, Figure 4.34, Figure 4.35, Figure 4.36, Figure 4.37 and Figure 4.38.

As predicted from the XRD images, in samples annealed at 300 $°C$ there are traces of Chlorine while in other samples the presence is negligible. Moreover, clusters are formed by either Tin or Silver, depending on the quantity of Silver in the film. The presence of silicon in all samples is due to the substrate. Films annealed at 150 $°C$ under DUV do not seem amorphous: grains and agglomerations of particles are visible in all the three samples. The sample doped with 0.2 $mmol$ of Ag shows dendrites and is the one with more Silver. In fact, Ag concentration does not seem to have a linear relationship with the amount of extra Silver in the precursor solution. Films annealed at 180 $°C$ have almost no Silver and, in particular, one has no Ag at all. As already visible by SEM images, most doped samples are amorphous and show smooth surfaces, while samples with less amount of extra Silver show something like a crystal structure. Films annealed at 300 $°C$ are the most interesting: the sample less doped has almost no Ag and has a crystalline-like structure. Sample doped with 0.2 $mmol$ of Ag has some islands of particles, which are made of Tin (75%) and Silver (25%). The most doped sample has some agglomerations too but, on the contrary, they are made mainly of Silver.

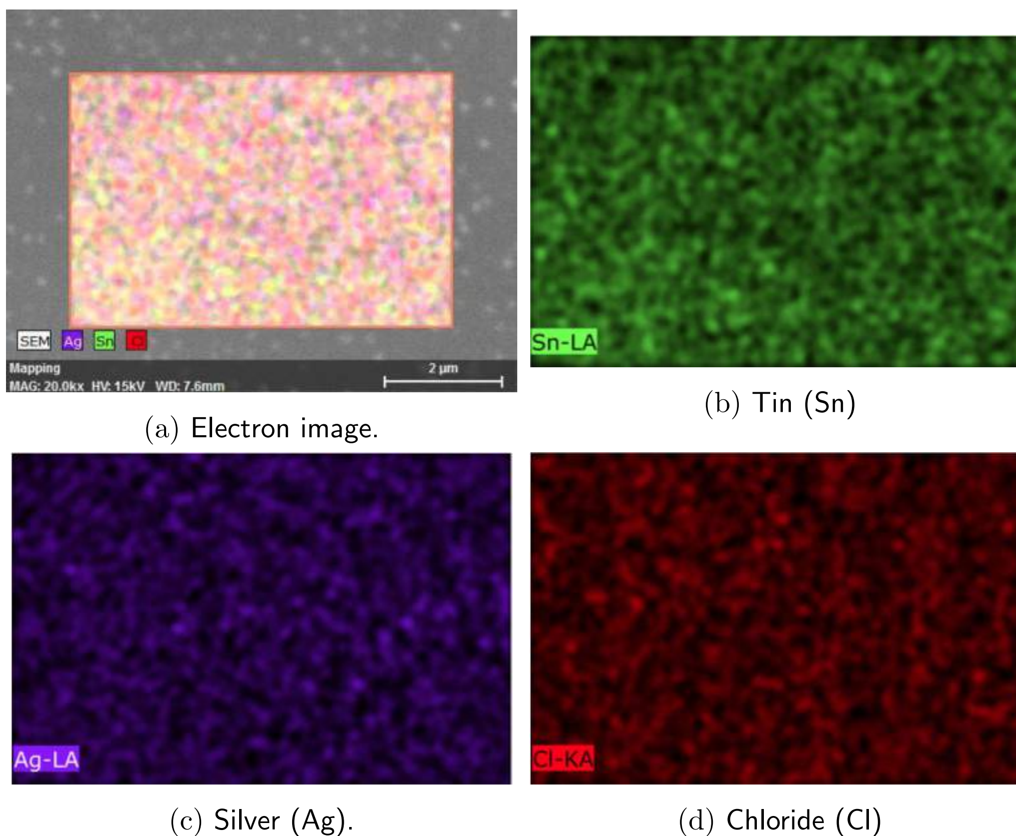

(a) Electron image.

(b) Tin (Sn)

(c) Silver (Ag).

(d) Chloride (Cl)

Element	Apparent Concentration	Wt%	Wt% Sigma	Atomic %
C	0.88	8.78	0.23	17.51
O	12.07	12.54	0.08	18.76
Si	107.92	73.52	0.20	62.67
Cl	0.01	0.01	0.01	0.01
Ag	0.35	0.40	0.04	0.09
Sn	4.17	4.74	0.05	0.96
Total:		100.00		100.00

(e) Weight and percentage of atoms in sample's surface.

Figure 4.30: Surface map acquired by EDS of sample doped with $0.1\ mmol$ of Ag and annealed at $150\ °C$ under DUV. Here are reported the (a) electron map and the presence of (b) Tin, (c) Silver and (d) Chlorine. Table (e) shows weight and percentage of atoms in the sample's surface.

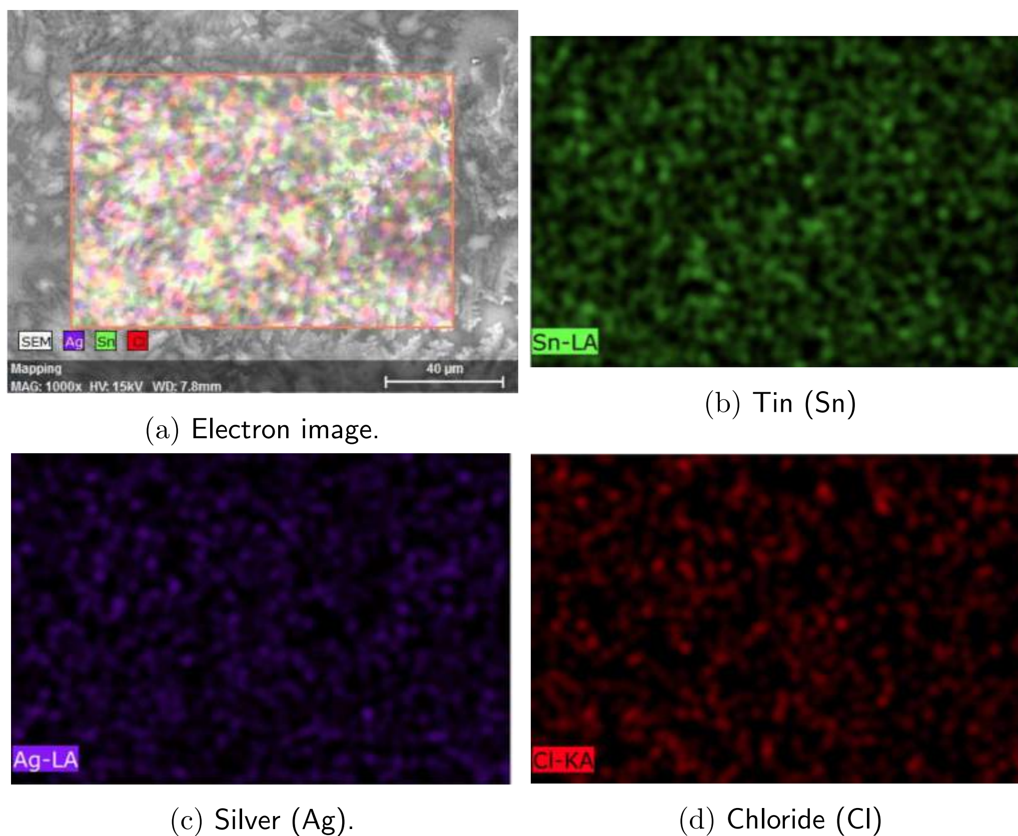

(a) Electron image.

(b) Tin (Sn)

(c) Silver (Ag).

(d) Chloride (Cl)

Element	Apparent Concentration	Wt%	Wt% Sigma	Atomic %
C	0.99	9.43	0.23	19.19
O	11.07	11.63	0.08	17.78
Si	104.06	72.99	0.21	60.91
Cl	0.02	0.02	0.01	0.01
Ag	1.39	1.56	0.04	0.35
Sn	3.90	4.37	0.05	0.90
Total:		100.00		100.00

(e) Weight and percentage of atoms in sample's surface.

Figure 4.31: Surface map acquired by EDS of sample doped with $0.2\ mmol$ of Ag and annealed at $150\ °C$ under DUV. Here are reported the (a) electron map and the presence of (b) Tin, (c) Silver and (d) Chlorine. Table (e) shows weight and percentage of atoms in the sample's surface.

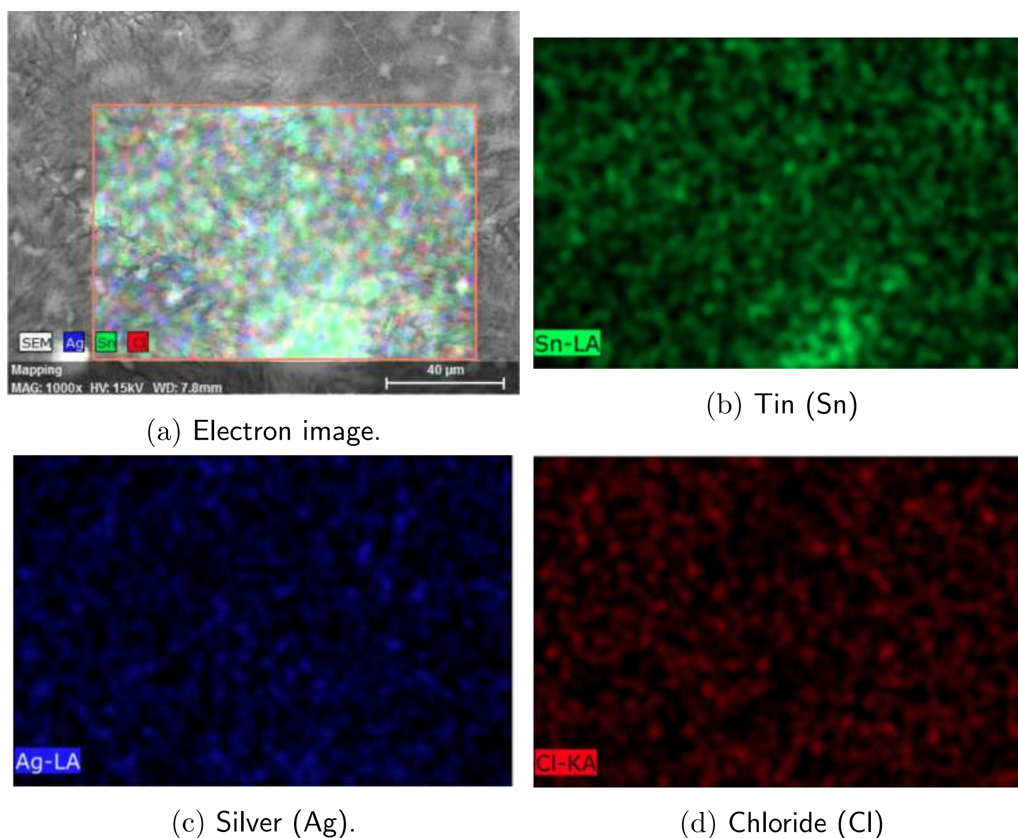

(a) Electron image.

(b) Tin (Sn)

(c) Silver (Ag).

(d) Chloride (Cl)

Element	Apparent Concentration	Wt%	Wt% Sigma	Atomic %
C	0.89	8.88	0.23	17.75
O	11.68	12.28	0.08	18.44
Si	106.77	73.24	0.20	62.65
Cl	0.01	0.01	0.01	0.01
Ag	0.59	0.68	0.04	0.15
Sn	4.29	4.91	0.05	0.99
Total:		100.00		100.00

(e) Weight and percentage of atoms in sample's surface.

Figure 4.32: Surface map acquired by EDS of sample doped with $0.4\ mmol$ of Ag and annealed at $150\ °C$ under DUV. Here are reported the (a) electron map and the presence of (b) Tin, (c) Silver and (d) Chlorine. Table (e) shows weight and percentage of atoms in the sample's surface.

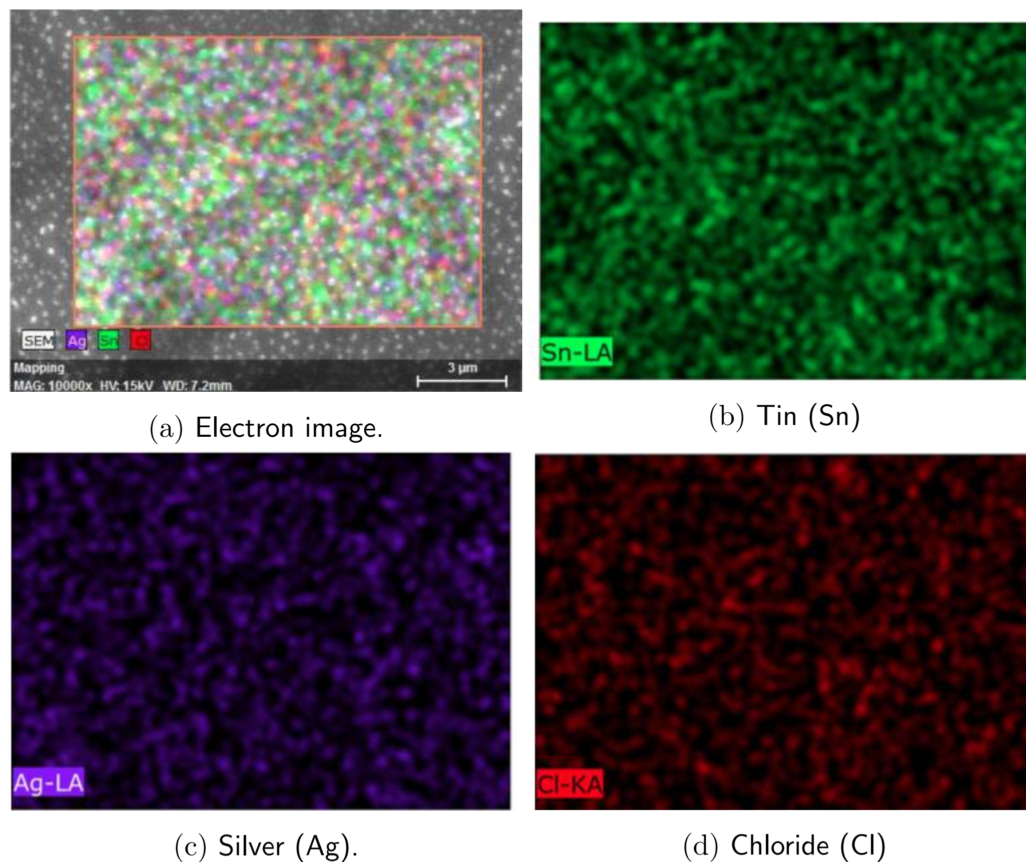

(a) Electron image.

(b) Tin (Sn)

(c) Silver (Ag).

(d) Chloride (Cl)

Element	Apparent Concentration	Wt%	Wt% Sigma	Atomic %
C	0.95	9.53	0.23	18.89
O	11.59	12.28	0.08	18.28
Si	105.59	72.85	0.20	61.75
Cl	0.00	0.00	0.01	0.00
Ag	0.56	0.64	0.04	0.14
Sn	4.08	4.69	0.05	0.94
Total:		100.00		100.00

(e) Weight and percentage of atoms in sample's surface.

Figure 4.33: Surface map acquired by EDS of sample doped with $0.1\ mmol$ of Ag and annealed at $180\ °C$. Here are reported the (a) electron map and the presence of (b) Tin, (c) Silver and (d) Chlorine. Table (e) shows weight and percentage of atoms in the sample's surface.

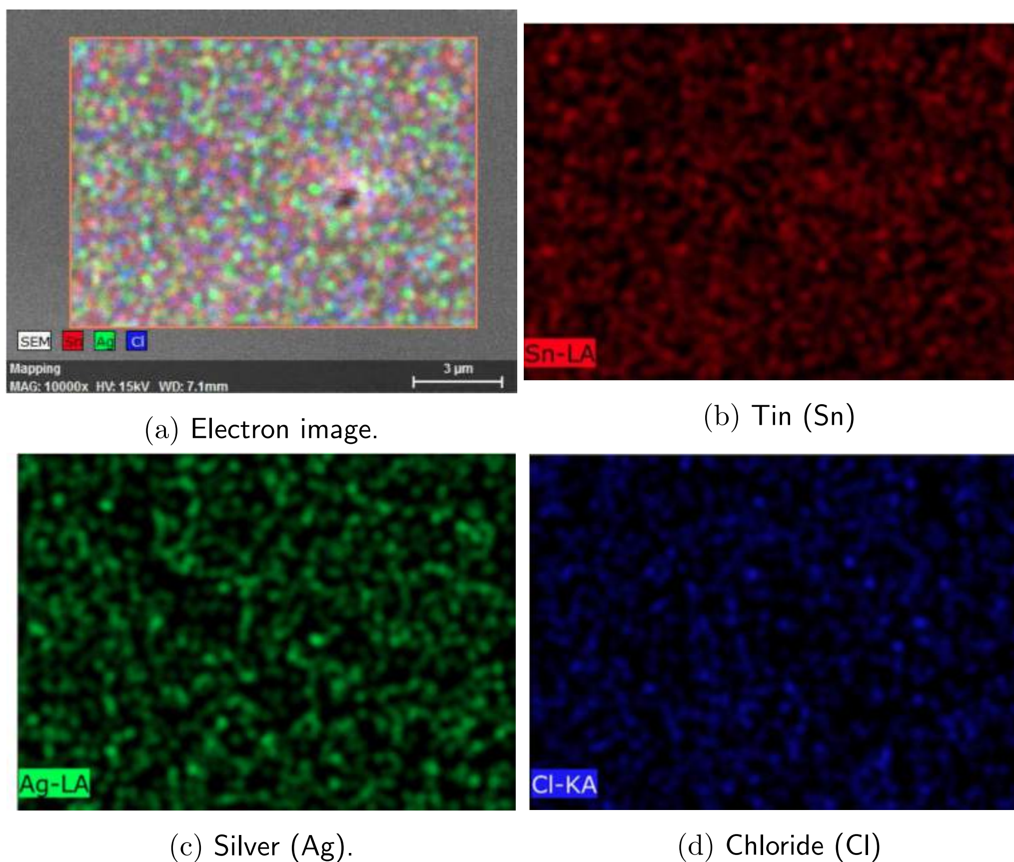

(a) Electron image.

(b) Tin (Sn)

(c) Silver (Ag).

(d) Chloride (Cl)

Element	Apparent Concentration	Wt%	Wt% Sigma	Atomic %
C	0.89	9.15	0.23	18.09
O	11.67	12.20	0.08	18.10
Si	108.91	74.52	0.21	62.98
Cl	0.00	0.00	0.01	0.00
Ag	0.00	0.00	0.00	0.00
Sn	3.59	4.13	0.04	0.83
Total:		100.00		100.00

(e) Weight and percentage of atoms in sample's surface.

Figure 4.34: Surface map acquired by EDS of sample doped with $0.2\ mmol$ of Ag and annealed at $180\ °C$. Here are reported the (a) electron map and the presence of (b) Tin, (c) Silver and (d) Chlorine. Table (e) shows weight and percentage of atoms in the sample's surface.

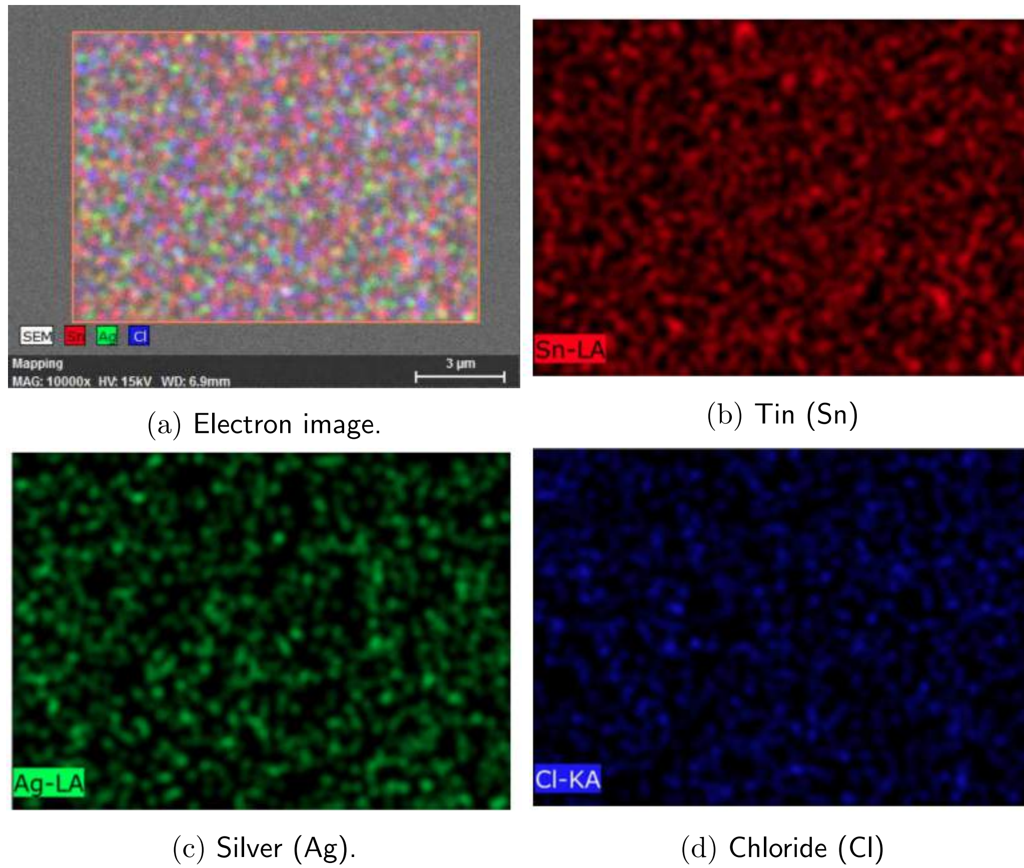

(a) Electron image.

(b) Tin (Sn)

(c) Silver (Ag).

(d) Chloride (Cl)

Element	Apparent Concentration	Wt%	Wt% Sigma	Atomic %
C	0.89	9.13	0.23	18.10
O	11.42	11.97	0.08	17.81
Si	109.05	74.63	0.21	63.24
Cl	0.00	0.00	0.00	0.00
Ag	0.02	0.03	0.03	0.01
Sn	3.69	4.24	0.04	0.85
Total:		100.00		100.00

(e) Weight and percentage of atoms in sample's surface.

Figure 4.35: Surface map acquired by EDS of sample doped with $0.4\ mmol$ of Ag and annealed at $180\ °C$. Here are reported the (a) electron map and the presence of (b) Tin, (c) Silver and (d) Chlorine. Table (e) shows weight and percentage of atoms in the sample's surface.

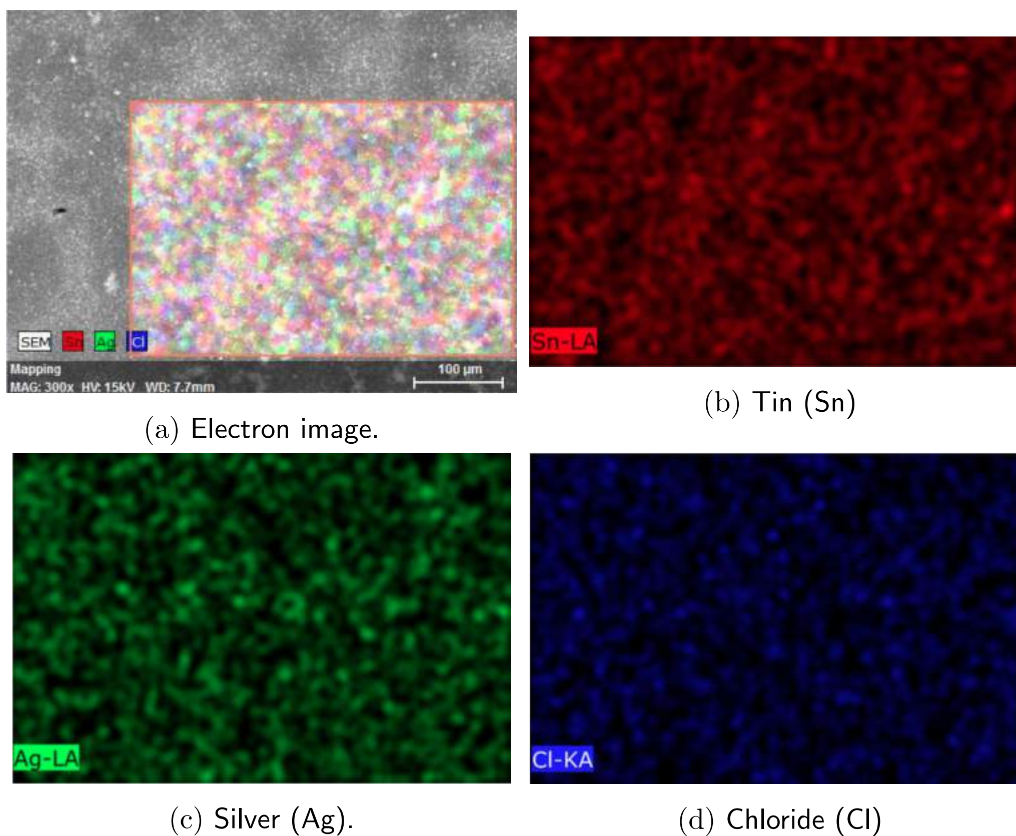

(a) Electron image.

(b) Tin (Sn)

(c) Silver (Ag).

(d) Chloride (Cl)

Element	Apparent Concentration	Wt%	Wt% Sigma	Atomic %
C	0.91	9.17	0.23	18.30
O	11.00	11.60	0.08	17.37
Si	108.64	74.19	0.20	63.30
Cl	0.02	0.02	0.01	0.01
Ag	0.24	0.28	0.04	0.06
Sn	4.15	4.74	0.05	0.96
Total:		100.00		100.00

(e) Weight and percentage of atoms in sample's surface.

Figure 4.36: Surface map acquired by EDS of sample doped with $0.1\ mmol$ of Ag and annealed at $300\ °C$. Here are reported the (a) electron map and the presence of (b) Tin, (c) Silver and (d) Chlorine. Table (e) shows weight and percentage of atoms in the sample's surface.

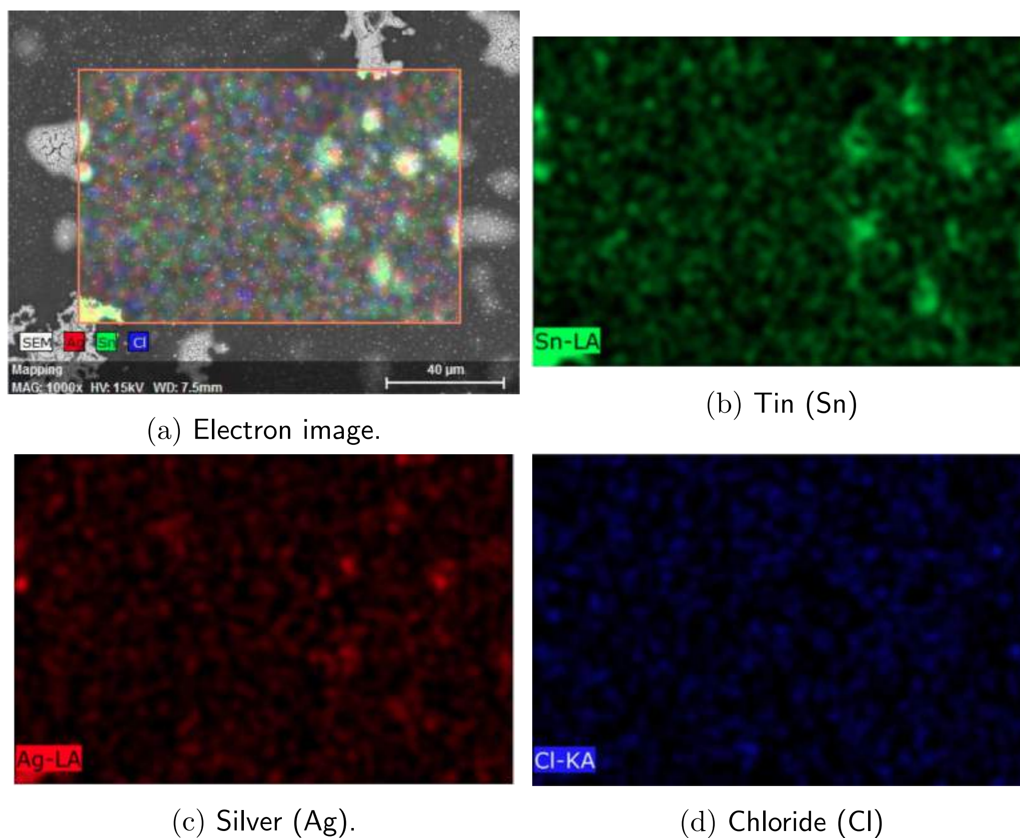

(a) Electron image.

(b) Tin (Sn)

(c) Silver (Ag).

(d) Chloride (Cl)

Element	Apparent Concentration	Wt%	Wt% Sigma	Atomic %
C	1.71	11.78	0.20	24.70
O	12.93	14.87	0.09	23.42
Si	71.99	52.86	0.14	47.40
Cl	0.18	0.16	0.01	0.12
Ag	2.14	2.32	0.05	0.54
Sn	16.45	18.00	0.07	3.82
Total:		100.00		100.00

(e) Weight and percentage of atoms in sample's surface.

Figure 4.37: Surface map acquired by EDS of sample doped with $0.2\ mmol$ of Ag and annealed at $300\ °C$. Here are reported the (a) electron map and the presence of (b) Tin, (c) Silver and (d) Chlorine. Table (e) shows weight and percentage of atoms in the sample's surface.

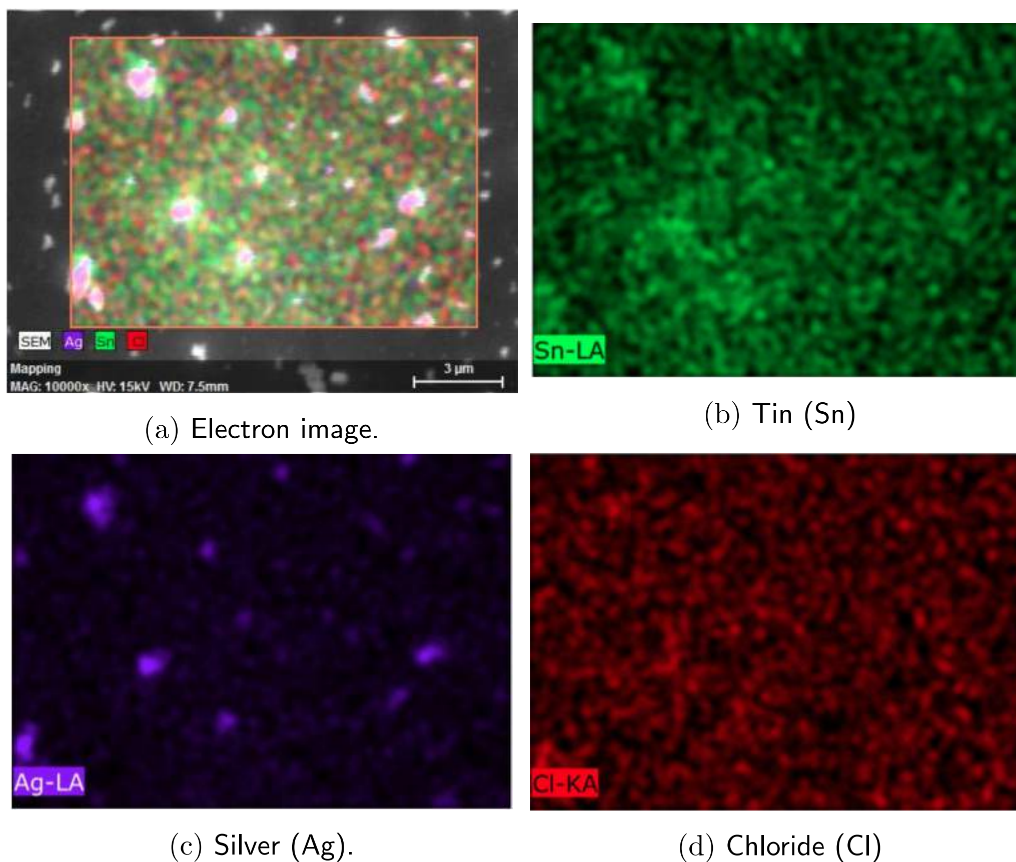

(a) Electron image.

(b) Tin (Sn)

(c) Silver (Ag).

(d) Chloride (Cl)

Element	Apparent Concentration	Wt%	Wt% Sigma	Atomic %
C	0.86	8.65	0.23	17.49
O	10.72	11.53	0.08	17.51
Si	106.23	73.57	0.20	63.64
Cl	0.10	0.10	0.01	0.07
Ag	1.36	1.58	0.04	0.36
Sn	3.96	4.58	0.05	0.94
Total:		100.00		100.00

(e) Weight and percentage of atoms in sample's surface.

Figure 4.38: Surface map acquired by EDS of sample doped with $0.4\ mmol$ of Ag and annealed at $300\ °C$. Here are reported the (a) electron map and the presence of (b) Tin, (c) Silver and (d) Chlorine. Table (e) shows weight and percentage of atoms in the sample's surface.

After surface analysis, the electrical properties of the doped samples were also studied. Like other devices already considered, the transfer characteristics were acquired and are reported in Figure 4.39. The width/length ratio (W/L) for all the devices is 14. Only the curves of samples annealed at 180 $°C$ look like transfer characteristics but the I_{ON}/I_{OFF} ratio is really low (around 10) while the other curves do not show the typical shape of a transfer curve. For this reason, is meaningless to report the output characteristics curves.

The sample lightly doped and annealed at 300 $°C$ seems to be a good conductive material even if it is worse than the device deposited with stoichiometric solution. For this reason, Hall measurements were made and reported in Table 4.7, where R_s is the sheet resistance, ρ is the resistivity, μ_H is the Hall mobility, μ is the carrier mobility, n_s is the sheet carrier density and n is the bulk carrier density.

Resistivity		**Mobility**		**Carrier concentration**	
R_s (Ω/sq)	ρ $(\Omega \cdot cm)$	μ_H (m^2/C)	μ $(cm^2/V\ s)$	n_s/cm^2	n/cm^3
$5.10 \cdot 10^9$	$1.89 \cdot 10^4$	$-1.68 \cdot 10^6$	3.18	$-4.45 \cdot 10^8$	$-1.20 \cdot 10^{14}$

Table 4.7: Electrical properties measured using Hall measurement system for the sample doped with 0.1 $mmol$ of Ag annealed at 300 $°C$.

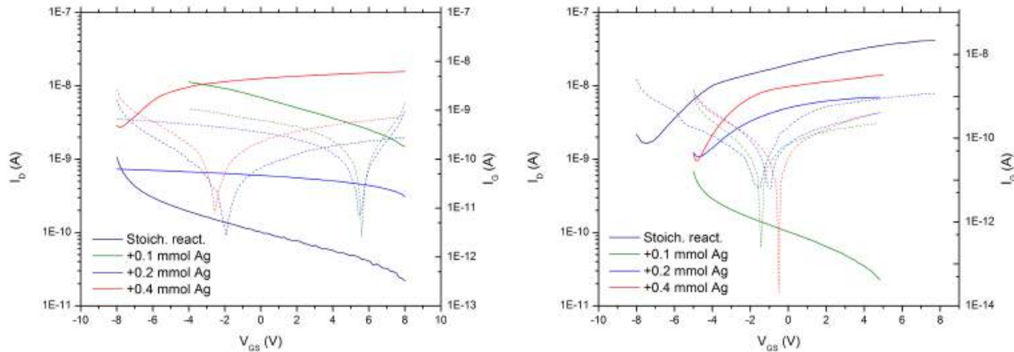

(a) Samples annealed at $150\ ^{\circ}C$ with DUV. (b) Samples annealed at $180\ ^{\circ}C$.

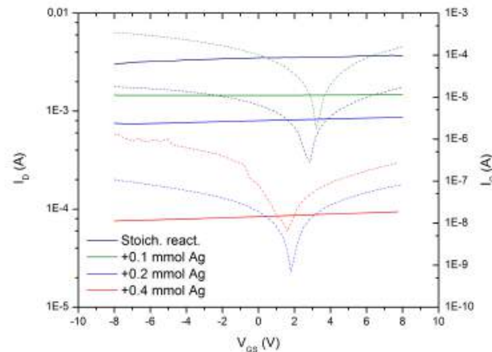

(c) Samples annealed at $300\ ^{\circ}C$.

Figure 4.39: Transfer characteristic curves for the doped samples annealed at (a) $150\ ^{\circ}C$ under DUV, (b) $180\ ^{\circ}C$, and (c) $300\ ^{\circ}C$. In the left y-axis the drain current (I_D) values are reported while in the right y-axis the gate leakage current (I_G) values are reported with dashed lines. All the measures were made with $V_D = 8\ V$ and V_{GS} that sweep from $-8\ V$ to $+8\ V$. The width/length ratio (W/L) is 14 for all the devices.

Chapter 5

Conclusions

This thesis work was focused on the use of Solution Combustion Synthesis in order to produce SnO_x thin films, possibly Tin (II) Oxide, a p-type semiconductor, in order to have the possibility to produce low-cost low-temperature complementary devices (i.e. CMOS) with all-oxide n-type and p-type semiconductors.

The first important thing to highlight is the effectiveness of the Solution Combustion Synthesis method. From FTIR spectra is clear that all the samples deposited have no more organic compounds, even the ones annealed at 150 $°C$ under DUV and at 180 $°C$. Another important result, common to all the films, is the value of energy gaps (E_G). There is an agreement of all the data around 3.79 eV, which is good for transparent devices, and agrees with the value of SnO_2. In Figure 5.1 all the values with their own errors are reported, excluding samples with a not reliable thickness value (i.e. samples with χ^2 of thickness over 10).

To better discuss other properties, the samples are divided into four categories depending on the annealing temperature used (150 $°C$ under DUV, 180 $°C$, 250 $°C$ and 300 $°C$).

5.1 Annealing at 150 $°C$ under DUV

All samples annealed at this temperature are amorphous but most doped samples have a peak in XRD measure typical of Ag. From SEM images of the

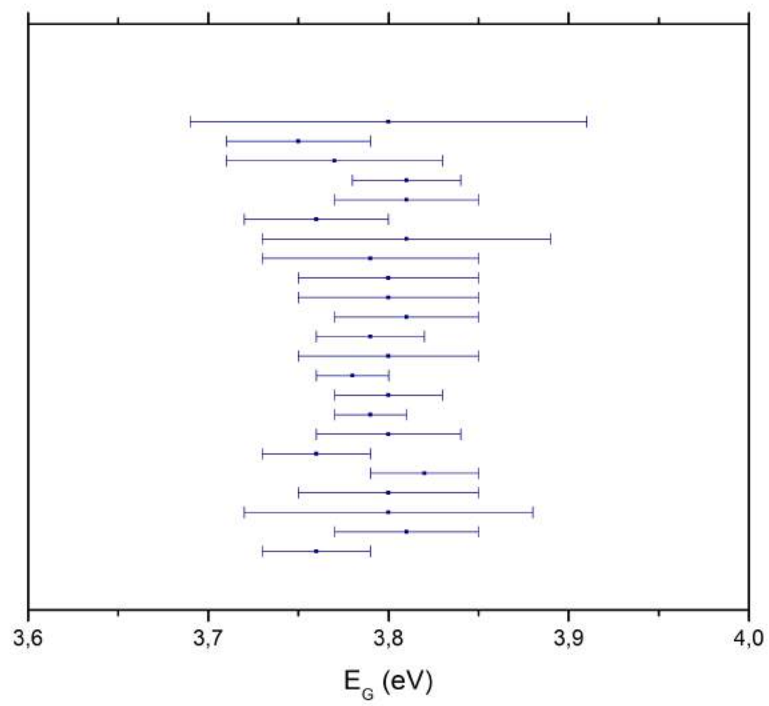

Figure 5.1: Energy gap values and error for all the samples analysed in this work which had a reliable value of thickness.

surface adendrites and agglomerations of particles are visible, mainly made by Tin. This could be the reason why these films have the worst transmittance, in particular with a big drop (40% of transmittance for the most doped sample) around 2.5 eV. Non-doped films do not act as semiconductors in TFT devices and are bad as a conductive material anyway. In doped samples the conductivity is slightly increased and the most doped film acts as n-type semiconductor with very low I_{ON}/I_{OFF} ratio, lower than 10. However, none of the samples turned out to be nor a p-type semiconductor neither a good conductor.

5.2 Annealing at 180 °C

Samples annealed at 180 °C are amorphous, regardless of precursors or doping, except for sample doped with 0.1 *mmol* of Ag which has some agglomerations visible from SEM and EDS analysis. These are the only films which have no drop of transmittance when doped, probably just due to their smooth structures. Moreover, the samples deposited using $AgNO_3$ as precursor act as n-type semiconductor in TFT devices, even in this case with exception for sample doped with 0.1 *mmol* of Ag. Other doped films have about the same electrical properties of the non-doped one, so the role of Silver doping is not really appreciable. As for samples annealed at 150 °C, the I_{ON}/I_{OFF} ratios are really low, even if they are slightly better. However, none of the samples turned out to be nor a p-type semiconductor neither a good conductor.

5.3 Annealing at 250 °C

These samples were only deposited with stoichiometric reactions. They are amorphous and conductive but since they are not good as the samples annealed at 300 °C, further investigations were not made.

5.4 Annealing at 300 $^\circ C$

Samples annealed at 300 $^\circ C$ were investigated the most. All samples with 3 and 4 layers are crystalline. Films deposited with the stoichiometric reaction have the structure of SnO_2 while the doped ones have peaks of Ag and $AgCl$. Presence of $AgCl$ or Chlorine in general, that was confirmed by the EDS analysis, should be avoided because it could make electrical properties worse and the easiest way to do it is to centrifuge the solution for more time or doing it multiple times, since $AgCl$ is solid.

Moreover, it was found that samples with 4 layers deposited with 30 min of annealing are the best conductive materials. Samples with a different number of layers or less annealing time have worse electrical properties.

As for samples annealed at 150 $^\circ C$ under DUV, doped samples have a drop of transmittance around 2.5 eV and is reasonable to think that even in this case this is due to the structures that appear in the films with the doping. These structures are visible with SEM and EDS analysis and they are made of Tin or Silver. These grains could also be the reason of the degradation of electrical conductivity. In fact samples annealed at this temperatures act as conductive layer and the most conductive film deposited is the one with stoichiometric reaction as precursor. Anyway, even in this case, doping with Silver did not help to get a p-type semiconductor.

5.5 Future prospective

In this research work some questions and routes remain unknown and unanswered after this dissertation. Based on the results obtained here, two main ways are suggested: one in order to try to get p-type SnO and the other in order to improve electrical properties of SnO_2 for TCO devices.

One of the reasons why p-type SnO was not obtained could be oxidation of the films during spin coating and annealing, that were performed in air condition. Using glove box with N_2 atmosphere could prevent this phenomenon. Another study could be done with concentrations of Silver doping different from the ones used in this work. Finally, changing the fuel-to-oxidizer ratio

of the solutions could lead to films with different properties.

A way to optimise SnO_2 for TCO devices could be doping the films, as reported in literature. There are big differences between the state of the art for TCO based on SnO_2[63][64] and the best one of this thesis work, but is important to keep in mind that the main goal of this thesis was not to produce optimised TCOs. By changing deposition parameters and doping nature and concentration, comparable results may be achieved.

Bibliography

[1] E. Fortunato, R. Barros, P. Barquinha, V. Figueiredo, S. K. Park, C. Hwang, and R. Martins, Transparent p-type SnO_x thin film transistors produced by reactive rf magnetron sputtering followed by low temperature annealing, Appl. Phys. Lett., vol. 97, no. 5, 2010.

[2] P. Barquinha, L. Pereira, G. Gonçalves, R. Martins, and E. Fortunato, Toward High-Performance Amorphous GIZO TFTs, J. Electrochem. Soc., vol. 156, no. 3, p. H161, 2009.

[3] E. M. C. Fortunato, P. M. C. Barquinha, A. C. M. B. G. Pimentel, a. M. F. Gonçalves, A. J. S. Marques, L. M. N. Pereira, R. F. P. Martins, and A. M. F. Gonçalves, Fully Transparent ZnO Thin-Film Transistor Produced at Room Temperature, Adv. Mater., vol. 17, no. 5, pp. 590-594, Mar. 2005.

[4] C. D. Dimitrakopoulos and P. R. L. Malenfant, Organic Thin Film Transistors for Large Area Electronics, Adv. Mater., vol. 14, no. 2, pp. 99-117, Jan. 2002.

[5] R. Martins, P. Barquinha, a. Pimentel, L. Pereira, and E. Fortunato, Transport in high mobility amorphous wide band gap indium zinc oxide films, Phys. Status Solidi, vol. 202, no. 9, pp. 95-97, Jul. 2005.

[6] C. Avis and J. Jang, High-performance solution processed oxide TFT with aluminum oxide gate dielectric fabricated by a sol-gel method, J. Mater. Chem., vol. 21, no. 29, p. 10649, 2011.

[7] S.-Y. Han, G. S. Herman, and C. Chang, Low-temperature, high-performance, solution-processed indium oxide thin-film transistors., J. Am. Chem. Soc., vol. 133, no. 14, pp. 5166-9, Apr. 2011.

[8] W. A. MacDonald, Engineered films for display technologies, J. Mater. Chem., vol. 14, no. 1, p. 4, Dec. 2004.

[9] H. C. Yi and J. J. Moore, Self-propagating high-temperature (combustion) synthesis (SHS) of powder-compacted materials, J. Mater. Sci., vol. 25, no. 2, pp. 1159-1168, 1990.

[10] K. Okamura, B. Nasr, R. A. Branda and H. Hahn, Solution-processed oxide semiconductor SnO in p-channel thin-film transistors, J. Mater. Chem., 2012, 22, 4607.

[11] L. Luo, D. Bozyigit, V. Wood and M. Niederberger, High-Quality Transparent Electrodes Spin-Cast from Preformed Antimony-Doped Tin Oxide Nanocrystals for Thin Film Optoelectronics, Chem. Mater. 2013, 25, 4901-4907.

[12] Minami, Tadatsugu, Transparent conducting oxide semiconductors for transparent electrodes. Semiconductor Science and Technology. 20 (4): S35 (2005).

[13] Dominici, L; Michelotti, F; Brown, TM; et al., Plasmon polaritons in the near infrared on fluorine doped tin oxide films. Optics Express. 17: 10155 (2009).

[14] P. P. Edwards, A. Porch, M. O. Jones, D. V. Morgan, and R. M. Perks, Basic materials physics of transparent conducting oxides, Dalton Trans. 19, 2995 (2004).

[15] H. Mizoguchi and P.M. Woodward, Electronic Structure Studies of Main Group Oxides Possessing Edge-Sharing Octahedra: Implications for the Design of Transparent Conducting Oxides, Chem. Mater., 16, 5233 (2004).

[16] C. Kiliç and A. Zunger, Origins of Coexistence of Conductivity and Transparency in SnO_2, Phys. Rev. Lett., 88, 095501-1 (2002).

[17] C.G. Van de Walle, Hydrogen as a Cause of Doping in Zinc Oxide, Phys. Rev. Lett., 85, 1012 (2000).

[18] G. Masetti, M. Severi, S. Solmi, Modeling of carrier mobility against carrier concentration in arsenic-, phosphorus-, and boron-doped silicon, IEEE Trans. Electron Devices, ED30, 764 (1983).

[19] P. Ebert, Z. Zhang, F. Kluge, M. Simon, Z. Zhang, K. Urban, Importance of Many-Body Effects in the Clustering of Charged Zn Dopant Atoms in $GaAs$, Phys. Rev.Lett., 83, 757 (1999).

[20] Chen, Zhangxian, Fabrication of Highly Transparent and Conductive Indium-Tin Oxide Thin Films with a High Figure of Merit via Solution Processing. Langmuir. 29: 13836-13842 (2013).

[21] S. Wagner, H. Gleskova, I.-C. Cheng, and M. Wu, Silicon for thin-film transistors, Thin Solid Films, vol. 430, no. 1-2, pp. 15-19, 2003.

[22] A. C. Tickle, Thin-film transistors: a new approach to microelectronics. New York: John Wiley and Sons Inc, 1969.

[23] P. Barquinha, R. Martins, L. Pereira, and E. Fortunato, Transparent Oxide Electronics, Mar. 2012.

[24] M. M. Valencia, p-Type Transparent Electronics, Master Thesis:Oregon State University, 2003.

[25] E. Fortunato, P. Barquinha, and R. Martins, Oxide semiconductor thin-film transistors: a review of recent advances., Adv. Mater., vol. 24, no. 22, pp. 2945-86, Jun. 2012.

[26] C. R. Kagan and P. Andry, Thin-film Transistors. Marcel Dekker, Inc., 2003.

[27] C. R. Kagan and P. Andry, Thin-Film Transistors. New York: Marcel Dekker, Inc, 2003.

[28] D. K. Schroder, Semiconductor Material and Device Characterization. John Wiley and Sons, Inc., 2006.

[29] S. L. González-Cortés, F. E. Imbert, Fundamentals, properties and applications of solid catalysts prepared by solution combustion synthesis (SCS), Applied Catalysis A: General 452 (2013) 117-131.

[30] M. Kim, M. G. Kanatzidis, A. Facchetti, T. J. Marks, Low-temperature fabrication of high-performance metal oxide thin-film electronics via combustion processing, Nature Materials vol. 10, pages 382-388 (2011).

[31] S. R. Jain, K. C. Adiga and V. R. Pai Verneker, A New Approach to Thermochemical Calculations of Condensed Fuel-Oxidizer Mixtures, December 1981Combustion and Flame 40 (C): 71-79.

[32] M. Barrere, A. Jaumotte, B.F. DeVeubeke and J. Vandenkerekhove, Rocket Propulsion Elsevier, Amsterdam, 1960, pp. 132-134.

[33] N. N. Bakhman, Combust. Explo. Shock Waves 4: 9 (1968).

[34] L. Luxmann, R. Dobner, Metall (Berlin) 34 (1980) 821.

[35] K. Hasselbach, G. Murken, M. Troömel, Mössbauer-Messungen an Sn_2O_3, Z. Anorg. Allg. Chem. 897 (1973) 127.

[36] F.D. Rossini, D.D. Wagman, W.H. Evans, S. Levin, I. Jaffe, Selected Values of Chemical Thermodynamic Properties,CircularoftheNationalBureauofStandards500,U.S.GovernmentPrintingOffice, Washington, DC, 1952.

[37] D.N. Klushin, O.V. Nadinskaya, K.G. Bogatina, Zh. Prikl. Khim. (Leningrad) 32 (1959) 273.

[38] J. Geurts, S. Rau, W. Richter, F.J. Schmitte, SnO films and their oxidation to SnO_2: Raman scattering, IR reflectivity and X-ray diffraction studies, Thin Solid Films 121 (1984) 217.

[39] G.W. Watson, The origin of the electron distribution in SnO, J. Chem. Phys. 114 (2001) 758.

[40] A. Togo, F. Oba, I. Tanaka, K. Tatsumi, First-principles calculations of native defects in tin monoxide, Phys. Rev. B 74 (2006) 195128.

[41] J.P. Allen, D.O. Scanlon, L.F.J. Piper, G.W. Watson, Understanding the defect chemistry of tin monoxide, J. Mater. Chem. C 1 (2013) 8194.

[42] X.Q. Pan, L. Fu, Tin oxide thin films grown on the (1012) sapphire substrate, J. Electroceram. 7 (2001) 35-46.

[43] K. J. Saji, Y.P. V. Subbaiah, K. Tian, A. Tiwari, P-type SnO thin films and SnO/ZnO heterostructures for all-oxide electronic and optoelectronic device applications, Thin Solid Films 605 (2016) 193-201.

[44] G.W. Watson, The origin of the electron distribution in SnO, J. Chem. Phys. 114 (2001) 758.

[45] Y. Ogo, H. Hiramatsu, K. Nomura, H. Yanagi, T. Kamiya, M. Hirano, H. Hosono, p-channel thin-film transistor using p-type oxide semiconductor, SnO, Appl. Phys. Lett. 93 (2008) 032113.

[46] W. Guo, L. Fu, Y. Zhang et al., Microstructure, optical, and electrical properties of p-type SnO thin films, Applied Physics Letters, vol. 96, no. 4, Article ID 042113, 2010.

[47] J. S. Ahn, R. Pode, and K. B. Lee, Study of Cu-doped SnO thin fims prepared by reactive co-sputtering with facing targets of Sn and Cu, in Solid Films, vol. 608, pp. 102-106, 2016.

[48] H. P. Pham, Thanh G. Le Thuy, Q. Trung Tran,et al., Characterization of Ag-Doped p-Type SnO Thin Films Prepared by DC Magnetron Sputtering, Journal of Nanomaterials, Volume 2017 (2017).

[49] L. L. Díaz-Flores, R. Ramírez-Bon, A. Mendoza-Galván, E. Prokhorov, J. González-Hernández, Impedance spectroscopy studies on SnO_2 films prepared by the sol-gel process, Elsevier, J. Phys. Chem. Solids, Vol.64, pp.1037-1042, 2003.

[50] Z. Chen, J. K. L. Lai, C. H. Shek, H. Chen, Synthesis and structural characterization of rutile SnO_2 nanocrystals, Cambridge University Press, J. Mater. Res., Vol.18, no.6, pp. 1289-1292, 2003.

[51] A.A. Bolzan, C. Fong, B.J. Kennedy, C.J. Howard, Structural studies of rutile-type metal dioxides, Acta Crystallogr. Sect. B-Struct. Sci. 53 (1997) 373.

[52] K. Ellmer, Resistivity of polycrystalline zinc oxide films: current status and physical limit, J. Phys. D: Appl. Phys. 34 (2001) 3097.

[53] R. G. Gordon, Criteria for choosing transparent conductors,MRS Bull. 25 (2000) 52.

[54] T. Minami, New n-type transparent conducting oxides, MRS Bull. 25 (2000) 38.

[55] H.L. Hartnagel.(1995). Semiconducting Transparent Thin Films, 1a ed. Institute of Physics Publishing, Philadelphia.

[56] J. Sundqvist, Employing Metal Iodides and Oxygen in ALD and CVD of Functional Metal Oxides, Acta Universitatis Upsaliensis, Uppsala, Ch.4, 35-56, 2003.

[57] S. R. Jain, K. C. Adiga, and V. R. Pai Verneker, A new approach to thermochemical calculations of condensed fuel-oxidizer mixtures, Combust. Flame, vol. 40, pp. 71-79, Jan. 1981.

[58] S. L. González-Cortés and F. E. Imbert, Fundamentals, properties and applications of solid catalysts prepared by solution combustion synthesis (SCS), Appl. Catal. A Gen., vol. 452, pp. 117-131, 2013.

[59] R. Branquinho, D. Salgueiro, A. Santa, A. Kiazadeh, P. Barquinha, L. Pereira, R. Martins, and E. Fortunato, Towards environmental friendly solution-based ZTO/AlO x TFTs, Semicond. Sci. Technol., vol. 30, no. 2, p. 024007, 2015.

[60] J. Leppäniemi, H. Majumdar, K. Ojanperä, T. Kololuoma, J. Dahl, M. Tuominen, P. Laukkanen, and A. Alastalo, Rapid low-temperature processing of metal-oxide thin film transistors with combined far ultraviolet and thermal annealing, Appl. Phys. Lett., vol. 115, no. 11, pp. 1-10, 2014.

[61] C. R. Kagan and P. Andry, Thin-film transistors. New York: Marcel Dekker, Inc., 2003.

[62] R. V. Kruzelecky, C. Ukah, D. Racansky, S. Zukotynski e J. M. Perz., Interband optical absorption in amorphous silicon, Journal of non-crystalline solids, 103 (1988) 234-249.

[63] R. Otsuka, T. Endo, T. Takano, S. Takemura, R. Murakami, R. Muramoto, J. Madarász2 and M. Okuya, Fluorine doped tin oxide film

with high haze and transmittance prepared for dye-sensitized solar cells, Japanese Journal of Applied Physics 54, 08KF03 (2015).

[64] T. Fukano, T. Motohiro, Low-temperature growth of highly crystallized transparent conductive fluorine-doped tin oxide films by intermittent spray pyrolysis deposition, Solar Energy Materials & Solar Cells 82 (2004) 567-575.